ANALYSIS AND SIMULATION OF DYNAMICS OF SPACECRAFT POWER SYSTEMS

by

Jae Ryong Lee

Dissertation submitted to the Faculty of the

Virginia Polytechnic Institute and State University

in partial fulfillment of the requirements for the degree of

Doctor of Philosophy

in

Electrical Engineering

APPROVED:

_____
Bo H. Cho, Co-chairman

_____
Fred C. Lee, Co-chairman

_____
Saifur Rahman

_____
Kwa S. Tam

_____
Lee W. Johnson

November 14, 1988

Blacksburg, Virginia

ANALYSIS AND SIMULATION OF DYNAMICS OF SPACECRAFT POWER SYSTEMS

by

Jae Ryong Lee

Bo H. Cho, Co-chairman   Fred C. Lee, Co-chairman

Electrical Engineering

(ABSTRACT)

Comprehensive analyses, including dc, small-signal and large-signal analyses, of the dynamics of various spacecraft power systems are performed. Systems' dynamics are analyzed for various operating modes, such as the shunt, battery-charge and battery-discharge modes, as well as the transition mode. Computer models using the EASY5 program are developed for the Direct Energy Transfer (DET) system, solar array switching system and partial shunt system to facilitate design, analysis and performance verification.

Large-signal analyses are performed to identify stability conditions and to predict large-signal dynamic behavior for each mode of operation. The equivalent source and load characteristics of a solar array power system with a constant-power load, shunt regulator, battery charger and discharger, are identified to predict large-signal dynamic behavior. Employing the equivalent source and load, the state trajectories of shunt failure, battery discharger failure and solar array/battery lockup are predicted and verified through time-domain simulations.

Small-signal analyses of the DET system are performed for the three modes of operation. The system loop gain is defined. Design guidelines for the feedback control loop of the shunt regulator, battery charger and discharger are developed to shape the system loop gain for the optimum bus dynamic performance and stability of the system. Designed subsystems

are simulated both in frequency-domain and time-domain to verify the design concept.

Various spacecraft power systems, such as solar array switching systems, a partial shunt system, a peak power tracking system and the COBE (Cosmic Background Explorer) power system are analyzed and simulated. Design guidelines of the power conditioning equipment for each system are provided.

-

Acknowledgements

I would like to express my sincere appreciation to my advisors, Dr. Bo H. Cho and Dr. Fred C. Lee, for their guidance, encouragement and support. I also would like to thank to the members of my committee, Dr. Saifur Rahman, Dr. Kwa S. Tam and Dr. Lee W. Johnson, for their valuable suggestions and comments on my dissertation.

I appreciate the help of   for providing many useful discussions and suggestions.

I acknowledge the support provided by NASA Goddard Space Flight Center, Greenbelt, MD, through the grant NAG5-518 to Virginia Power Electronics Center (VPEC) at Virginia Polytechnic Institute and State University.

It has been a pleasure to work with my fellow students at VPEC. I thank all those who have offered support and assistance throughout my research.

I am deeply grateful to my parents for their constant support of my academic pursuits. Finally, I dedicate this dissertation to my wife   and my children   in token of my love.

TABLE OF CONTENTS

CHAPTER 4. SMALL-SIGNAL ANALYSIS OF THE MAIN BUS DYNAMICS

CHAPTER 5. ANALYSIS AND SIMULATION OF VARIOUS SPACECRAFT POWER SYSTEMS

CHAPTER 1

INTRODUCTION

1.1 Introduction

The continuous growth in size and complexity of spacecraft power systems coupled with an increase in payload sensitivity to bus dynamics has focused attention on developing more efficient and reliable power processing systems. One of the important factors to determine the efficiency, reliability, size and weight, is the heat generated from power dissipation in the system. To improve the efficiency and minimize the heat generation in the spacecraft power system, the solar array switching system, partial shunt system and peak power tracking system have been widely used among existing and currently developing systems. The power conditioning equipment, which balances the power between the source and payloads, also employs more efficient and reliable power processing circuits such as a pulse-width-modulated (PWM) shunt, sequential shunt, and switching converters for the battery charging and discharging circuits.

As the components and subsystem are interconnected to configure a complex system, many undesired interactions that exist among highly-nonlinear components become a severe problem. Even though the behavior of individual components may be well understood and documented, there has been a major deficiency in the ability to perform integrated-system

level analysis, design and performance evaluation. Thus, the need of a comprehensive power system model that can effectively predict a system's local and global behavior is most critical to facilitate the **analysis, design and performance evaluation** for present and future spacecraft power systems.

To facilitate both the frequency-domain and time-domain simulation of the large-scale power system, a comprehensive modeling technique using the EASY5 program [1] was recently developed in [2]. Since this modeling technique utilizes a modular approach using a two-port coupling method, models are flexible, sufficiently accurate, verifiable and computationally efficient. The following models were generated in the previous study: solar array, linear shunt regulator, battery discharger and switching regulators.

A large-signal analysis is needed to investigate the stability and large-signal dynamic behavior of the system's main bus. In Ref. 2, a large-signal analysis was performed to study the state trajectory of the solar array power system with a constant-power load. The stability of each equilibrium point on the solar array I-V curve was analyzed using the eigenvalues of the simplified second-order system. Three different operating regions on the solar array I-V curve were identified.

For the stability concern of the solar array power system, previous research has shown that the current source region on the solar array's I-V curve is unstable when the solar array has a constant-power load. The current source region of the solar array's output voltage, however, is chosen as the regulation voltage of the main bus in many recent spacecraft power systems using the regulated bus. Since the solar array system with a constant-power load in the current source region becomes an open-loop unstable system, it is important to understand how the bus regulators, such

as the shunt regulator and battery discharger, stabilize the main bus of the system.

To avoid subsystem interaction and to optimize the dynamics of the system bus, such as dc regulation, stability and bus impedance, a design approach for the main bus shunt regulator was introduced [4].

Although several papers have presented design methods for the battery charger and discharger, they deal with the performance of the charger or discharger itself without considering the system's dynamic performance, when the equipment is connected to the bus. For instance, the battery discharger is often designed with the assumption that its load is resistive, even though the load characteristic is complex when the discharger is connected to the bus. Since the battery-charger functions as a bus regulator only during a certain transient period, little attention has been given to this mode of operation. In order to ensure good dynamic performance for a complete orbit cycle, however, it is essential to properly design the charger's control loop by considering the dynamics of the system, as well as the charger itself.

Since design verification through an integrated system's hardware testing is expensive or often impossible, time-domain simulations are essential to evaluate the performance of systems. In order to simulate the entire system in various modes of operation, necessary components and subsystem models should be developed.

1.2 Objective and Outline of Chapters

The objective of this dissertation is to perform comprehensive dynamic analyses for various spacecraft power systems to provide design guidelines for the optimum dynamic performance and stability of the systems.

Specific goals of this study are:

- All the necessary component models and subsystem models for the direct energy transfer (DET) system, solar array switching system and partial shunt system, are developed to perform the dc, small-signal ac and large-signal analyses, and design verification through time-domain simulations.

- The large-signal analyses include identification of stability regions and prediction of large-signal transient behavior, such as a failure mode and solar array/battery lockup.

- The small-signal analyses include optimization of the bus impedance and stability margin, and design of feedback compensators for the power conditioning equipment.

- The proposed system configuration and design concepts are analyzed through frequency-domain simulations for small-signal dynamics, such as stability margins and bus impedance, and time-domain simulations for steady state and transient responses.

In Chapter 2, new component models, such as a battery model, battery charger model, sequential shunt regulator, etc., which are essential for the spacecraft power system modeling, are developed to simulate a complete power system. The previous models [2] are also improved to provide additional flexibility and accuracy. The performance of each component model is verified through simulations. Other component models, such as the solar array switching unit, partially-shunted solar array and dc models of battery charger and discharger, are developed to study various power systems and one-orbit cycle simulation in Chapter 5.

The previous study of the stability of the solar array power system using a state-plane analysis technique is reviewed in Chapter 3. The analysis is expanded to the DET power system. To understand bus dynamics, a simplified second-order system, treating the bus voltage and solar array output current as two state variables, is developed. The stability criteria are derived and state trajectories are analyzed using the dc characteristics of the source, load and bus regulators for each mode of operation. Design strategies for the solar array's operating region and each regulator's dc gain are provided. The solar array/battery lockup phenomenon is analyzed and graphically depicted. Methods to free the system from the battery lockup mode are also provided. To understand the main bus behavior when the power conditioning equipment is abruptly removed from the bus, two failure modes, the shunt-regulator failure and the battery-discharger failure, are analyzed in the state-plane, and simulated to observe the bus voltage transient after the failure.

In Chapter 4, small-signal dynamics of the main bus of the DET power system are analyzed in various modes, such as the shunt, battery-charge and -discharge modes. A design methodology of each bus regulator is presented to optimize the performance of the bus, including dc regulation, stability and bus impedance. Dynamic performances of the bus are simulated with small-signal and large-signal system models.

Several alternative spacecraft power system configurations are considered in Chapter 5. These are solar array switching systems, a partial-shunt system and a peak power tracking system. An analysis of the stability of the solar array switching system and a design strategy of the feedback loop are provided. By comparing two solar array switching systems, their advantages and disadvantages are identified through analysis and simulation. A simulation of the partial-shunt system allows the voltage and current waveforms of the upper and lower portion of the solar array to

be observed and the power dissipation of the system to be compared with that of a functionally equivalent full-shunt system. The concept of the peak power tracker (PPT) system is illustrated using buck-type and boost-type PPT examples. Finally, the COBE system is modeled and simulated to examine the transient responses during mode changes, and a complete one-orbit cycle simulation is performed to observe the current and voltage profile during an orbit cycle.

Conclusions are presented in Chapter 6.

CHAPTER 2

MODELING OF SPACECRAFT POWER SYSTEMS

2.1 Introduction

As the size and complexity of spacecraft power systems grow, computer simulation has become an essential tool for system design. Many package programs are available for simulating electrical circuits. Generalized circuit analysis programs, including SPICE, are useful for simulating circuits, including the detail characteristics of individual devices. In these programs, all device parameter values are users' inputs. Also, these programs provide a high level of user-friendliness, such that users only need to input the node information of the circuit to be analyzed, without writing any circuit equations. However, when the system becomes large, the number of components increases and the required computer memory and computation time rise tremendously.

For system-level study, a detailed analysis of the behavior of each circuit component is usually not necessary and the voltage and current waveforms

at circuit level (or subsystem level) are mainly needed for assessing dynamic response. To develop a system model which produces a required system response with a reasonable amount of computer memory and computation time, the EASY5 program has been chosen as a host program. The EASY5 has many desired capabilities for large-scale system modeling, such as modularization, flexibility and efficiency [4].

In Section 2.2, the large-scale system modeling approach developed in [2] is reviewed. The differences between the time-domain model and frequency-domain model are described. In Section 2.3, component models essential for spacecraft power system are developed and the previously-developed models are improved in accuracy and flexibility. The component models developed include the solar array model, full shunt model, sequential shunt mode, battery model and battery charger model.

The developed models are verified by comparing the simulated results with measured data, whenever available.

2.2 Modeling Approach of Large-scale Systems

For large systems, it is not feasible to define the complete system entirely in terms of circuit elements is not feasible. A logical approach should be the modularization of components (equipment) or subsystems. These components or subsystems are then interconnected to form a system.

To utilize the modular concept, each component should be modeled as an unterminated multi-port network (Fig. 2.1). In general, each module receives two inputs, such as V_1 and I_2, from preceding and following modules and gives two outputs, I_1 and V_2, to two adjacent modules. A source model, such as a solar array model, becomes an unterminated one-port network with one input, I_{SA} (or V_{SA}), and one output, V_{SA} (or I_{SA}). The component models are internally defined in terms of the hybrid-g [G] parameter representation of the specific power system component. For example, in the case of two-port network,

$$\begin{bmatrix} I_1 \\ V_2 \end{bmatrix} = \begin{bmatrix} g_{11} & g_{12} \\ g_{21} & g_{22} \end{bmatrix} \begin{bmatrix} V_1 \\ I_2 \end{bmatrix}$$

Each element of the G matrix can be a linear, nonlinear or time variant function.

The circuit model is, in general, expressed with circuit equations and/or state equations. Circuit devices, such as BJT, FET, op-amp, etc., can be modeled with any existing modeling technique as needed. For example, an op-amp can be modeled as an ideal op-amp or a finite gain op-amp by writing the circuit equations either way in the EASY5 component model program. If the temperature effect should be considered, the model pro-
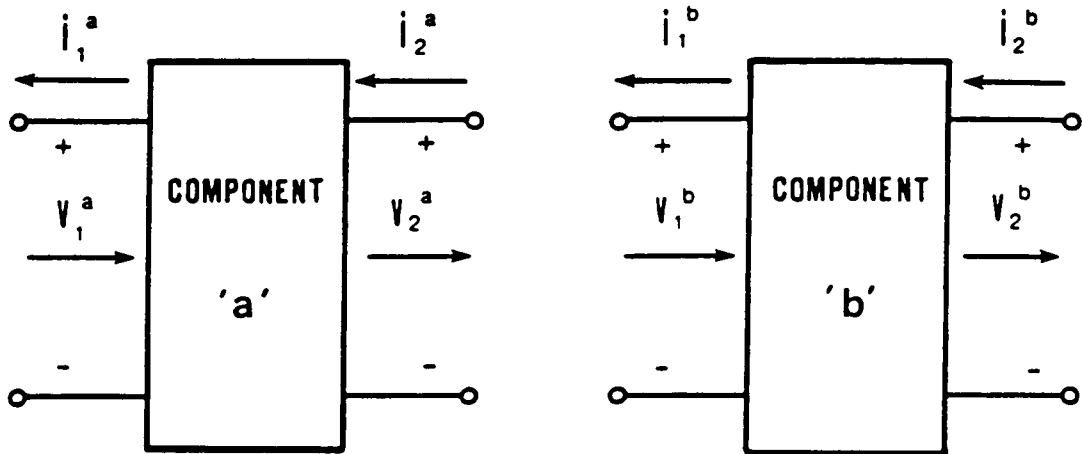
Fig. 2.1 Two-port subsystem coupling using the hybrid G-matrix

gram can use the device model equations with a temperature coefficient. Therefore, each component model can be built as a precise model or a simplified model, depending on requirements.

The large-signal models are usually developed using the state equations. Some models, however, can be represented by their transfer functions. Since the state equation is expressed with actual circuit components such as resistors, inductors, and capacitors, it is convenient to observe the voltage or current waveforms at each component. The transfer function model provides locations of poles and zeros, so design modification by a small-signal analysis can be easily implemented. One disadvantage of the transfer function model is that the initial condition of energy storage elements cannot be directly observed.

For time-domain simulations, the EASY5 numerical integration routine calculates current values of the states and output variables for each module. It then passes along the output values to an adjacent module according to the interconnection law. There are seven different types of numerical integration routines available in EASY5. Each offers a different numerical stability and computational efficiency dependent on the type of nonlinearity of a system. In general, variable step methods, such as the Gear method and the Runge-Kutta Variable Step Integrator, are efficient in linear systems. Fixed-step methods, such as the Euler method and the Heuns method, are more efficient in those nonlinear systems which consist of many switching regulators.

The model development of each time variant component (e.g. power stage model of switching regulators) of a spacecraft power system involves two separate models, the large-signal time-domain simulation model and the small-signal linearized model. For frequency domain simulations, the EASY5 program calculates a linear approximation to a nonlinear system

(time invariant) at any operating point given by users. The linearized model of a given nonlinear system is formed internally by perturbing, one at a time, the states and the inputs [1]. The size of perturbation can be determined by users. Using the EASY5 command TRANSFER FUNCTION, the Bode plot of the transfer function can be obtained from an input variable to an output variable defined by a user. It is convenient that, after building a system model composed of several component models, one can also obtain the transfer function of local variables by freezing the state variables in the rest of the models. For example, after a switching regulator with a control loop is modeled, one can obtain the transfer functions of just the power stage, as well as the loop gain of the closed loop.

2.3 Component Model Development

In this section, EASY5 component models (the major equipment of the spacecraft power system) are described. Since such models as switching regulators and a battery discharger were discussed in [2], descriptions for these models are omitted here. The solar array model developed previously is improved to include the effect of temperature. Also, to avoid numerical instability in the current source region, the solar array is modeled differently. The shunt regulator is modeled in two ways, by the state equation method and the transfer function method. The sequential shunt regulator model is developed in order to understand its advantage over the ordinary shunt regulator. The battery charger and battery models are developed to simulate a complete spacecraft power system.

2.3.1 Solar Array Model

The primary objectives of the solar array model are to accurately predict the behavior of an array of photovoltaic cells to be used in a comprehensive power system model. In order to predict the dynamic behavior inside the solar array, it is necessary to use a large-signal model. However, since the cell parameters, such as the dynamic resistance, diffusion and junction capacitances of a diode, varies depending on cell voltage, current, illumination and temperature, it is very difficult to develop a large-signal model including the effect of these variations. A satisfactory large-signal model has not been found. Instead of a large-signal model, a dc model of the solar array is easy to model and useful to simulate the terminal characteristics of the solar array.

Two approaches for developing the solar array dc model are widely used. First, a curve-fitting routine using least squares fit can be used to

determine the coefficients of the given solar array I-V curve. Voltage and current points along the curve are entered into the curve fitting routine. The polynomial coefficients are calculated, and the array current at each voltage point is calculated. Secondly, the solar cell circuit model is used with a macro model approach [5]. A typical circuit model is shown in Fig. 2.2. Since this circuit model is flexible and efficient for simulating the solar array in various conditions, this approach is chosen for this study.

An analytical expression that describes the terminal characteristics of the solar cell model in Fig. 2.2 is

$$I_o = I_g - I_{do} [\exp \frac{Q}{kT} (V_o + I_o R_s) - 1] - \frac{V_o + I_o R_o}{R_{sh}} \qquad (2.1)$$

I_o = current output of the cell

I_g = light-generated current

I_{do} = reverse saturation current

Q = magnitude of the electronic charge

k = Boltzmann constant

T = cell temperature ($^o K$)

V_o = output voltage at the cell terminals

R_s = series resistance

R_{sh} = shunt resistance

Based on the cell model, a solar array macro model is constructed by assembling solar cells in parallel and series connections. The resulting equivalent circuit model is illustrated in Fig. 2.3, where its elements are lumped parameters and functions of the number of cells in series, n_s, and the number of parallel strings, n_p.
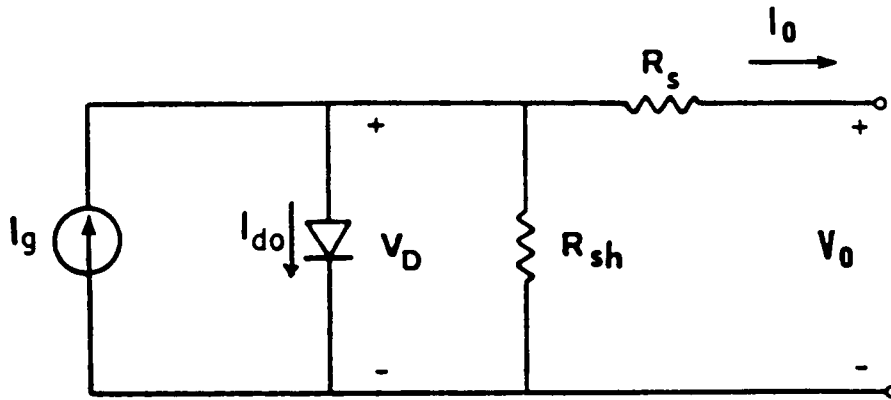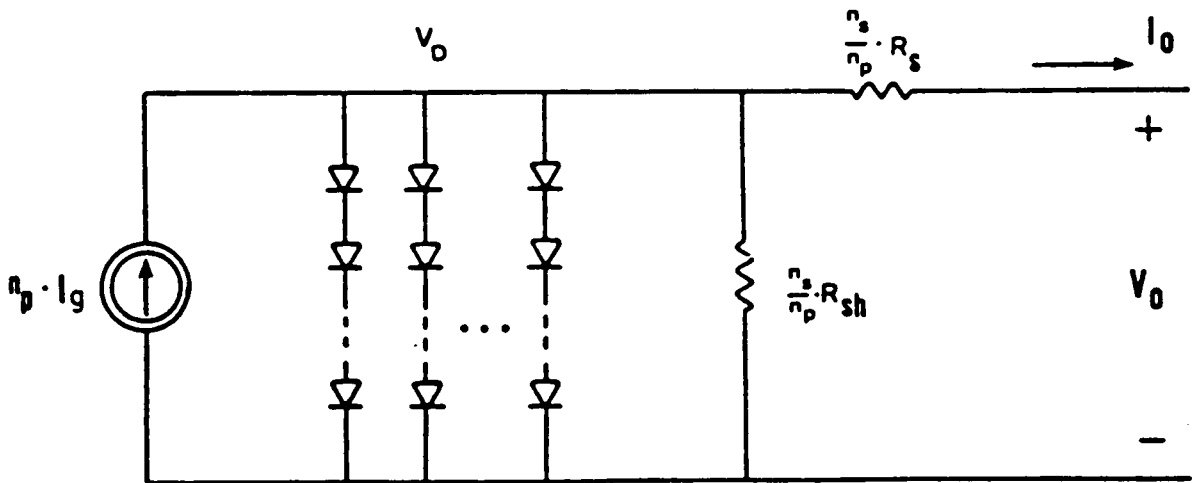
Fig. 2.2 DC model of solar cell

Fig. 2.3 DC macro model of solar array

The analytical expression for the terminal I-V characteristic of the solar array model in Fig. 2.3, then, is

$$I_o = n_p \left[I_g - I_{do} \left\{ \exp \frac{Q}{kT} \left(\frac{V_o}{n_s} + \frac{I_o R_s}{n_p} \right) \right\} - \frac{1}{R_{sh}} \left(\frac{V_o}{n_s} + \frac{I_o R_s}{n_p} \right) \right] \quad (2.2)$$

From Eq. (2.2), the solar array operating conditions are set by the load power demand and regulation of the bus voltage regulators, such as a shunt regulator, battery charger and discharger. Other, more elaborate, analytical dc models exist. They include such effects as the diffusion process and the carrier recombination in the silicon p-n junction [6]. Due to the complexities of the models, it is not practical to incorporate these effects in the system study.

Model Generation

Equation (2.2) can be rewritten as following.

$$I_o = n_p \left[I_g - I_{do} \left\{ \exp K_o \left(\frac{V_o}{n_s} + \frac{I_o R_s}{n_p} \right) \right\} - \frac{1}{R_{sh}} \left(\frac{V_o}{n_s} + \frac{I_o R_s}{n_p} \right) \right] \quad (2.3)$$

where $K_o = \dfrac{Q}{AkT_o}$

T_o : Nominal temperature (301^oK)

A : Empirical data-fitting constant

Since the above equation is an implicit function, that is, $I_o = f(I_o, V_o)$, solutions I_o and V_o can be obtained using a numerical iteration method. In this model, the Newton's Method was used. The algorithm of Newton's Method is expressed as

$$X_{n+1} = X_n - \frac{f(X_n)}{f'(X_n)} \qquad n = 0, 1, 2, 3 \dots$$

To incorporate the solar array model in a complete system, the solar array current, I_o, is chosen to be the independent variable (input variable) and the output voltage, V_o, to be the dependent variable (output variable) as expressed in Eq. (2.4).

$$f(V_o) = n_p [\, I_g - I_{do} \exp K_o (\frac{V_o}{n_s} + \frac{I_o R_s}{n_p}) - \frac{1}{R_{sh}} (\frac{V_o}{n_s} + \frac{I_o R_s}{n_p}) \,] - I_o \quad (2.4)$$

With this equation, the solar array is modeled as a voltage source. However, in the current source region of the solar array (from 0V to the peak power voltage, V_{pp}), the Newton iteration routine tends to diverge because the current level is almost flat in the region. To avoid this problem, the solar array is modeled as a current source using the following equation:

$$f(I_o) = n_p [\, I_g - I_{do} \exp K_o (\frac{V_o}{n_s} + \frac{I_o R_s}{n_p}) - \frac{1}{R_{sh}} (\frac{V_o}{n_s} + \frac{I_o R_s}{n_p}) \,] - I_o$$

That is, the solar array output voltage, V_o, is used as the input variable and the output current, I_o, as the output variable.

Although Eq. (2.3) includes the parameter of cell temperature, the equation is valid only for a cell temperature of 301^oK with other parameter values at the temperature. As discussed before, other parameter values vary, depending on cell temperature.

There are several papers [5, 6] which describe a method to include the temperature effect in the solar array model. One simple expression for the temperature effect is as follows [5]:

$$\Delta I = f_c \Delta T$$

$$\Delta V = (f_v + f_c R_s) \Delta T$$

where ΔT, ΔI and ΔV represent the difference between the values at a given temperature and the nominal temperature (301^oK). The temperature coefficients of current and voltage are f_c and f_v, respectively. The current coefficient, f_c, can be obtained from the empirical data of the solar array I-V curve by comparing the short-circuit currents at a given temperature and at the nominal temperature. The f_v is obtained from the open-circuit voltage difference at the two temperatures with the known f_c and R_s.

The illumination change effect of the solar array I-V characteristics is modeled by multiplying an appropriate factor to the light-generated current, I_g, under the assumption that the illumination change affects only the value of I_g.

Example of Simulation

Figure 2.4 shows the solar array I-V curves at four temperatures. For this simulation, the circuit model shown in Fig. 2.3 was used to obtain the solar cell's terminal characteristics at four different temperatures. This simulation result was similar to the original graph drawn from the experimental data in [7]. From this comparison, between the simulation results and the experimental results, the validity of the model is verified.

The solar cell model's parameter values were obtained from the experimental data of a 2×2 cm, 10 ohm-cm, 8 mil silicon cell [5].
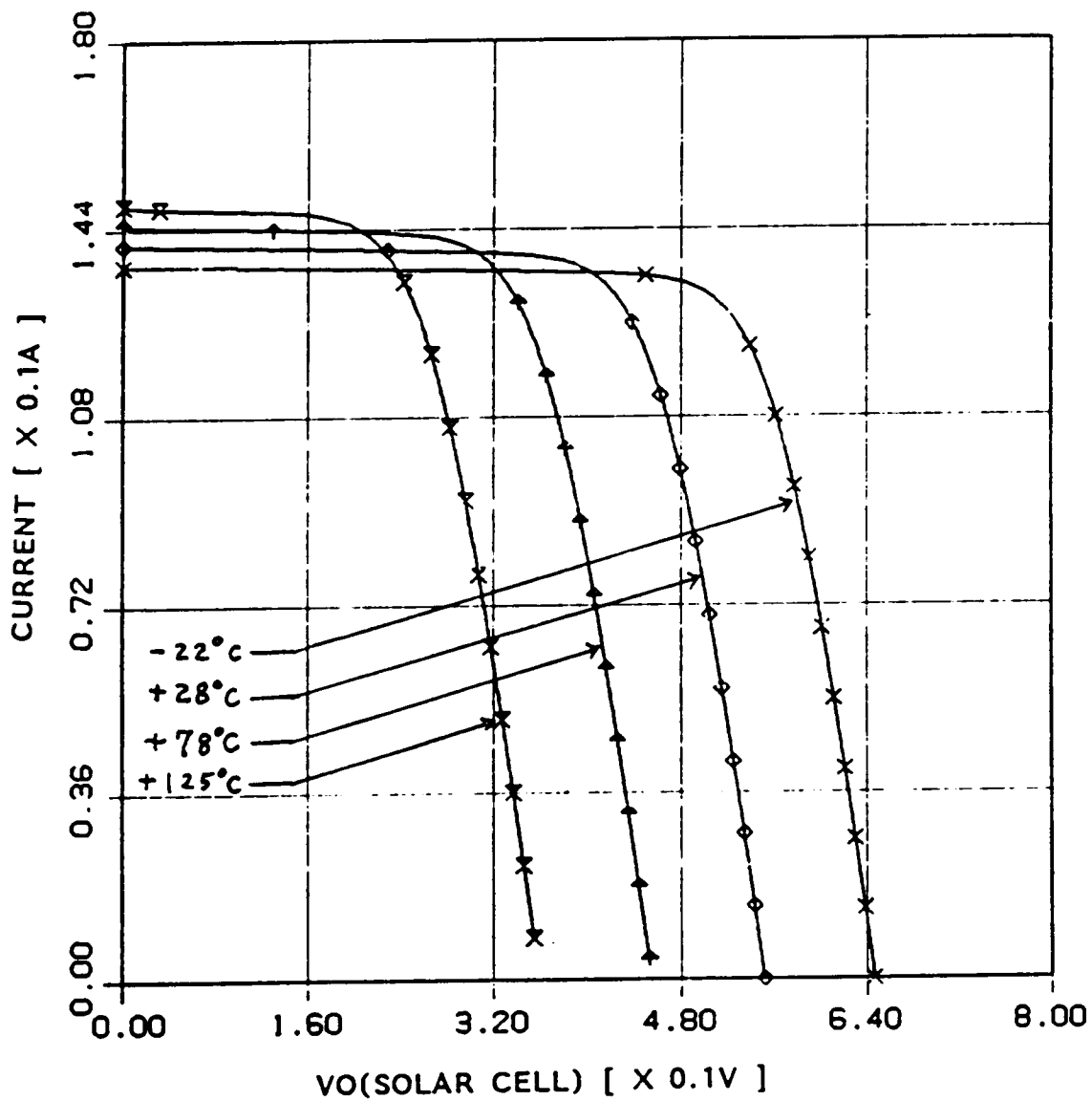
Fig. 2.4 Simulation result of solar array model

2.3.2 Shunt Regulator Model

Shunt regulators are used to limit the power bus voltage when excess solar array power is available. Since the basic function of the shunt regulator is to regulate the bus voltage by dissipating the excess power through the shunt elements, there are several different types of shunt regulators developed to reduce the amount of heat dissipation in shunt elements and to eliminate the thermal balance problem of spacecraft.

To illustrate shunt regulator modeling techniques, typical shunt regulators are modeled in detail in the following sections. The circuit diagram and the block diagram are shown in Figs. 2.5 and 2.6. These models take into account nonlinearities, including op-amp feedback, op-amp saturation and darlington cut-off. All diodes, including the transistor base-to-emitter junctions, have an infinite reverse impedance. The first-order model is used for transistors with their parameter values (such as current gain and base-emitter junction voltage, V_{be}) as the user's inputs.

Most shunt regulators are composed of two major function blocks, the error amplifier (EA) block and the shunt element block. In some applications, the EA block is implemented with three identical amplifier circuits and a majority voting circuit for redundancy. Also, the shunt element block is mostly composed of parallel, identical shunt transistor circuits or sequential turn-on shunt transistor circuits. Since it is not practical to generalize the model to fit any shunt regulator circuit, a typical shunt circuit is modeled to demonstrate modeling techniques.

2.3.2.1 Full Shunt Regulator Model

A. Modeling with transfer functions

A shunt regulator circuit, Fig. 2.5, is modeled through the block diagram shown in Fig. 2.6. The block diagram shows the transfer function representation of each functional block of the circuit. This transfer function model is useful when creating a generalized model to handle different circuits belonging to the same type shunt. The transfer function model is particularly useful for the frequency response analysis. By providing the values of gains, poles and zeros, the user can implement the corresponding models for different circuits.

Although the model is implemented based on transfer functions, the transfer functions are programmed with state equations in the model when the functional block diagram is actually modeled. The A_s block, in Fig. 2.6, can be expressed in state equations as

$$S2 = a_1 S1 + X1$$

$$\dot{X1} = a_1 S1 Z_0 - S2 P_0$$

The above state variable equations were converted from a transfer function which had one pole and one zero. The input (S1) of this block is an error voltage between the K_1, V_B ($= V_{bus}$) product and $V_r (= V_{ref})$, and the output voltage (V_{o1}) is the sum of the dc voltage component and the ac voltage component (S2) of the A_s block.

$$S1 = K_1 V_B - V_r$$
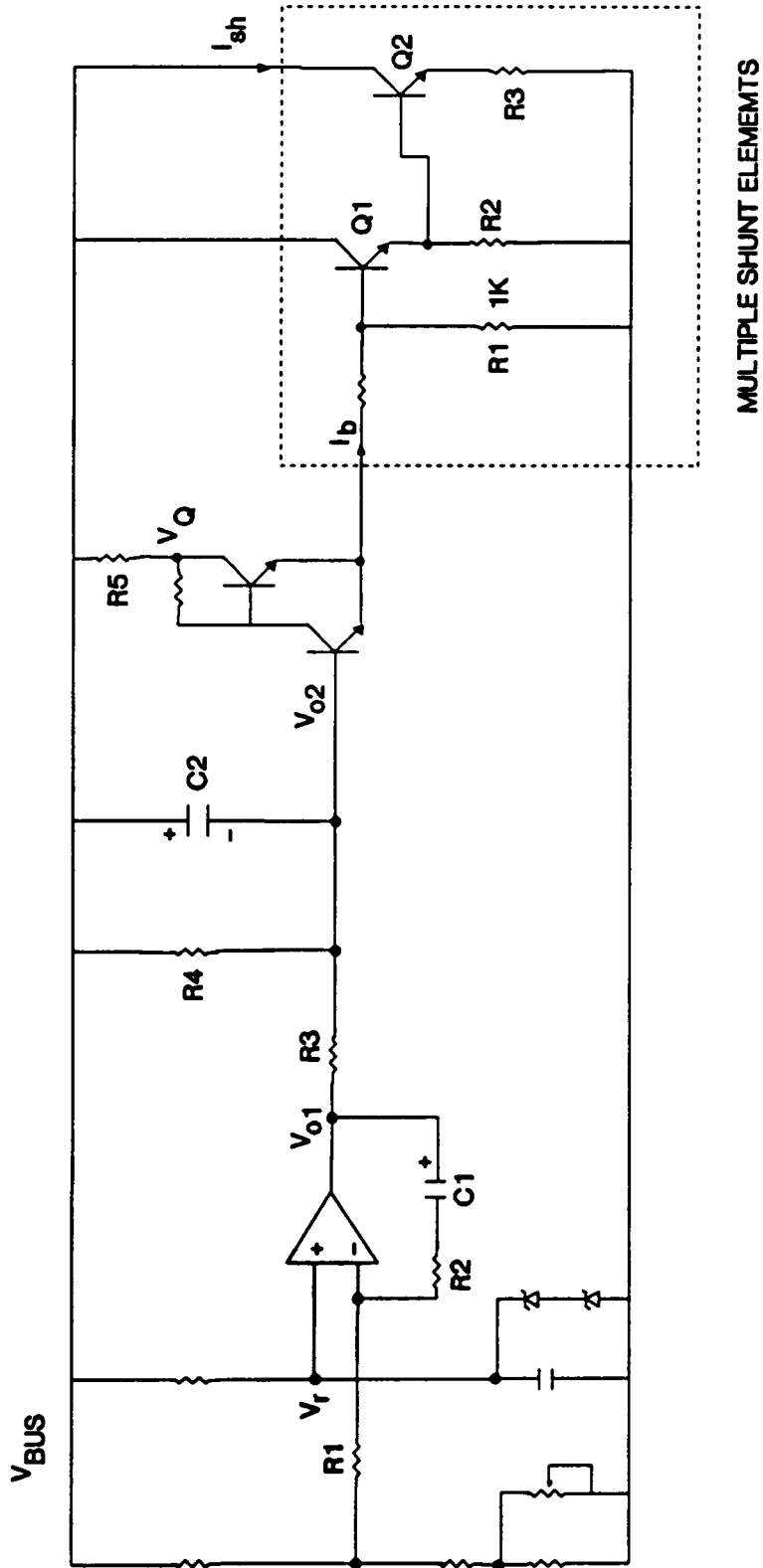
$$V_{o1} = S2 + V_r$$
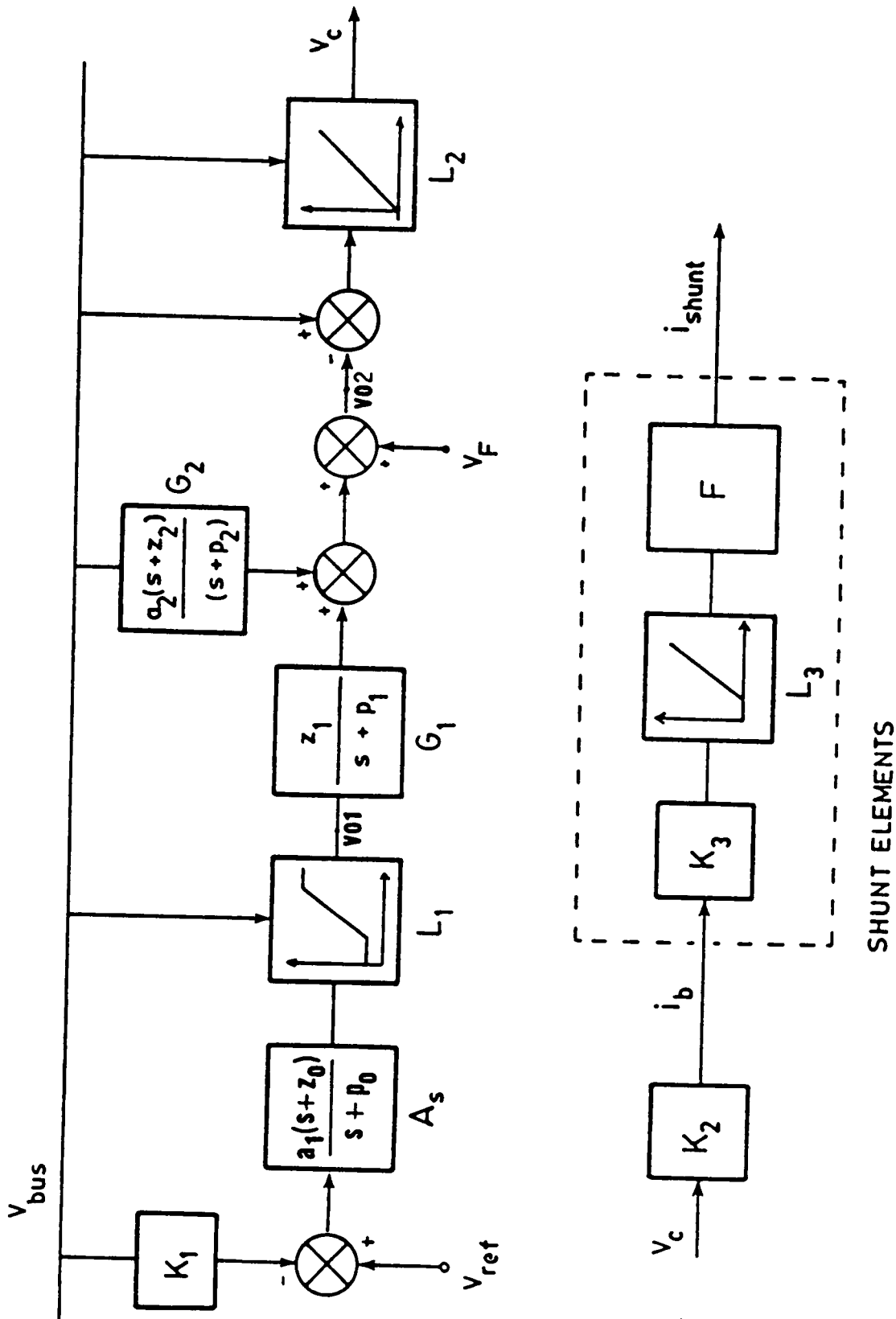
Fig. 2.5 Circuit diagram of typical shunt regulator

Fig. 2.6 Small-signal block diagram of Fig. 2.5

23

The dummy state variable, X1, which is not a capacitor voltage, is introduced by converting the transfer function into state equations. Similarly, the G_1 and G_2 blocks are expressed in state equations. However, in this case, the inputs (S1, S3) of these blocks are V_{o1} and V(bus), respectively, and the outputs (S2, S4) are directly fed to the summer in order to obtain V_{o2}. The L_1 block represents the op-amp saturation. This limiting function can be easily implemented by using FORTRAN 'IF' statements. The V_F is needed to include the base-emitter junction voltage drop of the darlington circuit. The L_2 block represents the limiting of control voltage, V_c, to a positive value. The K_2 block is a gain of control voltage to base current of the transistor driver circuit, and K_3 is a factor from the number of multiple shunt elements. The L_3 block represents the I_c vs. V_{be} characteristic of the shunt transistor. The F block represents the functional expression of the shunt current, I_{sh}, with respect to base current, I_b.

$$I_{sh} = f(I_b) = C1\, I_b + C2$$

$$C1 = \frac{\beta1\, \beta2\, R1\, R2}{\beta1\, \beta2\, R2\, R3 + \beta2\, R1\, R3 + R1\, R2} \tag{2.5}$$

$$C2 = -\frac{0.7\beta2\, (R1 + \beta1\, R2)}{\beta1\, \beta2\, R2\, R3 + \beta2\, R1\, R3 + R1\, R2} \tag{2.6}$$

where $\beta1$ and $\beta2$ are the current gains of transistors Q1 and Q2, respectively, and V_{be} of Q1 and Q2 is assumed to be 0.7V.

B. Modeling with state equations

The same shunt regulator circuit, Fig. 2.5, is modeled employing the state equation representation. The state variable represents the actual

capacitor voltage or inductor current. This circuit can be divided into three function blocks, i.e., error amplifier circuit, error amplifier output circuit and shunt element circuit, as shown in Fig. 2.7a-c.

1) Error amplifier circuit

If the op-amp is assumed to be ideal, then the output voltage (V_{o1}) can be expressed in terms of the inputs $(K_1 V_B$ and $V_r)$ and the state variable, V_{c1} , by the following equation:

$$V_{o1} = -\frac{R2}{R1}(K_1 V_B) + (1 + \frac{R2}{R1})V_r + V_{c1}$$

The state variable, V_{c1}, is expressed as

$$\frac{dV_{c1}}{dt} = \frac{V_{o1} - V_r - V_{c1}}{C1\, R2}$$

since the current through capacitor C1 is

$$C1\frac{dV_{c1}}{dt} = \frac{V_{o1} - V_r - V_{c1}}{R2}$$

In order to take into account the saturation effect of op-amp, the output voltage (V_{o1}) is limited to a voltage between the supply voltage (V_{bus}) and the ground.

2) Error amplifier output circuit

Since the error amplifier circuit, shown in Fig. 2.7b, is a simple linear circuit, the following output voltage equation and capacitor-voltage state equation are easily obtained to model this circuit.

$$V_{o2} = V_B - V_{c2}$$

$$C2\frac{dV_{c2}}{dt} = -\frac{V_B}{R4} - \frac{V_{o1}}{R3} + \frac{(R3 + R4)V_{o2}}{R3\, R4}$$
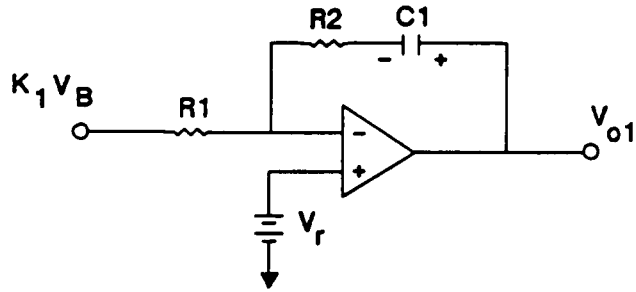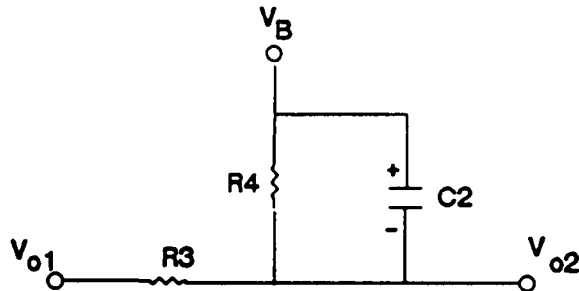
Fig. 2.7a Error amplifier circuit

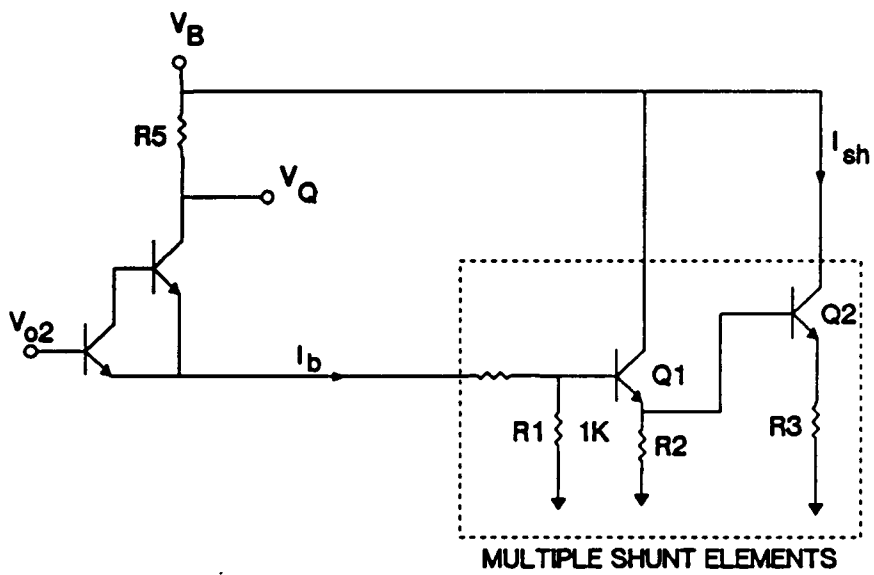Fig. 2.7b Error amplifier output circuit

Fig. 2.7c Shunt element circuit

26

3) Shunt element circuit

This circuit is basically a shunt transistor circuit with a base-drive circuit. If the upper darlington is not in cut-off, then the emitter current, I_b, to transistor Q1 is

$$I_b = \frac{V_B - (V_{o2} + 1.4)}{R5\, N}$$

where 1.4V is a darlington base-emitter voltage drop and N represents the number of multiple shunt elements. The shunt current flows only when V_Q, which is equal to $V_B - (V_{o2} + 1.4V)$, is positive. Also, before there is any shunt current, the voltage across the $1K\Omega$ resistor must be at least 1.4V or I_b must be greater than 1.4mA. Once I_b is determined, the shunt current can be expressed in terms of I_b through manipulation of transistor circuit equations. As a result,

$$I_{sh} = f(I_b) = C1 I_b + C2$$

where C1 and C2 are described in Eqs. (2.5) and (2.6). Finally, the shunt current is limited to the maximum current capacity of the solar array current.

$$0 < I_{sh} < I_{SA}(\max)$$

Example of Simulation

For simulation of the shunt regulator, a system consisting of the transfer-function shunt model, a solar array model and a constant-power load is configured.

In this simulation (Fig. 2.8), a constant-power load of 800W is applied to the solar array, which has an output power capacity of 853W. After the system reaches a steady state, a step load change was applied from
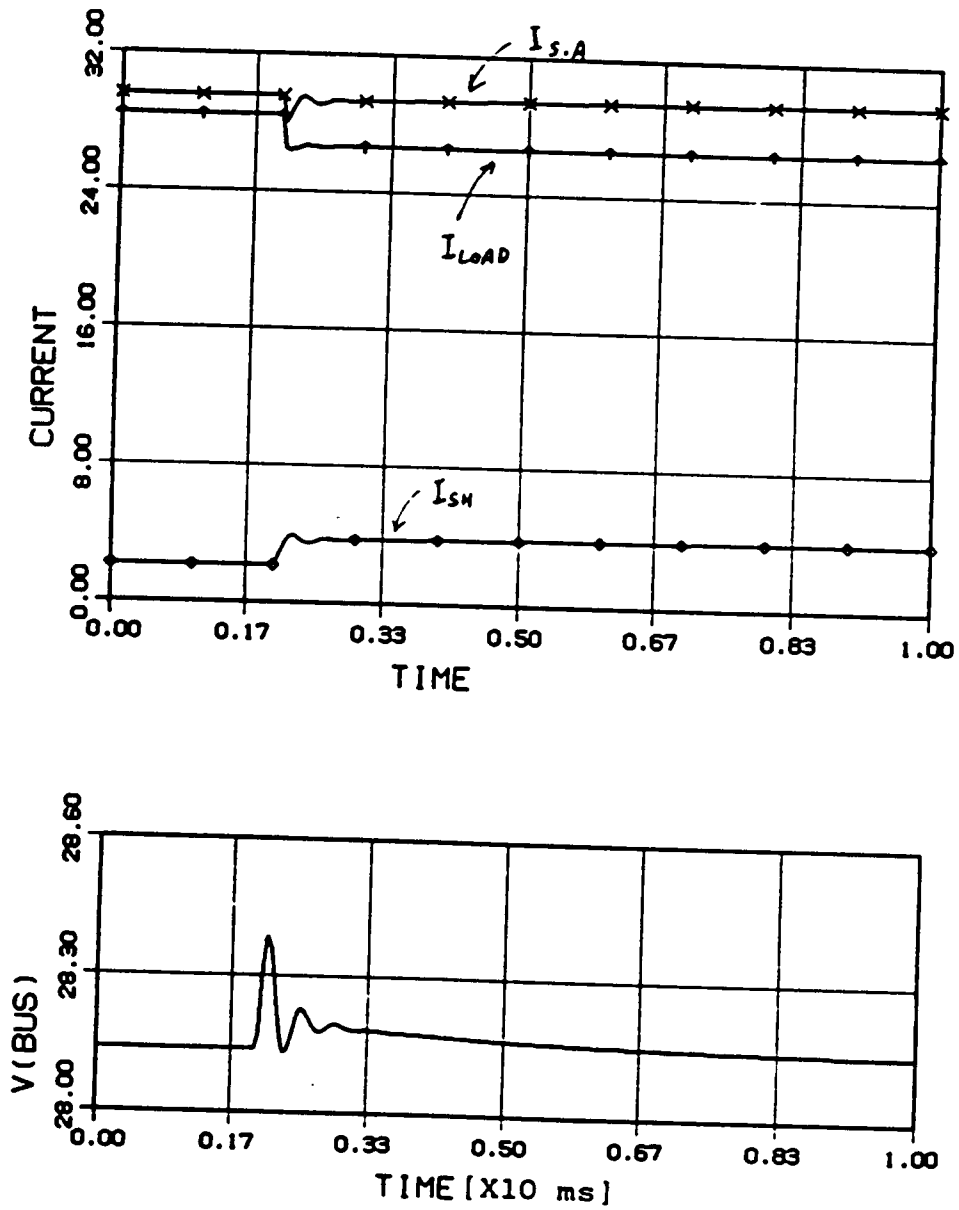
Fig. 2.8 Simulation results of shunt regulator model

800W to 750W at 2ms. The decrease in the load power causes the shunt current to rise. The shunt current is added to the load current so the solar array output current remains almost constant after a small transient. As a result, the bus voltage recovers its specified voltage (28.14V) after a transient period. From this simulation, one can observe system's step-load change responses, such as the overshoot/undershoot, settling time and steady state error, etc., for the shunt current, solar array current and bus voltage.

The same system, using the state-equation model for the shunt regulator, was also simulated. The simulation results were identical to those of the previous simulation, shown in Fig. 2.8.

2.3.2.2 Sequential Shunt Model

The basic function of the sequential shunt regulator is the same as the shunt regulator discussed in the previous section. However, the sequential shunt, composed of multiple shunt elements which turn on sequentially as the bus voltage rises, has several advantages over the full shunt regulator. One major advantage is that the power dissipation of the sequential shunt elements is much smaller than other regulators. This is because the elements that are turned on earlier stay in the saturation region (for BJT's, and ohmic region for MOSFET's), and only the shunt element that is turned on last stays in the linear region (for BJT's, and saturation region for MOSFET's).

In this section, the sequential shunt regulator used in the COBE, shown in Fig. 2.9, is modeled. The power MOSFET is modeled on the assumption that this device is operated in a linear fashion, as shown in Fig. 2.11, when it is in a saturation region. The drain current is expressed as

$$I_d = gm(V_g - V_{gst})$$

where I_d = drain current

gm = forward transconductance of MOSFET

V_{gst} = gate threshold voltage

Then, from the simplified circuit for one section of the regulator (Fig. 2.10), three equations can be written:

$$V_x = V_{drive} + \frac{R1}{R1 + R2}(V_1 - V_{drive})$$

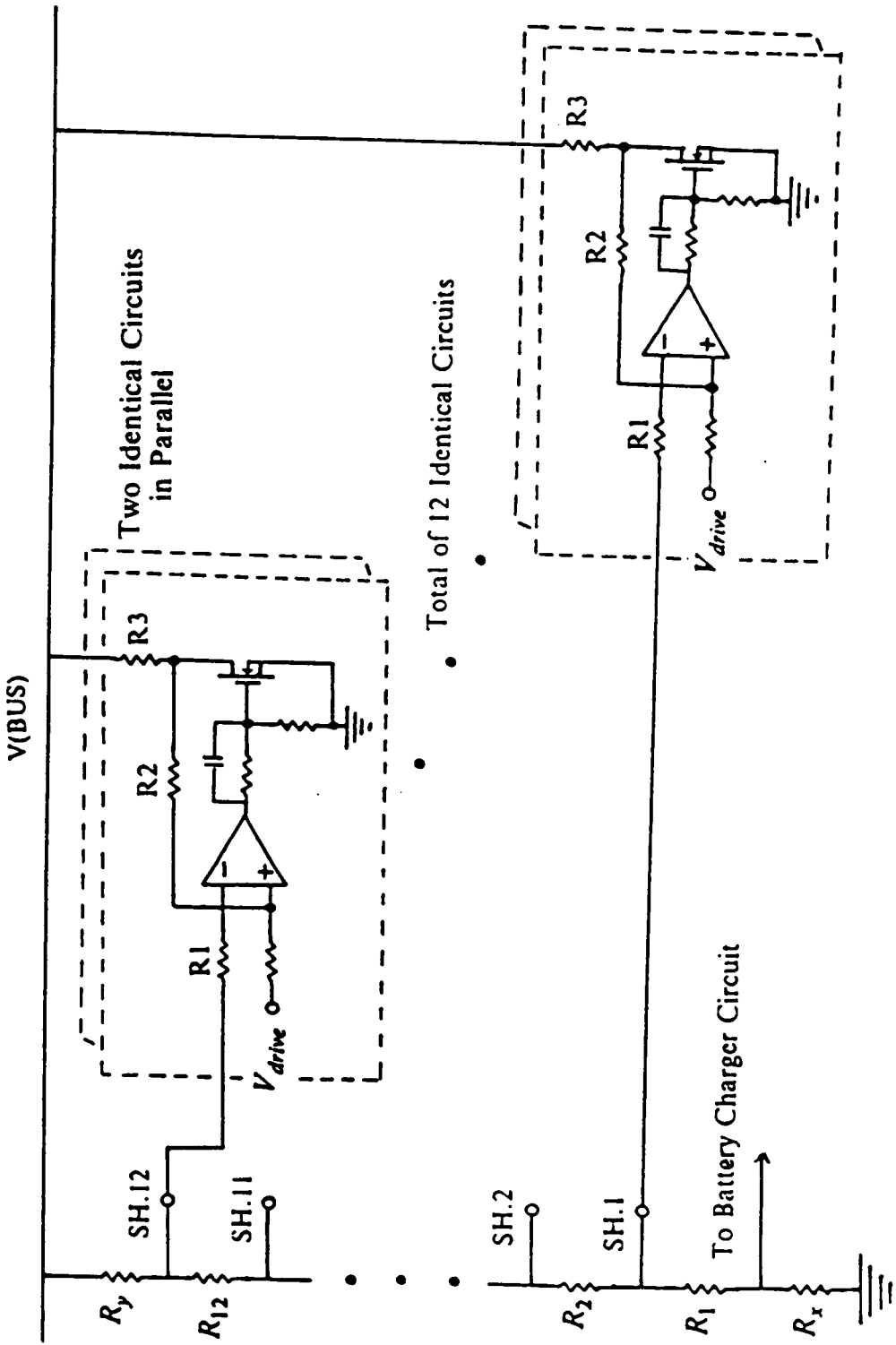$$V_o = gain(V_x - V_{bias})$$

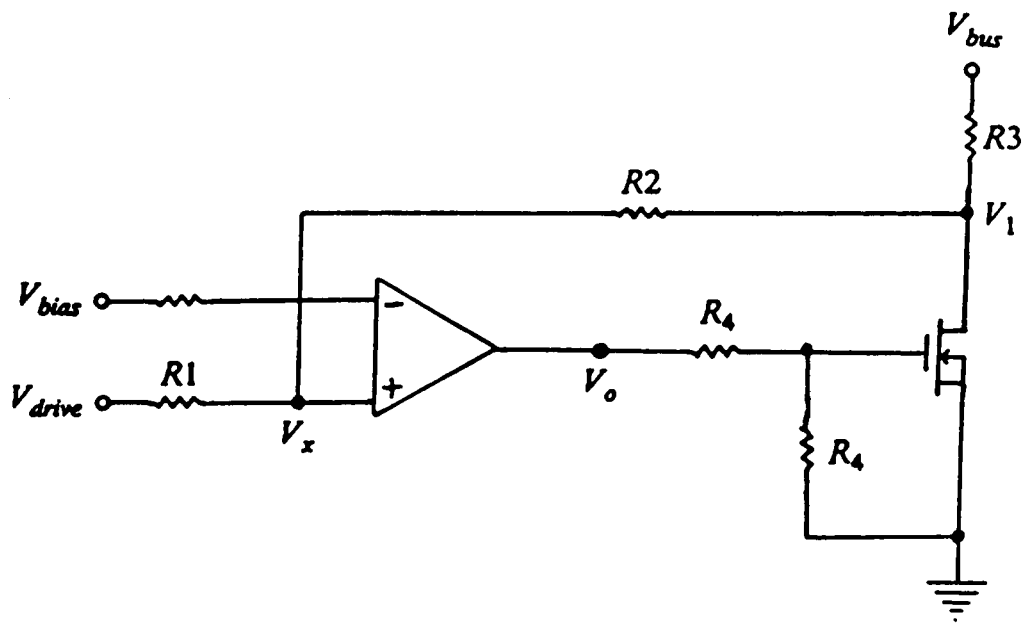Fig. 2.9 COBE sequential shunt regulator circuit
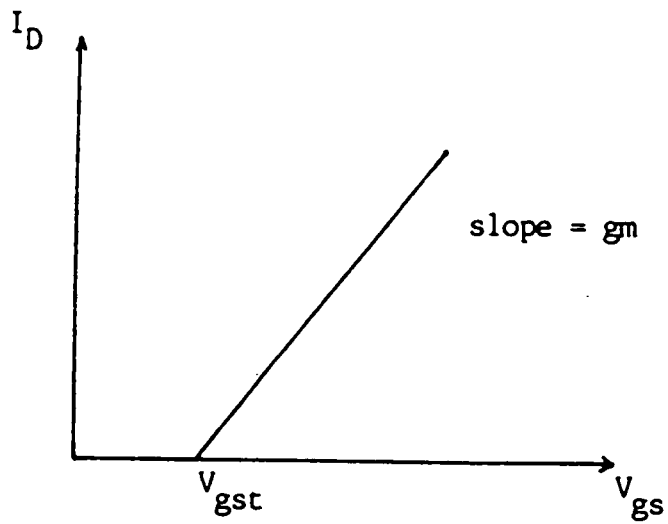
Fig. 2.10 Simlified circuit of one section of Fig. 2.9

Fig. 2.11 Transfer curve of MOSFET

$$V_1 = V_{bus} - gmR3 \left(\frac{V_o}{2} - V_{gst} \right)$$

where the gain and gm represent the open-loop gain of the op-amp and the transconductance of MOSFET, respectively.

From the above three equations, $V_{gs}(=\frac{V_o}{2})$ can be expressed as a function of V_{drive}, V_{bias} and V_{bus}. Since the parameter values are given as R1 = 12.4KΩ, R2 = 2.2MΩ, R3 = 20Ω, gain = 200000, and gm = 4, and after coefficient approximations, V_{gs} becomes

$$V_{gs} = \frac{R1 + R2}{gmR1R3} \left(V_{drive} - V_{bias} \right) + \frac{1}{gmR3} \left(V_{bus} - V_{drive} \right) + V_{gst}$$

For each pair of shunt elements in the saturation region,

$$I_{sh} = 2\,gm\left(V_{gs} - V_{gst} \right)$$

For the shunt element in the ohmic region,

$$I_{sh} = 2\,\frac{V_{bus}}{R3 + R(dson)}$$

For the shunt, the drive voltage should be greater than its bias voltage to have current flow. Since the bias voltage increases as V_{bus} increases, the drive voltage should also increase. When V_{bus} is greater than V_{ref} (shunt), which is 28.18V in this model, the drive voltage should be greater than bias 1 voltage of the shunt to turn on its element 1.

The V_{bias} is determined by the voltage divider circuit shown in Fig. 2.9.

$$V_{bias1} = \frac{V_{bus}\left(R_x + R_1 \right)}{R_x + R_1 + R_2 \cdots + R_{12} + R_y}$$

33

$$V_{bias2} = \frac{V_{bus}(R_x + R_1 + R_2)}{R_x + R_1 + R_2 \ldots + R_{12} + R_y}$$

The V_{drive} is assumed as

$$V_{drive} = K + slope(V_{bus} - 28.18)$$

and the values of K and slope were chosen to turn on each shunt element at different bus voltages, and to have the proper slope for I_{sh} versus V_{bus}. Since each MOSFET enters the ohmic region when $I_{sh} \cong 1.4A$, this characteristic can be implemented by limiting the V_{gs} to

$$0 \leq V_{gs} \leq 3.35$$

assuming that the transfer gain of the MOSFET is 4 and V_{gst} is 3V. The total shunt current is

$$I_{sh} = I_{sh1} + I_{sh2} + \ldots\ldots + I_{sh12}$$

Example of Simulation

A system consisting of the solar array model, constant-power load model and the sequential-shunt regulator model is configured.

In this simulation (Fig. 2.12), a constant power load decreases linearly from 850W to 530W. This decrease causes the bus voltage to rise and the first shunt section to turn on. Just before the first shunt section reaches saturation, the second shunt section turns on to take the additional shunt current. Since the shunt sections turn on sequentially according to the bus voltage, only one shunt section operates in the linear region (saturation region of MOSFET).
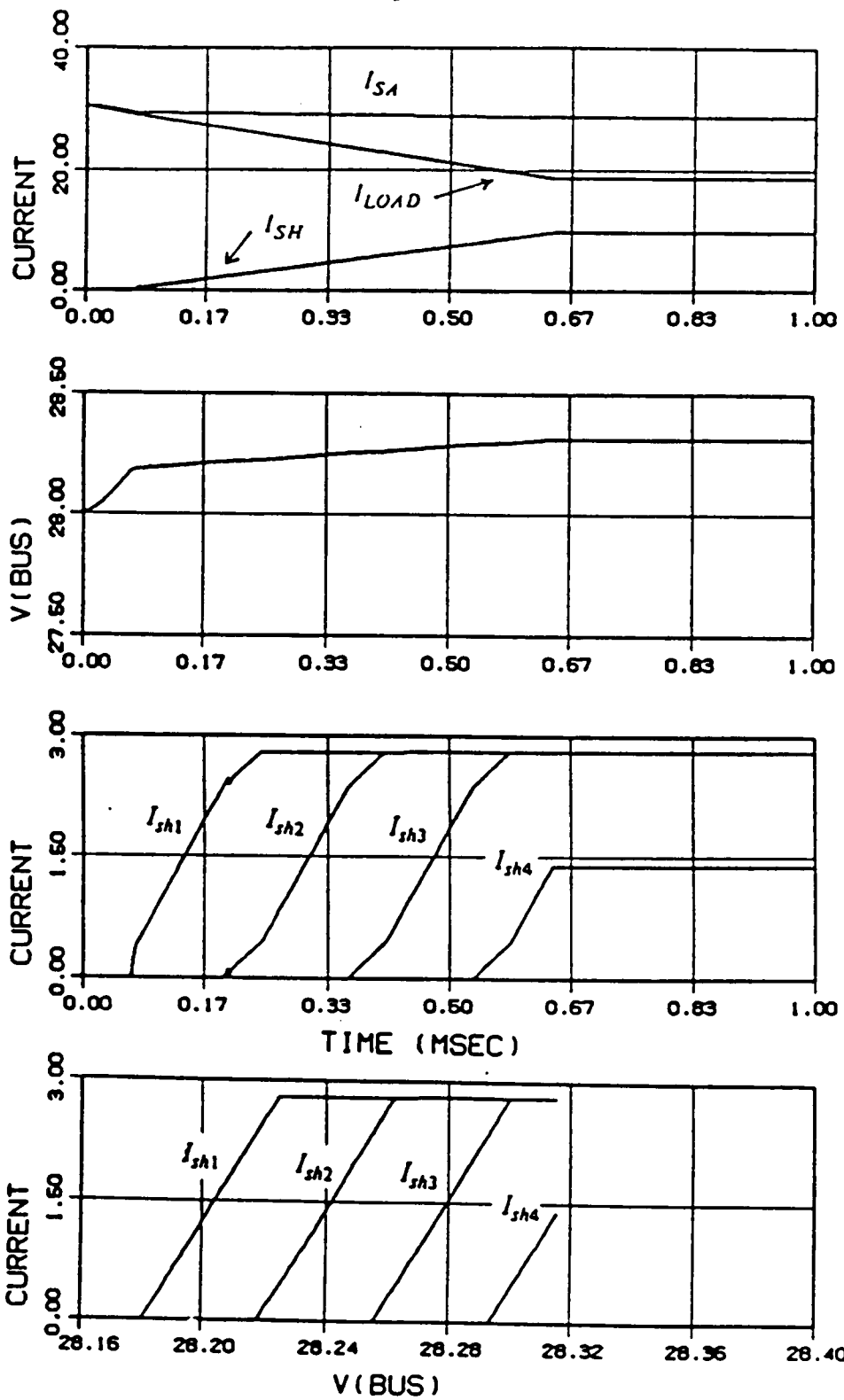
CHAPTER 2

Fig. 2.12 Simulation of COBE sequential shunt regulator

From the simulation result, the power dissipation in the MOSFETs can be calculated as follows. For three pairs of the MOSFETs in the ohmic region, the power dissipation becomes

$$3 \times (I_{sh1}) R(dson) = 3 \times 2.8 \times 0.18 = 1.512W$$

The fourth element is on the linear region. Therefore, the power dissipation in the element is

$$I_{sh4} V_{ds} = 1.4 \times 14 = 19.6W$$

The total power dissipation of the shunt transistors is 21.112 W.

If a full shunt system with these 12 elements in parallel is considered, the power dissipation of the transistors in this system becomes

$$V_{ds} = V_{bus} - I_{sh}(\text{one element}) R3 = 28.18 - \frac{9.8}{12} \times 20 \cong 11.8V$$

$$12 \times I_{sh}(\text{one element}) V_{ds} = 12 \times 0.82 \times 11.8 \cong 116.1W$$

From this comparison, the advantage of the sequential shunt can be clearly explained.

2.3.3 Battery Model

In spacecraft which uses a solar array as the main source of energy, the storage battery is the critical source of continuous power which responds to peak and eclipse power demands.

Nickel-cadmium (Ni-Cd) batteries have been widely used in many spacecraft. There are some major advantages of Ni-Cd batteries, compared to lead-acid batteries:

- Ability to be overcharged without damage
- Ability to spend long periods without damage when only slightly charged
- Mechanically more rugged, making them more transportable
- Ability to withstand freezing without damage

An equivalent circuit model of an electrochemical battery cell (Ni-Cd) has been recently developed in [10]. This circuit model facilitates the accurate analysis of spacecraft power systems with this battery. Computer-oriented battery models used in the past rely on table-look-up techniques or curve-fitting methods. These models represent rather static conditions. Using the equivalent circuit model, dynamic conditions, as well as self-discharge conditions, can be easily calculated.

The electrochemical cell displays changes in the terminal voltage, due to its internal polarization process. Polarization is divided into three general types:

- Ohmic Polarization - Voltage drop proportional to current flow, due to resistive effects of plates and electrolytes

- Activation Polarization - Voltage drop logarithmically related to current flow, due to the effects of double layers

- Concentration Polarization - Voltage drop logarithmically related to current flow, due to ionic transport effects by diffusion in electrolytes

Ohmic polarization, caused by plate and electrolyte resistances, can be represented by a resistive circuit element. The activation polarization and overcharge dissipation is represented with diodes.

The equivalent circuit shown in Fig. 2.13 is a lumped-element type that consists of a small number of nonlinear electrical elements. The charge transfer (realistically simulated by front-to-back diodes), the energy storage effect induced by the double layers, and the electrochemical reactions can only be represented by capacitances. The resistance, R_s, represents the resistive elements of the cells. The front-to-back diodes, D_1 and D_2, describe the charge-transfer effect, according to the equation, as

$$I_1 = K_1 \{ exp (K3 \times V1) - exp (-K3 \times V1) \}$$

The coefficients, K_1 and K_3, are determined from the experimental data.

The shunt diode, D_3, represents the self-discharging of the battery cell. The parameter values of the I-V equation of this diode differ from those of D_1 and D_2 and are also obtained from the experimental data.

The capacitance values, C_1 and C_2, vary according to the equation below. It is assumed that the values are statistically distributed with regard to their current contribution effects.

$$C = A \, exp \{ -B (V - V_M)^2 \} + D$$
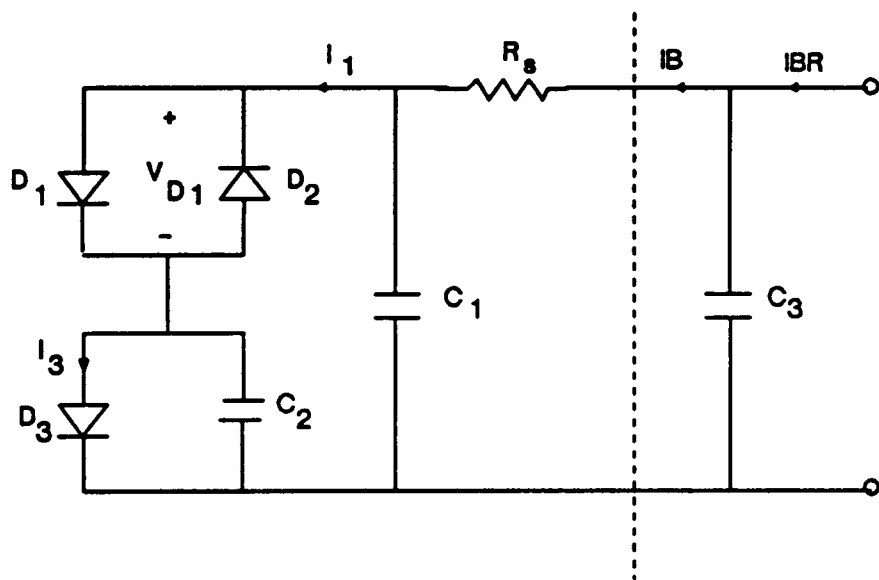
Fig. 2.13 Equivalent circuit model of battery cell

where C = capacitance value in farads

       V = actual voltage

     V_M = median voltage level

     A = capacitance in farads at $V = V_M$

     B = distribution constant

     D = minimum capacitance in farads

The parameter values, A, B, V_M and D, can be obtained from the experimental data.

Model Generation

As shown in Fig. 2.13, the capacitor, C_3, is added to model the COBE circuit. From the diode characteristic,

$$I_1 = K_1 [\exp (K_3 V_{D1}) - \exp (-K_3 V_{D1})]$$

$$I_3 = K_1 [\exp (K_3 V_{D3}) - 1]$$

The coefficients, K_1 and K_3, can be obtained by the following formula with given parameter values, I_0, k_2 , T, V_0, and L.

$$K_1 = \frac{I_0 \exp [40.27 k_2 \{ 1 - 459/(T + 519) \}]}{\exp (40.27 V_0/L) - 1}$$

$$K_3 = \frac{20900}{L (T + 459)}$$

where I_0 = reference diode current in amperes at

          60° F and V_0

     V_0 = reference diode voltage at $60^o F$ and I_0

     T = actual diode temperature ($^o F$)

k_2 and L are constants which may be determined

from analysis of experimental data

The parameter values, I_0, k_2, V_0 and L, for the diodes D_1 and D_2 differ from those values of diode D_3. The values in this model were obtained from the data shown in [10].

From the circuit diagram,

$$C_3 \frac{dV_{c3}}{dt} = IBR - IB$$

$$C_1 \frac{dV_{c1}}{dt} = IB - I_1$$

$$C_2 \frac{dV_{c2}}{dt} = I_1 - I_3$$

Example of Simulation

Figure 2.14 shows the battery output voltage versus the state-of-charge (Ampere-Hour) of a Ni-Cd battery composed of 18 serial cells. For this simulation, the circuit model shown in Fig. 2.13 was used to obtain the battery's terminal characteristic. This simulation result was similar to the original graph shown in [10].
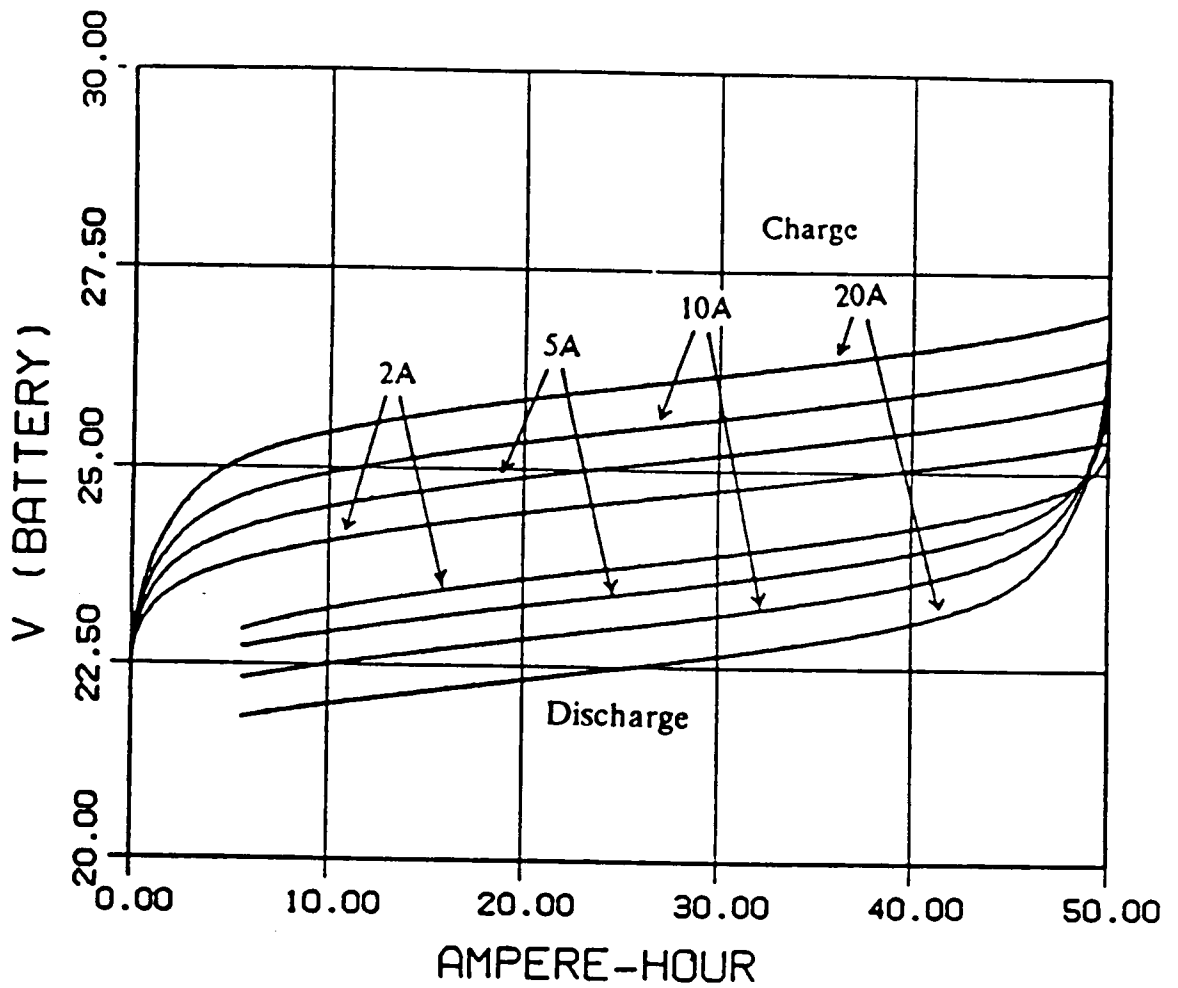
Fig. 2.14 Simulation of battery charge and discharge
characteristic for 18 cells at 40°F

2.3.4 Battery Charger Model

The basic functional requirement of the battery charger is to charge the battery when excess power from the solar array is available and the battery is not fully charged. Battery chargers in high-power systems use switching regulators to achieve highly efficient and low-heat dissipation. Since a series-pass charger is widely used in many spacecraft, the series-pass charger used in the COBE power system is modeled in this study.

Model Generation

Figure 2.15 shows a typical circuit of a series pass charger. The charger circuit is modeled and simulated in this section.

When the solar array exits from the eclipse, it produces excess power. The battery charger senses that the bus voltage is higher than its reference voltage and starts to charge the battery. The maximum charging current is limited by a feedback signal from the voltage across resistor R_1. When V_{bus} is higher than V_{ref}, the voltage at V_x becomes lower than V_2. Then V_3 is decreased so the P-channel MOSFET can finally turn on to allow the charging current, i_1, to flow. When the charge current flows, V_{bus} decreases according to the solar array's I-V characteristics. Then, V_x rises again and V_3 rises slightly to reduce I_1 . As a result, I_1 is controlled at the level of available excess power.

In the model program, V_3 can be expressed as

$$V_3 = V_3 - SR * TINC \quad \text{when } V_x > V_2$$

$$V_3 = V_3 + SR * TINC \quad \text{when } V_x < V_2$$

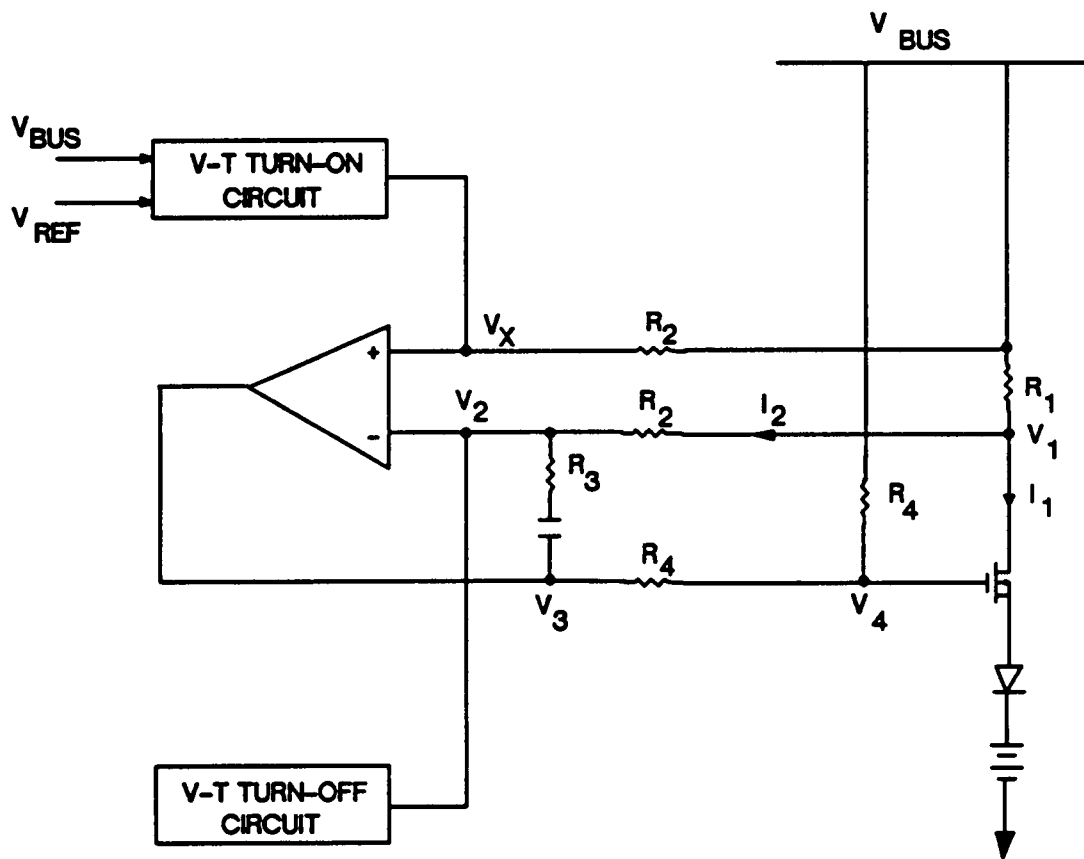$$V(\text{min}) \leq V_3 \leq V(\text{max})$$

Fig. 2.15 COBE battery-charger circuit

where SR = slew rate of op-amp

TINC = time step of simulation

V(min),V(max) = saturation voltages of op-amp

By using the basic circuit-analysis technique, the following equations are obtained.

$$V_4 = \frac{V_{bus} + V_3}{2}$$

$$I_2 = \frac{V_2 - V_c - V_3}{R_3}$$

$$V_1 = V_{bus} - R_1(I_1 + I_2)$$

When the MOSFET operates in the linear region, the drain current is expressed as

$$I_d = gm(V_{gs} - V_{gst})$$

where I_d = drain current

gm = forward transconductance of MOSFET

V_{gst} = gate-threshold voltage

When the battery voltage reaches a certain value, the MOSFET becomes saturated and the charging current is proportional to the MOSFET drain-source voltage, V_{ds}. Assuming that saturation occurs when the battery voltage reaches $V_{bat}(\text{max}) - 0.1V$, the charging current during saturation of the MOSFET can be expressed as

$$I_{ch} = gm_2 \, V_{ds} = gm_2 \left[\, V_{bat}(\text{max}) - V_{bat} \, \right]$$

when

CHAPTER 2

$$V_{bat}(\max) - 0.1V \leq V_{bat} \leq V_{bat}(\max)$$

where gm_2 is the inverse of on-resistance during MOSFET saturation.

The V-T turn-off circuit turns off the charger whenever the voltage or temperature of the battery, or the ampere-hour integrator, reaches the preset limit. The trickle charger, a small constant current charger, turns on to compensate for the self-discharging current of the battery when the battery is fully charged.

A simulation example of this charger is shown in COBE system simulation in Chapter 5.

CHAPTER 3

LARGE-SIGNAL ANALYSIS OF SPACECRAFT POWER SYSTEMS

3.1 Introduction

A large-signal analysis of the direct energy transfer (DET) power system is performed to predict the main bus dynamics in various modes of operation. Stability criteria for the operating points on the solar array I-V curve are identified in each mode. The trajectories of the bus voltage and solar array output current are investigated in such cases as load change and equipment failure.

Solar arrays, as the primary power source for a spacecraft, have a highly nonlinear output I-V characteristic. The operating point of the solar array is determined by such factors as the array's temperature, illumination level and the load characteristics of the power conditioning equipment. Several modes of operation exist due to variations of the illumination level and load demands.

This nonlinear source, coupled with nonlinear load characteristics, often results in multiple equilibrium points, of which only one is desired. An

undesired oscillation or a sudden voltage drop in the solar array's output may occur, depending on the system's operating conditions.

In this chapter, a large-signal stability analysis of the solar array power system is reviewed to analyze dynamics of practical spacecraft power systems such as the regulated-bus system and semi-regulated (sunlight-regulated) bus system using the DET concept. The region, where the operating point of the solar array in the DET system is located, is identified. Using the dc characteristics of the power conditioning equipment, the spacecraft power system operating in the shunt mode, battery-charge mode and battery-discharge mode is analyzed to show how the power conditioning equipment stabilizes the system in each mode. The system's dynamic behavior in the deadband mode is investigated using the large-signal analysis technique. The solar array/battery lockup phenomenon is analyzed and graphically depicted. System behavior after a shunt failure and battery-discharger failure are investigated to provide design considerations for the fault protection and redundant systems.

The analyses performed in this chapter are verified through simulations using the models described in [8].

3.2 Review of Stability Analysis of the Equilibrium Points of the Solar Array Power System

A spacecraft power system usually has many load converters to feed various dc equipment requiring different input voltages. Since these load converters regulate the output voltage with varying input voltage, they can be treated as a constant-power load, assuming that the converter is lossless. The solar array source with a resistive load is basically stable, so only the system with a constant-power load is analyzed.

Since the large-signal analysis of the solar array system with a constant-power load was performed in [2, 13], the analysis is reviewed to

expand for the DET power system having such power conditioning equipment as the shunt regulator, battery charger and battery discharger.

To analyze the solar array power system with a constant-power load, dc characteristics of a simplified solar array power system, shown in Fig. 3.1, were employed. In Fig. 3.1, the static load line characteristic exhibits a negative incremental resistance in the midsection. Voltage V_R is the array's minimum voltage for the converter to regulate its output voltage. As shown in the figure, three equilibrium points exist in the system. Below V_R, the converter behaves as a resistive load to the solar array, and is defined as Region #1. In Region #2, the magnitude of the slope of the load line is larger than that of the source line, while in Region #3, the magnitude of the load line is smaller than that of the source line. A large-signal analysis was carried out using a second-order system, as shown in Fig. 3.2. The LC low-pass filter in the model represents actual physical elements in the system, such as the cable impedance and the bus filter. To analyze the stability of the equilibrium point in each region, the state-plane analysis of the nonlinear system in Fig. 3.2 was introduced in [4] and reviewed as follows.

Defining the states, $x = [i_L \; v_C]^T$, and introducing small-signal perturbations on the states, two state equations were obtained:

$$L \frac{d\hat{i}_L}{dt} = r_S \hat{i}_L - \hat{v}_C \tag{3.1}$$

$$C \frac{d\hat{v}_C}{dt} = \hat{i}_L - \frac{1}{r_L} \hat{v}_C \tag{3.2}$$

Here, r_S and r_L represent the incremental resistances (tangential slope) of the solar array's output characteristic and load line, respectively, at the equilibrium point.
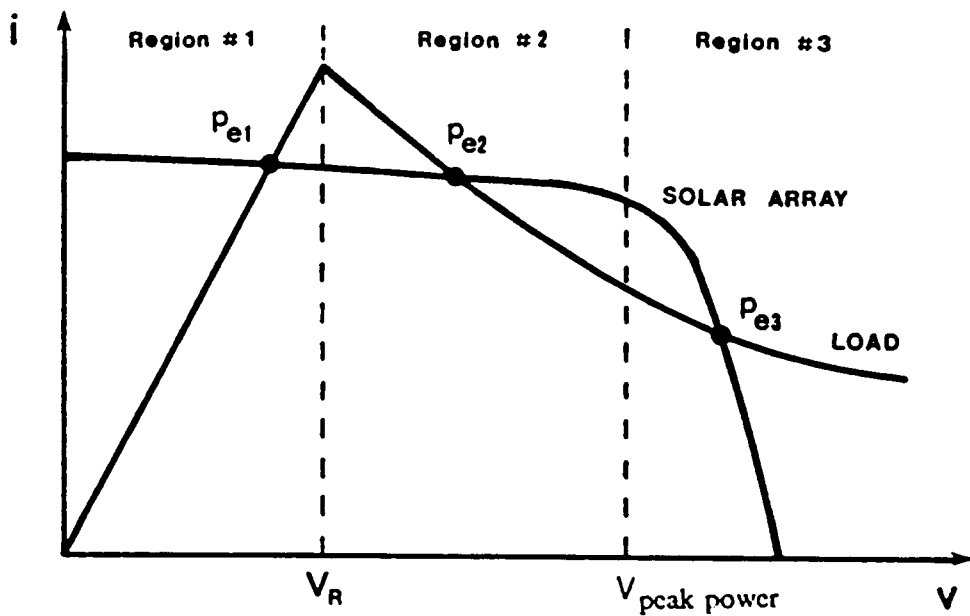
Fig. 3.1   Representation of a solar array power system
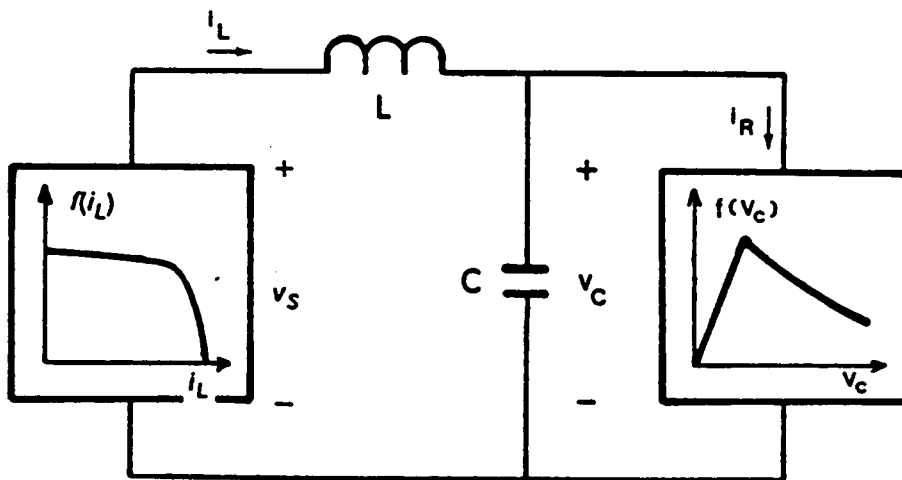with a switching regulator load line

Fig. 3.2   Equivalent circuit model of the system in Fig. 3.1
including LC filter

Eigenvalues of the system were obtained from Eqs. (3.1) and (3.2) as follows:

$$\lambda_1, \ \lambda_2 = \frac{1}{2} \cdot \left[(\frac{r_S}{L} - \frac{1}{r_L C}) \pm \sqrt{(\frac{r_S}{L} - \frac{1}{r_L C})^2 - \frac{4}{LC}(1 - \frac{r_S}{r_L})} \right] \quad (3.3)$$

From Eq. (3.3), the stability of equilibrium points in three different regions were defined.

In Region #1 : $r_L > 0$, $r_S < 0$

The equilibrium point, P_{e1}, is stable and is either "node" (real) or "focus" (complex).

In Region #2 : $r_L < 0$, $r_S < 0$, $|r_S| > |r_L|$

Two eigenvalues are real but of opposite sign. Point P_{e2} is a "saddle" and is unstable.

In Region #3 : $r_L < 0$, $r_S < 0$, $|r_S| < |r_L|$

The stability of point P_{e3} depends on parameter values L and C.

In Regions #1 and #2, the parameter values, L and C, do not have any effect in determining the stabilities of the equilibrium points in the regions. In region #3, the system stability depends on the parameter values L and C, as well as r_S and r_L. The criterion of the stability can be obtained from the following analysis.

From Eq. (3.3), when the eigenvalues are complex, that is, when

$$\left(\frac{r_S}{L} - \frac{1}{r_L C}\right)^2 \;<\; \frac{4}{LC}\left(1 - \frac{r_S}{r_L}\right) , \qquad (3.4)$$

the stability of the system depends on the real part of the eigenvalue.

$$\text{if } \left(\frac{r_S}{L} - \frac{1}{r_L C}\right) \;<\; 0 \quad \text{stable} \qquad (3.5)$$

$$\text{if } \left(\frac{r_S}{L} - \frac{1}{r_L C}\right) \;>\; 0 \quad \text{unstable} \qquad (3.6)$$

When the eigenvalues are real, that is,

$$\left(\frac{r_S}{L} - \frac{1}{r_L C}\right)^2 \;\geq\; \frac{4}{LC}\left(1 - \frac{r_S}{r_L}\right) \qquad (3.7)$$

Since the magnitude of the second term, square root term, is always less than the first term, the sign of the first term determines the stability of the system. That is,

$$\text{if } \left(\frac{r_S}{L} - \frac{1}{r_L C}\right) \;<\; 0 \quad \text{stable} \qquad (3.8)$$

$$\text{if } \left(\frac{r_S}{L} - \frac{1}{r_L C}\right) \;>\; 0 \quad \text{unstable} \qquad (3.9)$$

Therefore, the same stability criteria can be used for both cases of the complex eigenvalues and the real eigenvalues. As a result, from Inequalities (3.8) and (3.9), when $\frac{L}{C} < |r_S r_L|$, the system is stable, and when $\frac{L}{C} > |r_S r_L|$, the system is unstable.

From the above results, the equilibrium point in Region #1 is always stable, but the voltage cannot be used as the input of the load converter.

The equilibrium point in Region #2 is always unstable (saddle point), regardless of parameter values. Thus, the equilibrium point in Region #3 is the only desirable operating point and its stability is dependent on the values of L and C.

The large-signal behavior can be observed from the system's state-plane trajectories. The state trajectories, as shown in Fig. 3.3, were derived for each equilibrium point using the above two state equations in Eq. (3.1) and (3.2) [2, 13]. To obtain the trajectories, isoclines were derived for each equilibrium point. Near the equilibrium points, the trajectories follow the slope of eigenvectors of the system, γ. A **separatrix** [14], which divided two groups of trajectories, was identified. The steady-state operating point of the system which has initial conditions in the left-hand side of the separatrix, becomes point P_{e1}, while the operating point of the system which has initial conditions in the right-hand side of the separatrix becomes P_{e3}, assuming that the point P_{e3} is stable.

Since the equilibrium point, P_{e3}, can be stable or unstable, the following six cases are set up for the computer simulations.

Case i P_{e1} - node, P_{e3} - node

Case ii P_{e1} - node, P_{e3} - focus

Case iii P_{e1} - node, P_{e3} - unstable

Case iv P_{e1} - focus, P_{e3} - node

Case v P_{e1} - focus, P_{e3} - focus

Case vi P_{e1} - focus, P_{e3} - unstable

However, an investigation of **cases i, ii** and **iii** is sufficient to understand the behaviors of the system. P_{e1} can be a focus only when the inductance
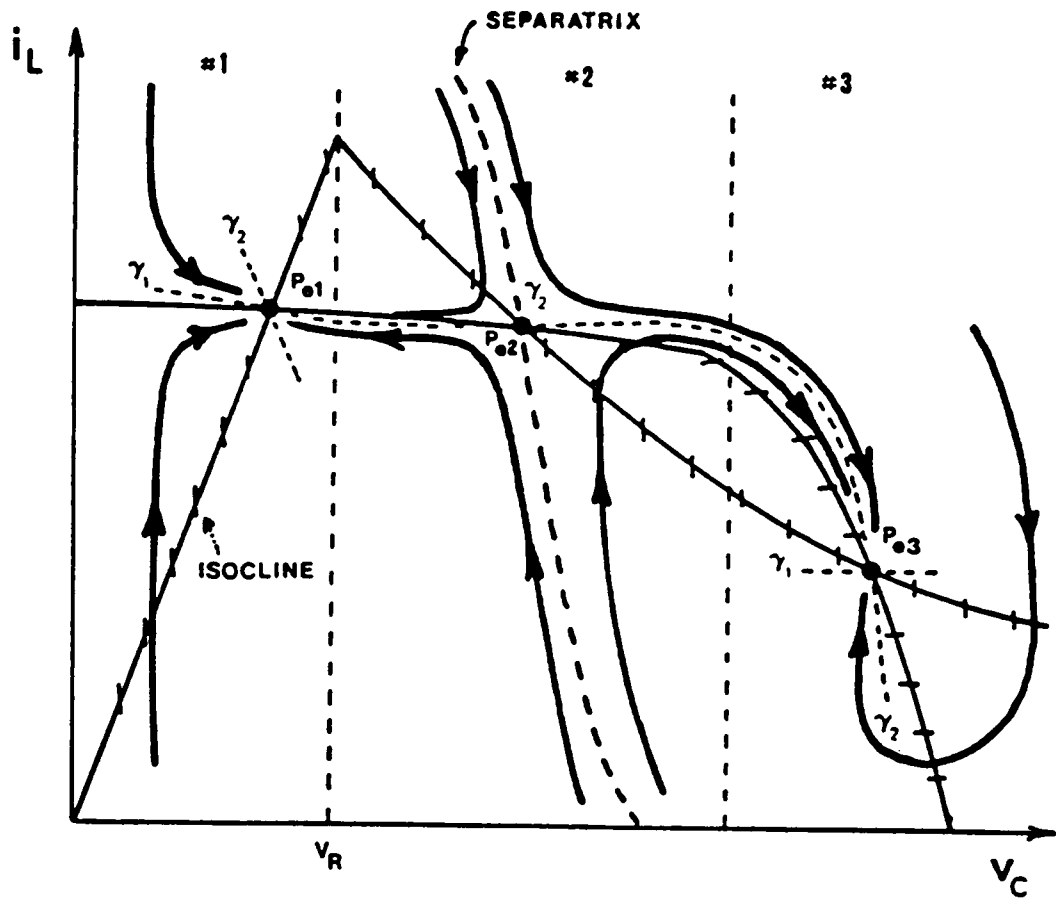
Fig. 3.3 State-plane trajectories of the system in Fig. 3.2

value, L, is comparable to the capacitance value, C. The simulation results of these cases, with the following system operating conditions, are shown in Figs. 3.4a-3.4c.

The short-circuit current of the solar array, I_{sc}, is 45.41A, the open-circuit voltage, V_{oc}, is 32.0V, and the maximum power is 1050 W. The constant-power load line is set to 850 W, and the boundary of Region #1 and #2, V_R, is 15V. The values of r_S and r_L at the equilibrium points in each region are listed in the following table.

	P_{e1}	P_{e2}	P_{e3}
I_L	45.38	45.02	30.34
V_C	12.03	17.31	28.02
r_S	-64.92	-37.3	-0.20
r_L	0.27	-0.56	-1.47

Cases i (P_{e3} node) and ii (P_{e3} focus) are shown in Figs. 3.3a and 3.4b. The trajectories from the initial points in the left-hand side of the separatrix (P_1 through P_6) converge to P_{e1}, and those in the right-hand side of the separatrix (P_7 through P_{12}) converge to P_{e3} . Figure 3.4c illustrates the case when P_{e3} is unstable and the state trajectory converges to stable equilibrium point, P_{e1}, which is not a desired equilibrium point.

From the above analysis and simulation, it was shown that the dynamic behavior of the solar array power system with a constant-power load depended on the stability of the equilibrium points, which was determined by the eigenvalues of the two state equations.
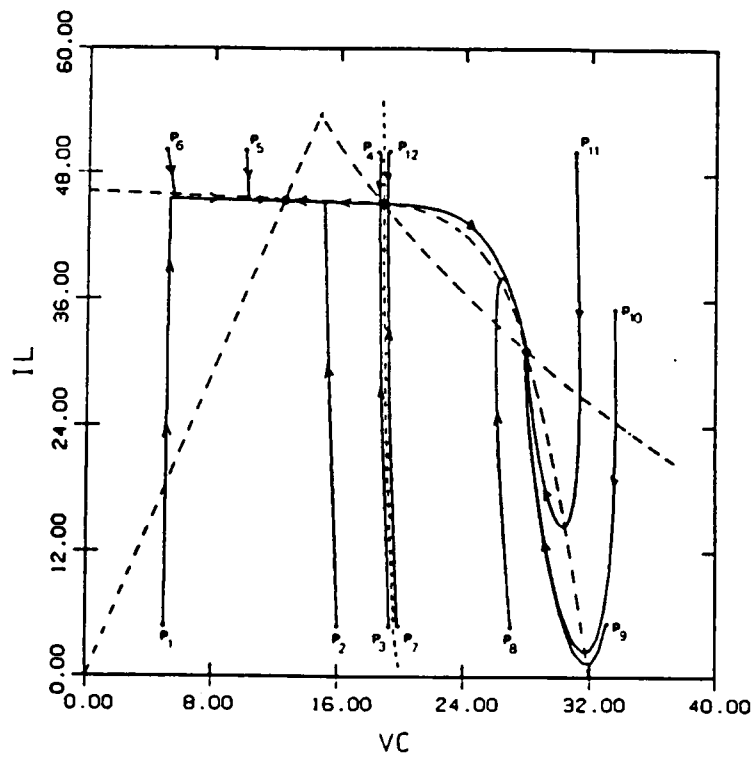
Fig. 3.4(a) Simulation of state-plane trajectories for the case where
the equilibrium point P_{e3} is 'stable node'
$(L = 10\mu H, C = 500\mu F)$
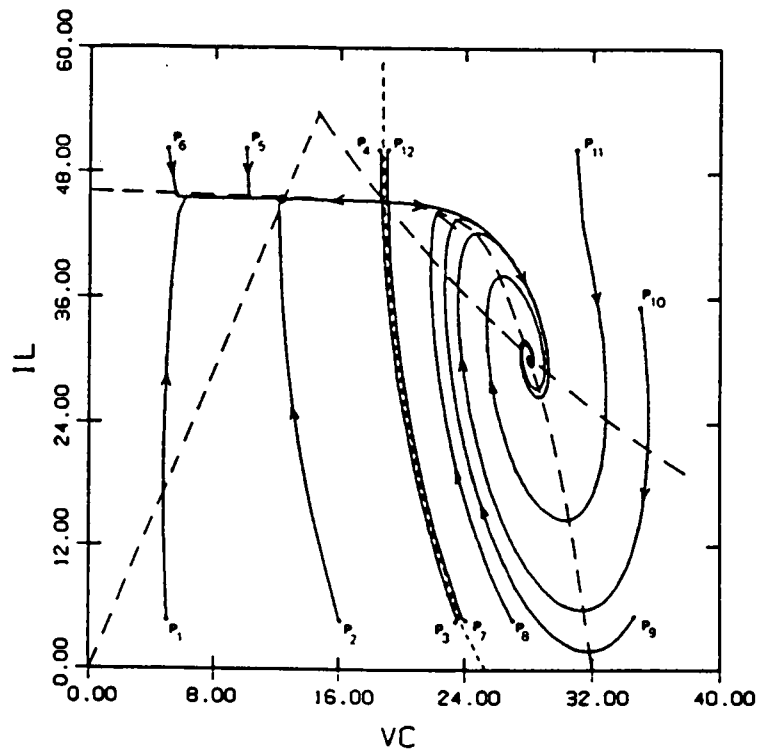
Fig. 3.4(b) Simulation of state-plane trajectories for the case where
the equilibrium point P_{e3} is 'stable focus'
$(L = 30\mu H, C = 500\mu F)$
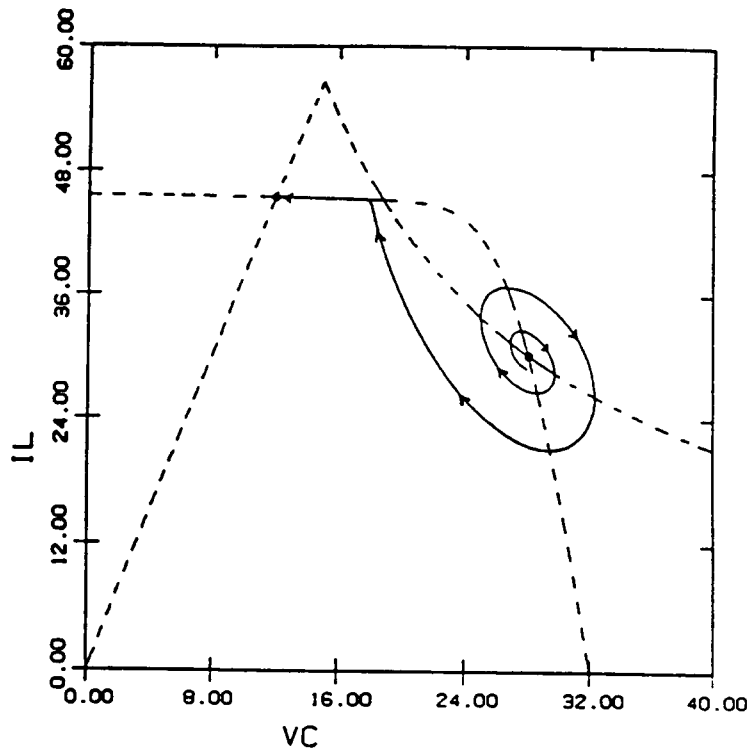
Fig. 3.4(c) Simulation of state-plane trajectories for the case where
the equilibrium point P_{e3} is 'unstable'
$(L = 150\mu H, C = 500\mu F)$

3.3 Dynamic Behavior of the Regulated-Bus System

The regulated-bus system using the DET concept has four different modes of operation throughout an orbit cycle: a shunt mode, battery-charge and -discharge modes and a deadband mode. In the regulated-bus system, the power conditioning equipment, such as the shunt regulator, battery charger and discharger, not only balance the power but also regulate the bus. Each regulator is activated at a specific range of bus voltage to maintain the bus at a desired voltage level.

Before the analysis is performed, the solar array's operating region is identified for the DET power system. Since the solar array is degraded during the mission period, two solar array I-V curves exist as shown in Fig. 3.5, during the sunlight period and at its beginning- and end-of-life, exist as shown in Fig. 3.5. The bus regulation voltage should be selected near the peak power voltage, V_{pp1}, which is the peak power voltage at the end-of-life, to obtain maximum available power at the end-of-mission. By doing so, the system can have an energy balance throughout the mission period. Suppose that the bus regulation is selected near the peak power voltage, V_{pp2}, of the solar array's beginning-of-life. Then, although the solar array can provide more power at Point B than at Point A at the beginning-of-life, the power at the end-of-life becomes very small, because the operating point of the solar array is at Point C. This implies that the solar array's operating point stays in Region #2 throughout the mission period.

Since the operating point in Region #2 is unstable in the case of a constant-power load, as shown in Section 3.2, it is important to analyze
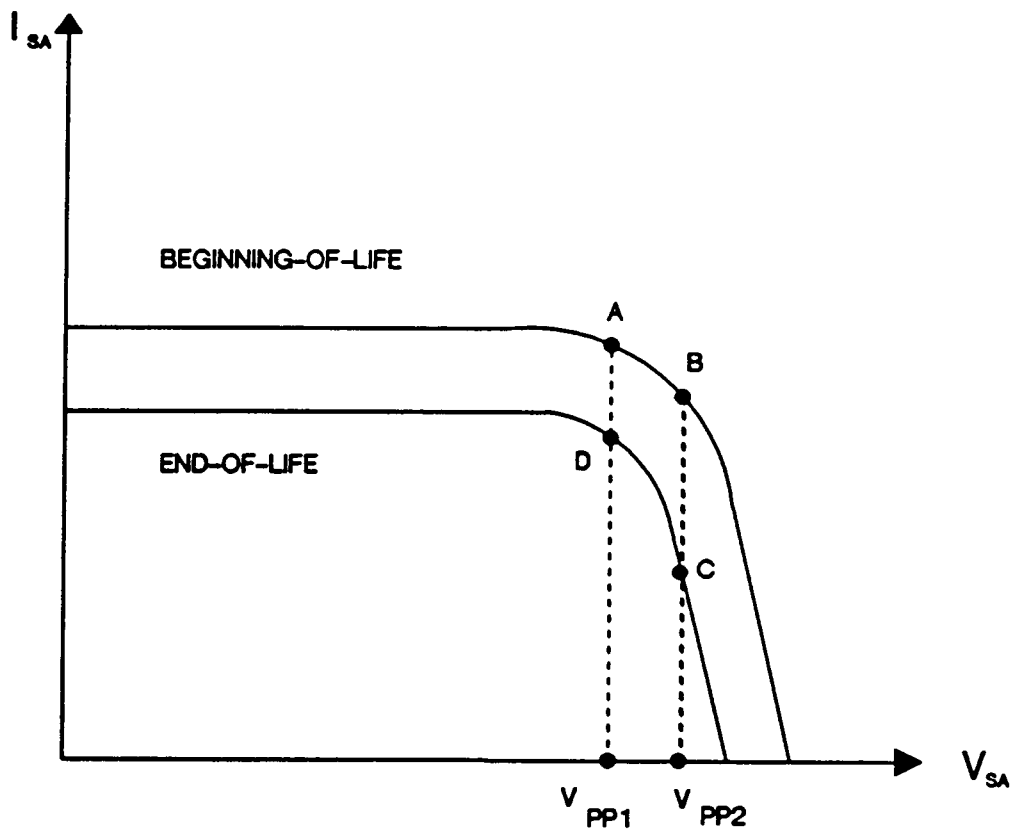
Fig. 3.5 Two solar array I-V curves at the beginning-of-life and end-of-life

59

how each piece of power conditioning equipment not only makes the system stable in different modes of operation, but also how it improves the system dynamics for the constant-power load. In the DET system, the bus dynamic behavior is mainly determined by the solar array output current and voltage, so the simplified second-order system model, using dc characteristics of the source, load and power conditioning equipment, will be used to analyze the system's dynamic behavior in each mode of operation. The load of the system is assumed to be of a constant-power type throughout the analyses in the following sections.

3.3.1 Dynamic Behavior of the System in Shunt Mode

In the DET system and many other spacecraft power systems, the shunt regulator is used to limit the increase of the bus voltage. Figure 3.6 illustrates the system in the shunt mode of operation. The shunt current can be expressed as a function of the error in the bus voltage, v_C, with the shunt transadmittance, Y_{sh}. For the large-signal analysis of the main bus, the shunt regulator's transadmittance is treated as a simple gain, $G_{sh} = \frac{1}{r_{sh}}$. That is, the dynamic of the shunt regulator itself is ignored to study the system's dynamic behavior. An analysis of the shunt regulator in a frequency domain will be performed in Chapter 4. Then,

$$i_{sh} = \frac{1}{r_{sh}} v_C \qquad (3.10)$$

The state equations at equilibrium points are

$$\frac{di_L}{dt} = \frac{1}{L} (v_S - v_C) = \frac{1}{L} (f(i_L) - v_C) \qquad (3.11)$$
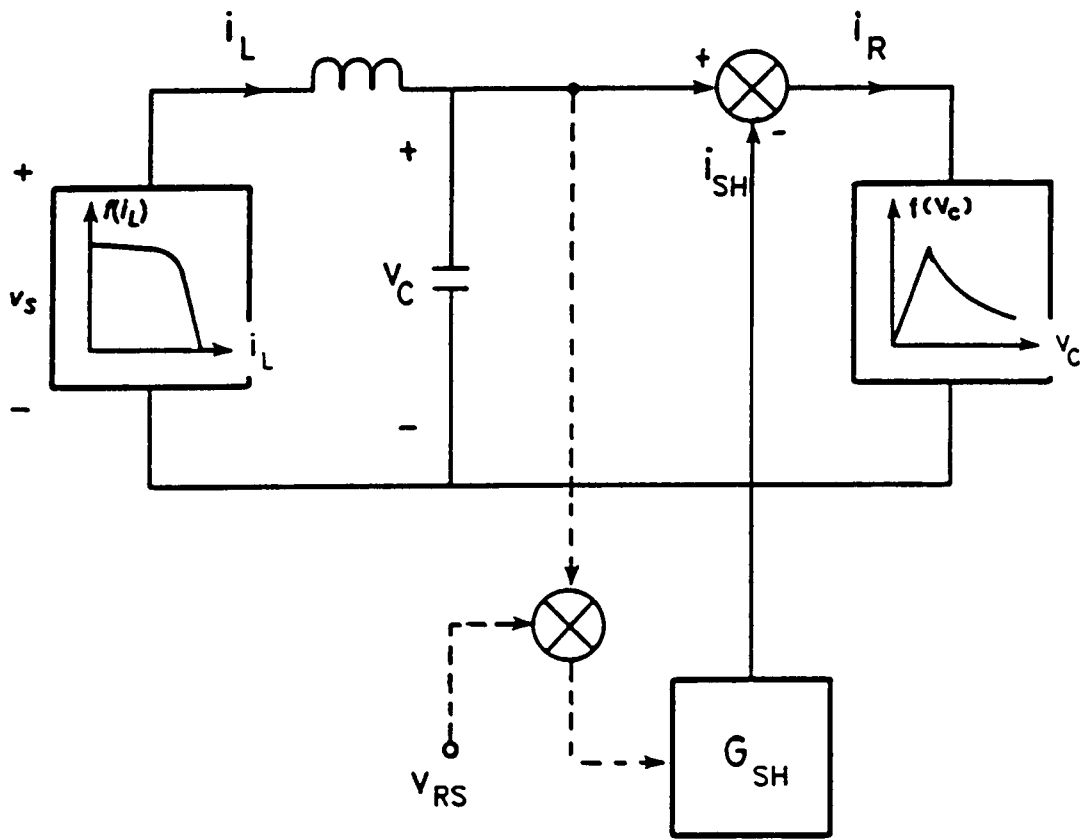
Fig. 3.6   Simplified block diagram of the system in Fig. 3.2
with the shunt regulator (G_{SH} = 1/r_{SH})

$$\frac{dv_C}{dt} \;=\; \frac{1}{C}\,(\,i_L - i_{sh} - i_R\,) = \frac{1}{C}\,(\,i_L - \frac{v_C}{r_{sh}} - f(\,v_C)\,) \qquad (3.12)$$

where $\dfrac{1}{r_{sh}}$ is the shunt regulator's transconductance. Following the same procedures as in the previous derivations in [4, 13], the state equations near the equilibrium point are

$$L\frac{d\hat{i}_L}{dt} \;=\; r_s\hat{i}_L - \hat{v}_C \qquad (3.13)$$

$$C\frac{d\hat{v}_C}{dt} \;=\; \hat{i}_L - (\,1/r_L + 1/r_{sh}\,)\,\hat{v}_C \qquad (3.14)$$

The eigenvalues are obtained as

$$\lambda_1, \;\lambda_2 = \frac{1}{2}\;\cdot\left[(\frac{r_S}{L} - \frac{1}{r_E C}) \pm \sqrt{(\frac{r_S}{L} - \frac{1}{r_E C})^2 - \frac{4}{LC}(1 - \frac{r_S}{r_E})}\,\right] (3.15)$$

where $r_E = r_L \,\|\, r_{sh}$. Since r_{sh} is a very small positive value (the dc gain of the transadmittance of the shunt regulator is designed to be large to have tight dc regulation), r_E becomes a very small positive value. Therefore, when the square root term is real, the absolute value of the term is always less than the other term, $(\dfrac{r_s}{L} - \dfrac{1}{r_E C})$, and the real part of the eigenvalue becomes a large negative value.

If the load converter is locally stable, a system with the shunt regulator activated is stable, regardless of the region in which the operating point is located. This can be explained in two ways. First, the shunt regulator can be viewed as a load to the solar array source. In this case, the total load line becomes a combination of the shunt regulator and a constant-

power load, as shown in Fig. 3.7. The slope of the new load line is a very large positive value above the bus voltage, V_{RS}, at which the shunt regulator is activated. The slope of the new load line is the same as $\frac{1}{r_E}$ above V_{RS}. As a result, the system is always stable whenever the shunt regulator is active.

Alternatively, the system can be analyzed from the view of the constant-power load. In this case, the solar array with a shunt regulator becomes a source to the constant-power load, as shown in Fig. 3.8. Since the incremental resistance of the shunt regulator, r_{sh}, is much smaller than the source impedance of solar array above V_{RS}, the total source impedance is dominated by the incremental resistance of the shunt, when V_C is greater than V_{RS}. The source impedance is much smaller than the incremental resistance of the load, so the system becomes stable, as shown in Eq. (3.3).

From the above analysis, stability in the shunt mode is determined by the dc gain of the transadmittance of the shunt regulator. The system's stability condition is $(\frac{r_s}{L} - \frac{1}{r_E C}) < 0$. In order for the system to be stable, regardless of the parameter values of L and C, the condition becomes

$$|r_{sh}| < |r_L|$$

This condition makes the slope of the total load line positive.

3.3.2 Dynamic Behavior of the System in the Battery-Charge Mode

The battery-charger is activated when the bus is higher than the charger's reference voltage, V_{RBC}, and the battery is not fully charged.
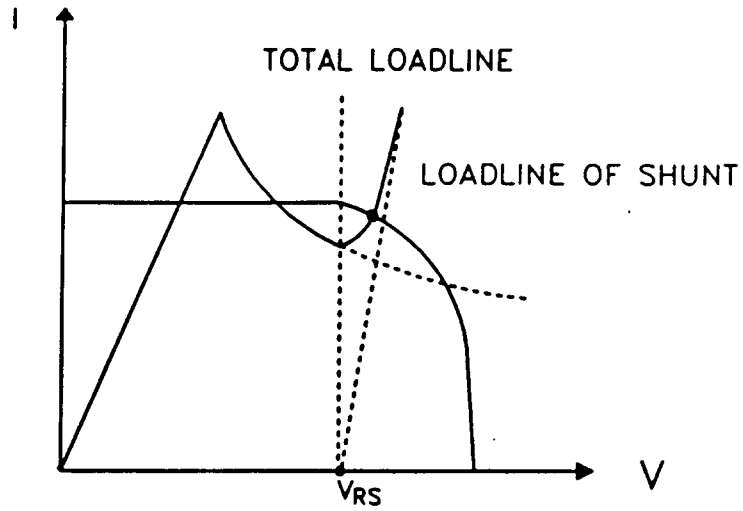
Fig. 3.7 I-V curves of solar array source and load (shunt +
constant power load) in shunt mode
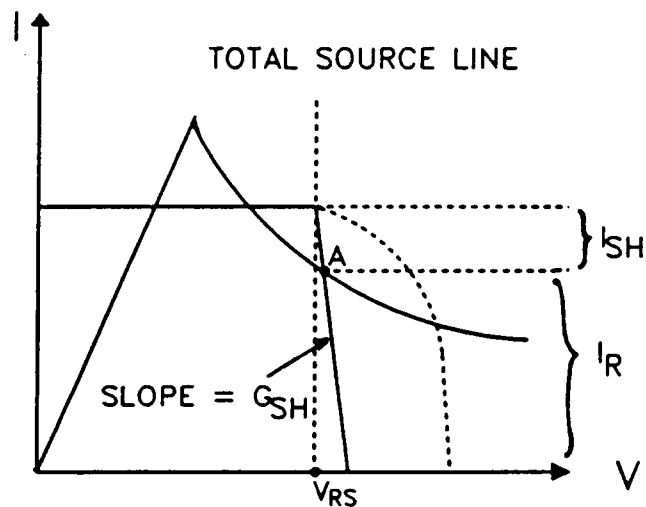
Fig. 3.8 I-V curves of source (solar array + shunt) and
constant power load in shunt mode

Before the charging current reaches a current limit, the bus voltage is regulated by the charger. This period is called the charger's **bus voltage regulating mode.** When the charger is in this mode, the function of the battery charger is the same as the shunt regulator from the viewpoint of bus dynamics. During this mode, the battery charger takes the excess power from the solar array to regulate the bus voltage, as well as to charge the battery. The charge current variation in this mode depends on the bus voltage and the input admittance of the battery charger:

$$\hat{i}_{ch} = Y_{BC}\, \hat{v}_C \qquad\qquad (3.16)$$

If only the dc characteristic of the charger is considered, the input admittance of the charger can be expressed as a simple gain, $G_{BC} = \dfrac{1}{r_{BC}}$. (The analysis of the charger in the frequency domain will also be performed in Chapter 4.) The expression of the eigenvalues are then the same as Eq. (3.15), with $r_E = r_L \,\|\, r_{BC}$. The charger is also assumed to be locally stable. Therefore, the load line of the charger (Fig. 3.9) in this mode is similar to that of the shunt regulator, as shown in Fig. 3.7.

The condition of the system stability in this mode is similar to that of the shunt mode, that is, $(\dfrac{r_S}{L} - \dfrac{1}{r_E C} < 0)$.

When the charging current reaches a preset current limit and the solar array still produces excess power, the charging current is regulated at its limit value. This period is called a charger's **charging current regulating mode.** Once the charger enters this mode, the switching-mode charger behaves like a constant-power load, because the output current is regulated and the battery voltage can be considered constant. When the charger
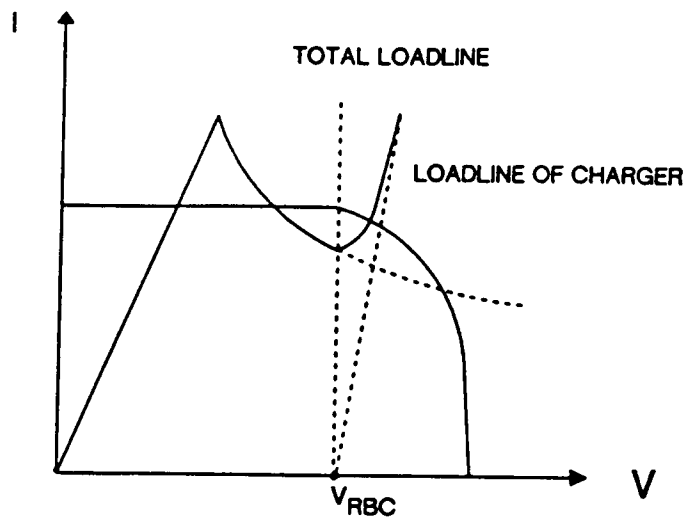
Fig. 3.9 I-V curves of solar array source and load (B/C + constant-power load) in charger's bus voltage regulating mode
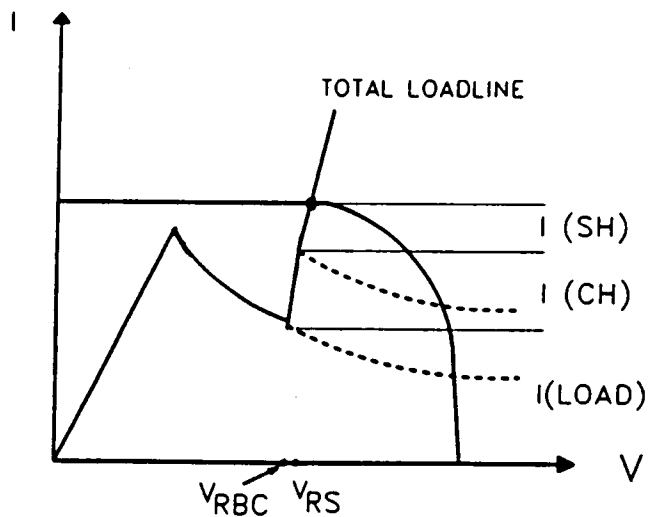

Fig. 3.10 I-V curves of solar array source and load (B/C + shunt + constant-power load) in charger's charging current regulating mode

stays in the charging current regulating mode, the bus voltage is not regulated by the charger. The bus voltage then rises due to the excess solar array power and the system settles in the shunt mode.

The load lines of the battery charger and shunt regulator, together with a solar array source and a constant-power load, are shown in Fig. 3.10. The charger behaves as an additional constant-power load to the solar array source. The characteristic of the shunt regulator determines the operating point of the system. As a result, the stability of the system depends on r_{sh} of the shunt regulator in this mode.

3.3.3 Dynamic Behavior of the System in the Battery-Discharge Mode

Figure 3.11 can be used to illustrate the system in the battery-discharge mode of operation. The output impedance of the battery discharger is also treated as a simple resistance, r_{BD}. In this case, the battery-discharge current, $i_B(= v_C/r_{BD})$, is added to the source current. Therefore, Eq. (3.12) becomes

$$\frac{dv_C}{dt} = \frac{1}{C} (i_L + i_B - i_R) = \frac{1}{C} (i_L + \frac{v_C}{r_{BD}} - f(v_C)) \qquad (3.17)$$

where r_{BD} is the incremental resistance of of the battery discharger's output. Following the same procedure as in the shunt mode derivations, the eigenvalues are expressed the same as in Eq. (3.15), where

$$\frac{1}{r_E} = \frac{1}{r_L} - \frac{1}{r_{BD}}$$
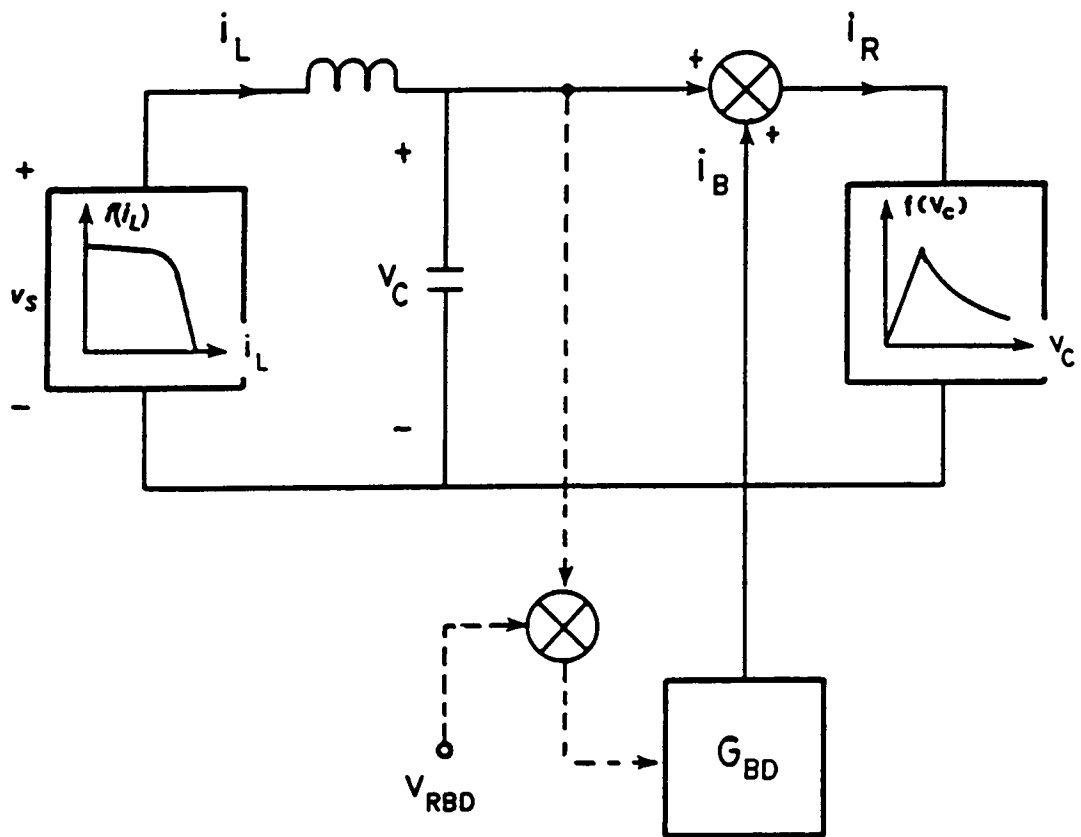
Fig. 3.11 Simplified block diagram of the system in Fig. 3.2 with
the battery-discharger ($G_{BD} = 1/r_{BD}$)

Since r_{BD} is a very small negative value, r_E becomes a very small positive value. Therefore, the additional term $\frac{1}{r_{BD}}$ stabilizes the system.

This analysis can also be explained using the same method as in the shunt mode. As shown in Fig. 3.12, the output characteristics of the battery are added to the constant-power load line to obtain the total load line below the bus voltage, V_{RBD}, where the battery discharger is turned on. The slope of the resulting load line becomes $\frac{1}{r_E}$.

As an another approach, the solar array and the battery discharger are considered as two separate sources connected in parallel. Since the output impedance of discharger is designed to be very small, the total source impedance is almost the same as the discharger's output impedance below V_{RBD}, as shown in Fig. 3.13. This condition can be viewed as the system is operating with a stiff voltage source.

The condition of the system's stability in this mode is also $(\frac{r_S}{L} - \frac{1}{r_E C}) < 0$.

3.3.4 Dynamic Behavior of the System in Deadband Mode

The deadband mode represents a period when the solar array solely supplies the power to the load, so that any power conditioning equipment, such as the shunt regulator, battery charger and discharger, is not activated.

Since none of the power conditioning equipment is activated during the deadband mode, the system's dynamic is the same as the case shown in Fig. 3.2. The equilibrium points between Point A and Point B in Fig. 3.14 are not stable, as described in Section 3.2. Therefore, the system
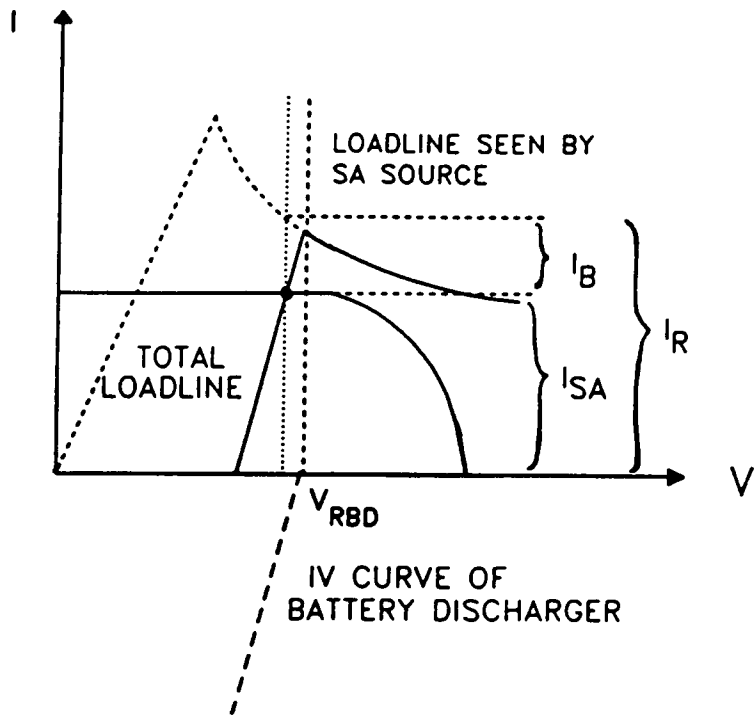
Fig. 3.12 I-V curves of solar array source and load (B/D +
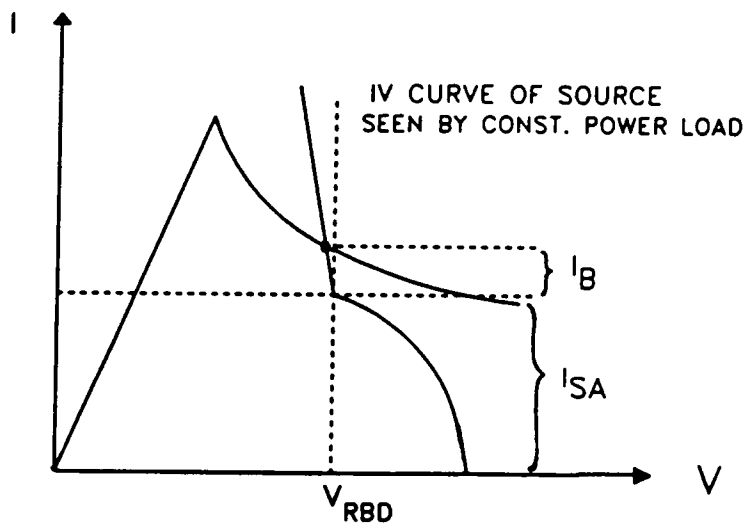   constant power load) in battery-discharge mode

Fig. 3.13 I-V curves of source (solar array + B/D) and
          constant power load in battery-discharge mode

with a constant-power load never stays in the deadband mode; that is, the operating point between Points A and B moves to either Point D or Point E, depending on the initial condition and location of the separatrix of the system.

Let us consider a case when the system enters the deadband mode during a transition from sunlight to eclipse. Figure 3.14 shows two solar array curves. Curve S1 is the I-V characteristic of the array at full-sun illumination level and Curve S2 represents its characteristic at low illumination. During a full-sun period, the system was in the shunt mode and the solar array's operating point was at Point A. As the illumination level goes down, the curve S1 moves down and meets the load line, L1, at Point E. Then, the shunt regulator is deactivated. When the solar array curve moves down further, below S2, the separatrix of the system occurs on the right-hand side of the previous operating Point, E, which is the initial condition for the system. Therefore, the operating point of the solar array moves toward Point F until the output voltage of the solar array reaches V_{RBD} at Point C, where the battery discharger is turned on and the operating point of the system eventually moves to Point D.

The results of simulation for the case described above are shown in Fig. 3.15. In this simulation, the actual circuit models of the shunt regulator and the battery discharger, including the feedback circuits, are used instead of dc models. At the beginning of simulation, the system is in the shunt mode with a shunt current of 1.5 ampere. The illumination level begins to decrease linearly at 1 msec, to simulate the transition from the sunlight to eclipse. The shunt current decreases accordingly, and becomes
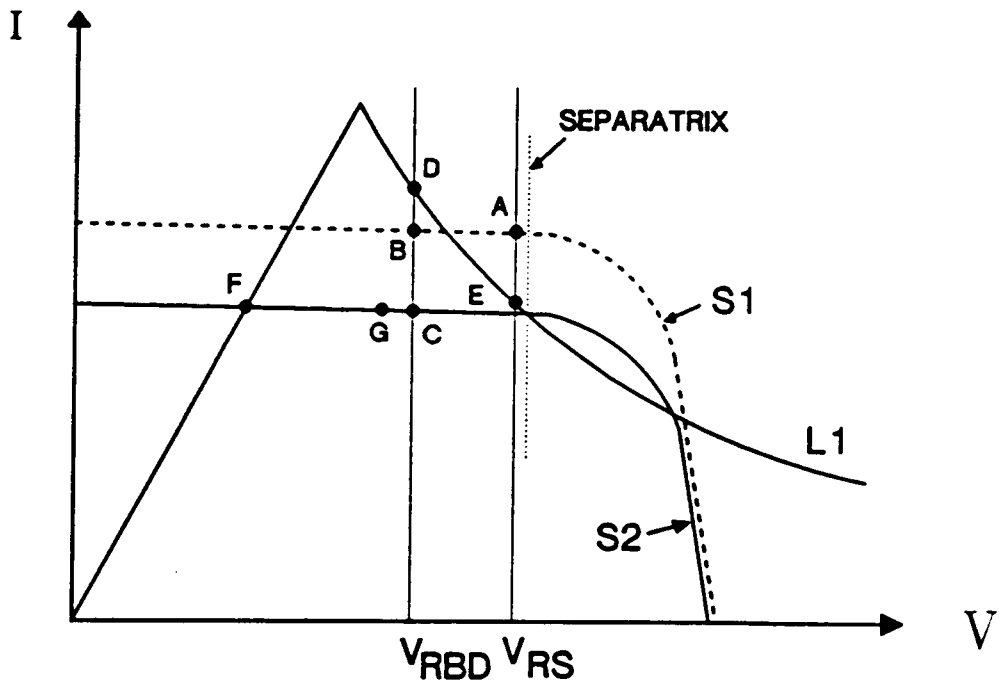
Fig. 3.14 I-V curves of solar array and constant-power load for deadband mode
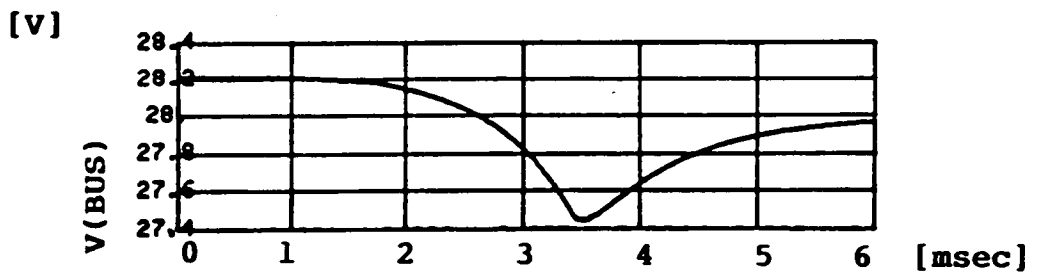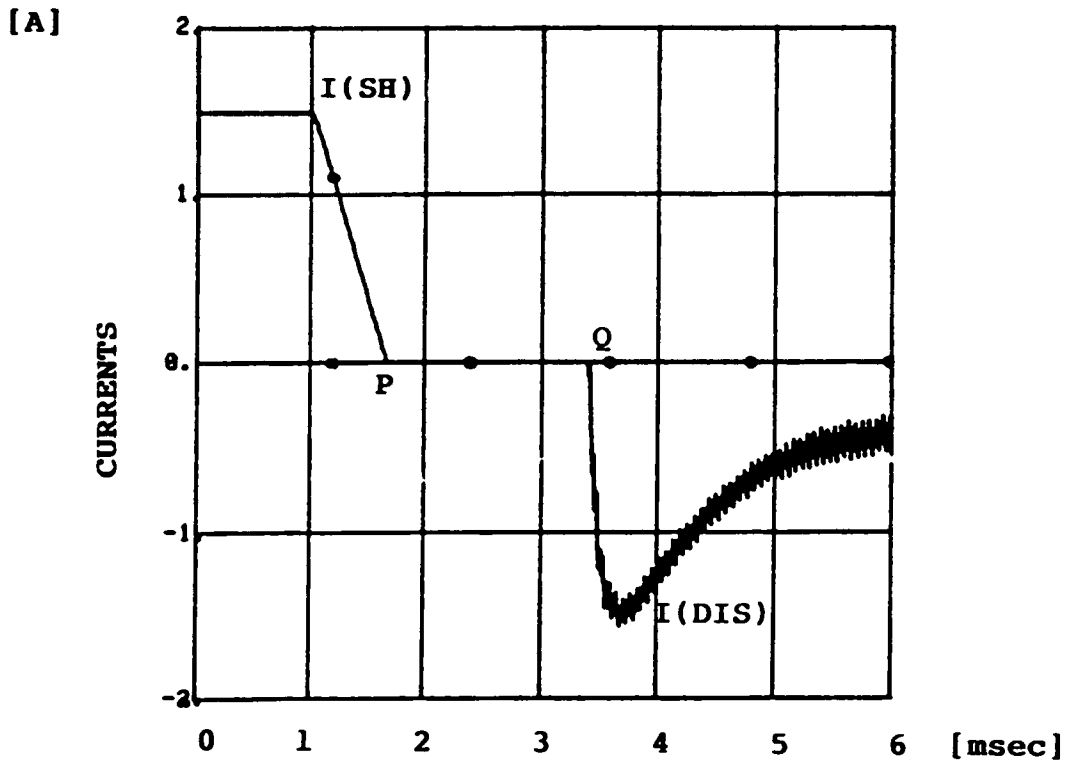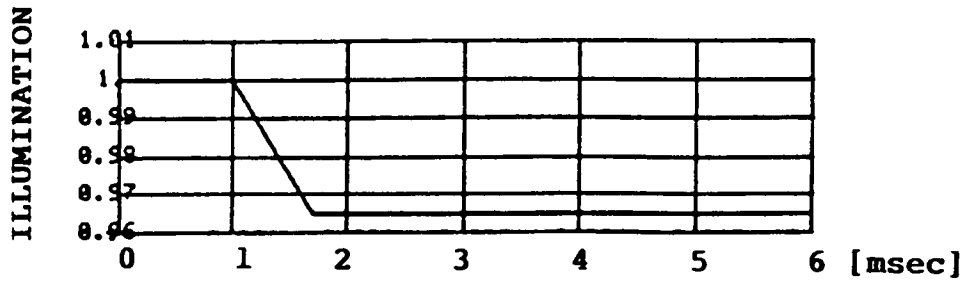
Fig. 3.15 Simulation of deadband mode

73

zero at Point P. From Point P to Point Q, neither the shunt regulator nor the battery discharger is activated. This period is in the deadband mode. During this period, the solar array operating point in Fig. 3.16a moves from Point E to Point G and back to C. The system operating point then moves from E to D, as shown in Fig. 3.16b. In the figure, the trajectories pass over and return back to the steady state operating point. This is because the battery-discharger's turn-on delay causes the bus voltage to drop below its regulation voltage and the discharger current has an overshoot at turn-on time.

From the state trajectory, one can observe that the equilibrium point in the battery-discharge mode is a stable node. The values of L and C used in this simulation are 1 μH and 1000 μF, respectively.

3.3.5 Dynamic Behavior of the Semi-regulated Bus System

The only difference between the regulated-bus and the semi-regulated bus systems is that there is no battery discharger in the semi-regulated bus system. In the semi-regulated bus system, the battery discharges through a diode instead of a battery discharger. Therefore, all the bus dynamics described for various modes, except the battery-discharge mode, are also applied to this system.

Consequently, there is no regulation during the battery-discharge mode and the bus voltage varies according to the terminal voltage of the battery. Since the battery voltage varies according to the battery's state-of-charge, the bus voltage varies in a wide range, depending on the battery voltage.
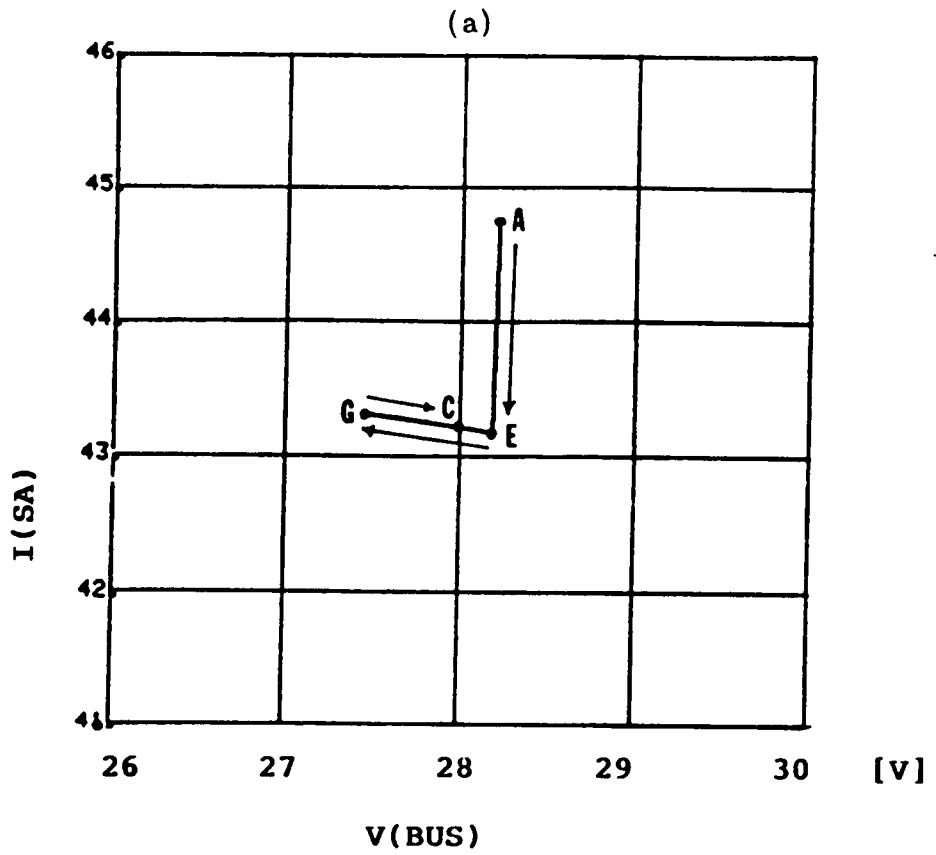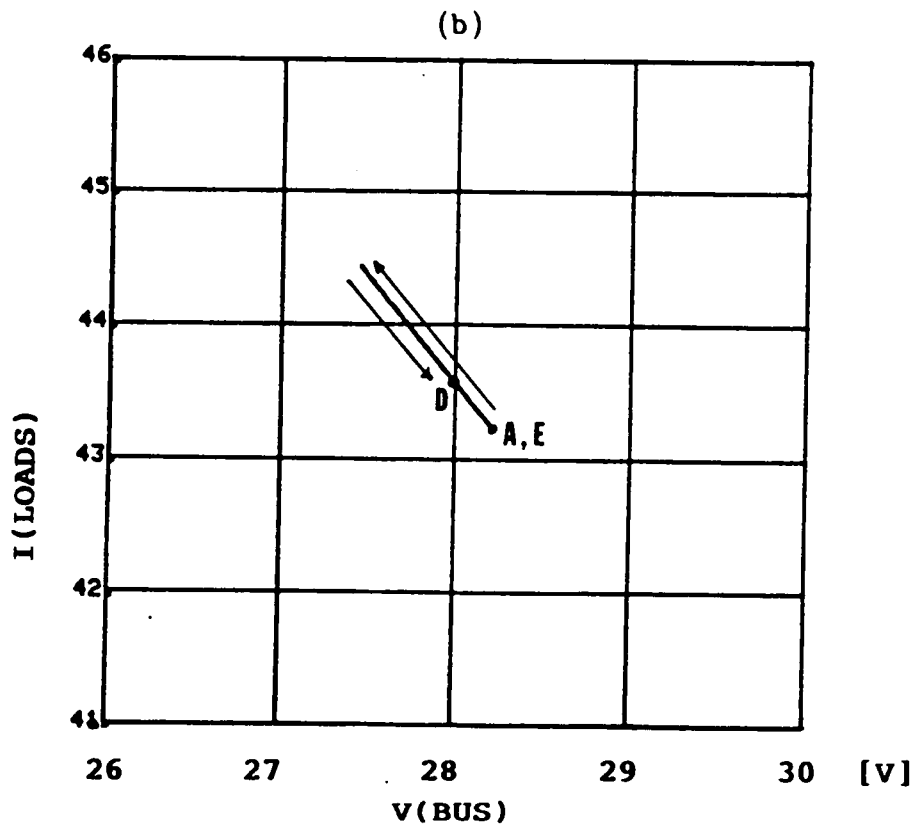
Fig. 3.16 Trajectory simulation of deadband mode

Since the output resistance of the battery is very small, the system bus becomes a stiff voltage source, as in the battery-discharge mode in the regulated-bus system, except for a varying output voltage. The resulting I-V curves in the battery-discharge mode are shown in Fig. 3.17. In the figure, the battery is considered as a source paralleled with a solar array. When the battery voltage is V_{BA1}, the operating point of the system is F and when the battery voltage is V_{BA2}, the operating point is A. Therefore, the bus voltage varies according to the battery voltage.

3.4 Analysis of Solar Array/Battery Lockup

The solar array/battery lockup has long been considered in the design of spacecraft power systems. The lockup is a phenomenon in which the battery shares the load power, although the solar array alone can supply the load power at the moment. To avoid the lockup, the solar array is usually oversized in many applications.

In this section, the lockup problem is analyzed in detail, using the results from the large-signal analysis described in the previous sections. This analyses will be verified through computer simulations.

First, a spacecraft power system composed of a solar array, a shunt regulator and a battery (or a battery with a battery discharger) is considered. During a sunlight period, the longest period in one orbit-cycle of the spacecraft, the solar array produces enough power to supply the spacecraft loads and to recharge the batteries. Since the solar array's power capability is normally designed to exceed the load demand, the shunt
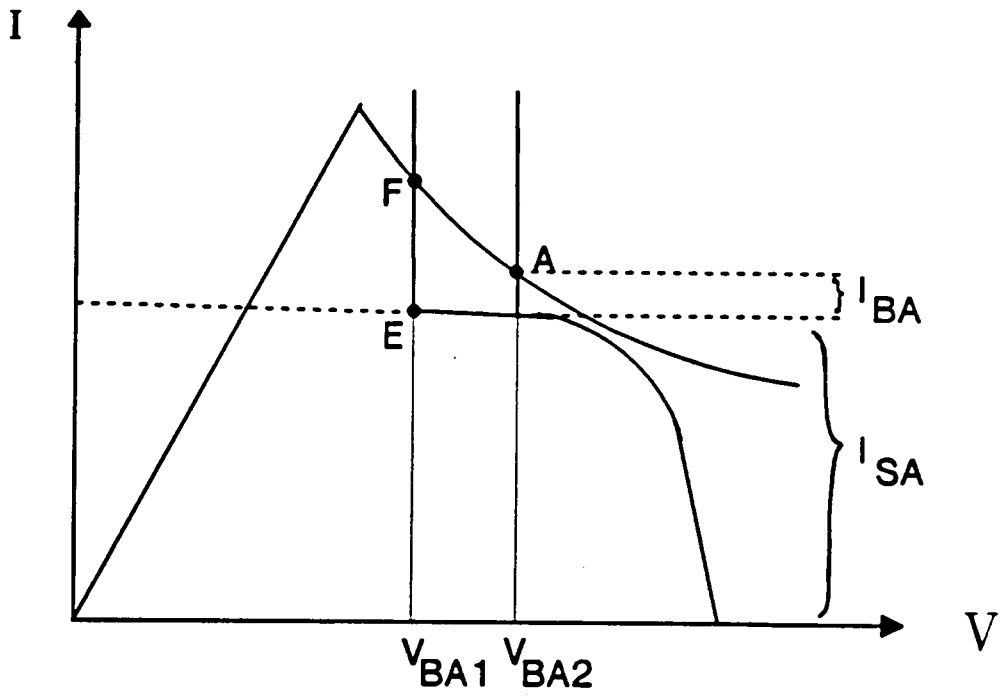
I

F

A .... } I_{BA}

E ....

I_{SA}

V

V_{BA1} V_{BA2}

Fig. 3.17 I-V curves of solar array, battery and constant-power
load in battery-discharge mode

regulator is active, limiting the array voltage during most of the sunlight period. However, during periods of launch, eclipse, or when the peak power demand is in excess of solar array capability, the batteries should supply all or part of the load, as required.

The lockup situation can be explained using Fig. 3.18. V_{RBD} in the figure represents a reference voltage of the battery discharger in the regulated-bus system or a battery voltage in the semi-regulated bus system. For example, with a load of 1250 W, the operating point of the solar array can reside on either Point B or Point C, depending on the previous operating condition. Point A is not a stable operating point.

Let us assume that the operating point was on Point C instead of Point B. Since, at Point C, the load power demand is less than the solar array power, the shunt regulator is taking part of the solar array current. When the load demand is increased to 1270 W, the operating point moves to Point D, because the solar array cannot supply the new load demand.

Suppose that the load power is again decreased to the original value, 1250 W. The operating point then moves from Point D to Point B. Point B is a stable operating point, because the battery discharger is a stiff voltage source as shown in Section 3.3.3. Therefore, although the source has enough power to supply the load, the system stays on the battery-discharging mode. From Fig. 3.18, it can be seen that, if the difference between the shunt reference voltage, V_{RS}, and the battery discharger's reference voltage, V_{RBD}, is large, the battery-discharge current at lockup can be large.
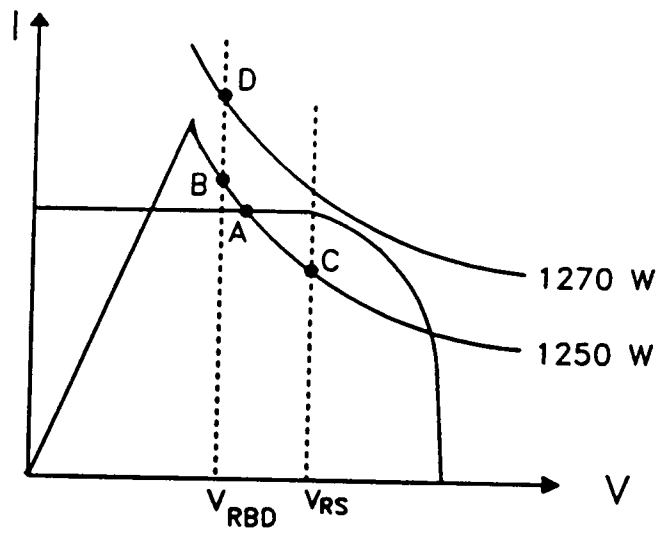
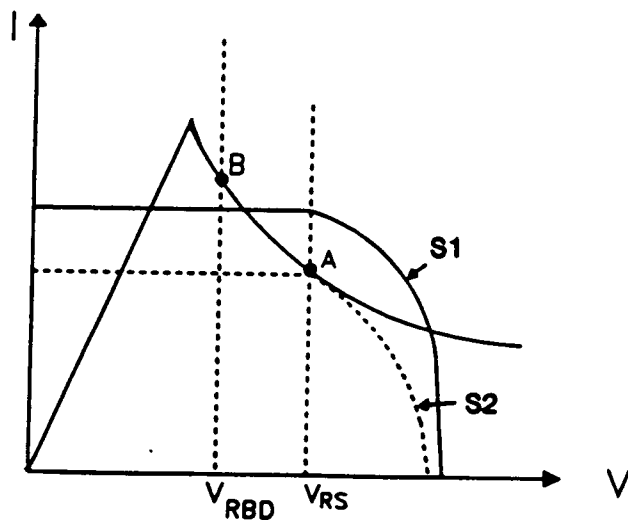Fig. 3.18   Solar array/battery lockup due to load change

Fig. 3.19   Solar array/battery lockup due to illumination change

79

This lockup can occur both in regulated bus and semi-regulated bus systems. However, since $|V_{RS} - V_{RBD}|$ is very small in the regulated-bus system (that is, the bus is tightly regulated in most regulated systems), the lockup current is small. In the semi-regulated bus system, the bus voltage varies according to the battery terminal voltage. Since the battery voltage becomes low when the state-of-charge is low, the bus voltage can be low. As a result, the battery lockup current can be large (e.g., from Point E to Point F as shown in Fig. 3.17).

The battery lockup can also occur with a fixed load when the source power varies. As shown in Fig. 3.19, let us assume that the I-V curve of the solar array is Curve S1 and the operating point is on Point A in the shunt mode. When the illumination level becomes low or the solar array is shaded for some reason, the I-V curve of the solar array can be lower than Curve S2. The operating point then moves to Point B, which is in the battery-discharge mode. If the solar array resumes its original power level, Curve S1, the operating point still remains at Point B. This is another case of battery lockup.

Battery lockup is not serious if it does not last long. That is, battery lockup can be allowed during a transient period, such as an eclipse to sunlight.

To avoid this lockup problem, the startup surge current of any load converter connected to the bus should be designed with a current level lower than the shunt current, because the solar array sees the surge current as a temporary increase of the constant-power load, as shown in Fig. 3.18. Another way to avoid the problem is to design the size of the solar array

to be sufficiently large so that the system can have only one stable operating point in the shunt mode with a full-load condition, as shown in Fig. 3.20. Curve S3 represents the I-V characteristic of the source with the shunt regulator and battery discharger (or battery). This source line consists of three characteristics: dc output characteristics of the solar array, battery discharger and shunt regulator. That is, below V_{RBD} the output impedance of the battery discharger dominates the source characteristics, while the shunt regulator's output impedance dominates the source characteristics above V_{RS}.

To escape from the lockup condition, the system should be forced to have only one stable operating point on the output characteristic line of the shunt. From Fig. 3.21, let us assume that the operating point of the system stays at Point A, which is a lockup condition. One way to obtain a single stable operating point is to move the load line from Curve L1 to the dotted Curve L2 by temporarily reducing the load power. Since there is only one intersection at Point C (a stable point) between the source curve, S3, and the constant-power curve, L2, the previous operating Point A moves to C. The operating point will then stay at Point B after resuming the original load power.

Another way is to avoid the battery lockup is to move the solar array source line from Curve S2 (Fig. 3.22) to S1 by slightly tilting the solar array panel toward the sun. It then gives a new combined source curve, S3. This new source curve with the constant-power load line can have only one stable operating point at B, which is in the shunt mode.
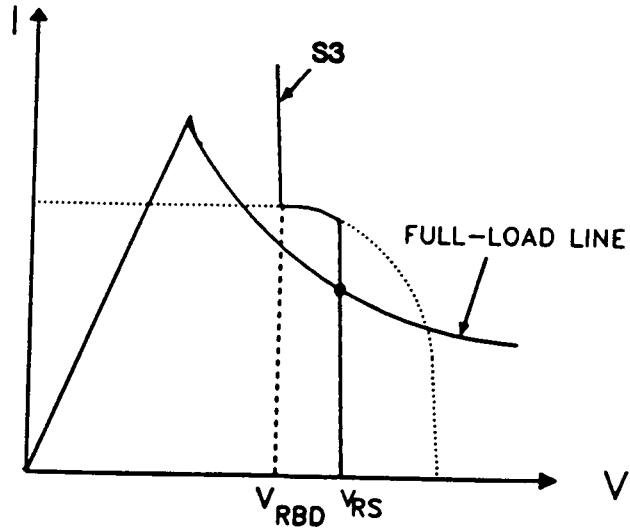
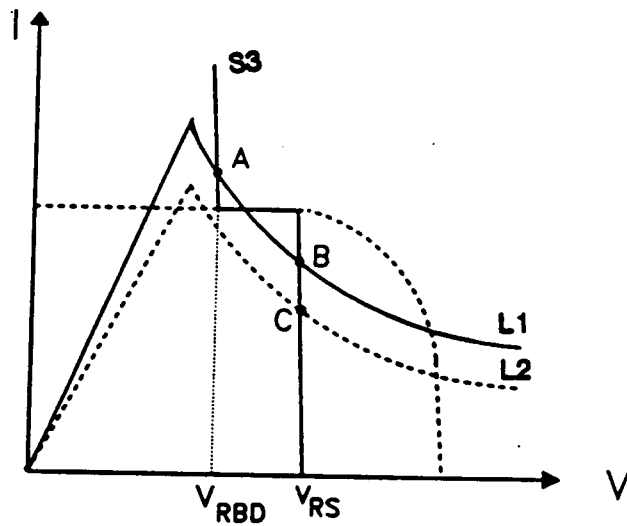Fig. 3.20 Source line and full load line without battery
lockup

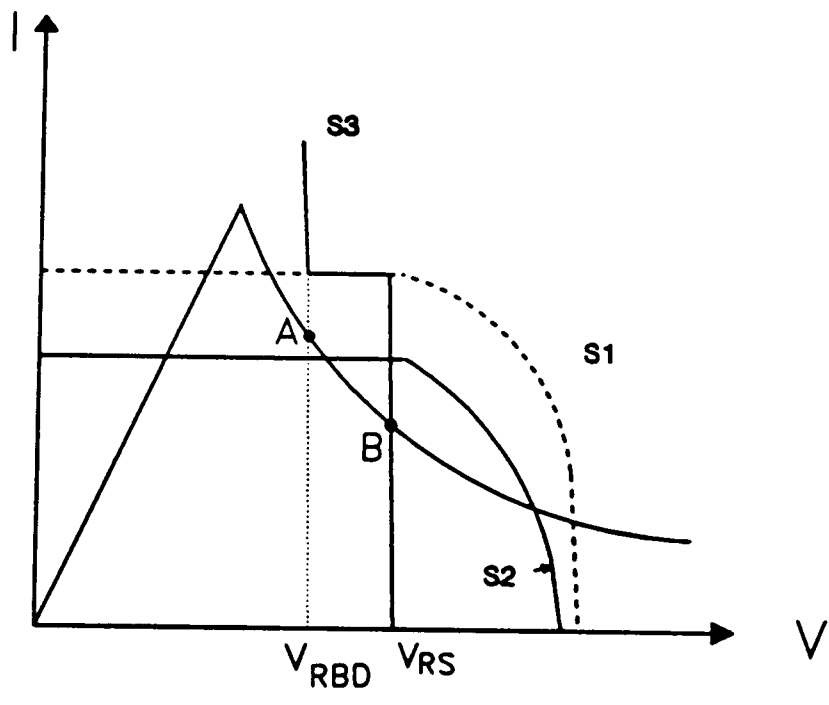Fig. 3.21 Escaping method from battery lockup by changing
load power

Fig. 3.22 Escaping method from battery lockup by changing illumination level

83

Figure 3.23 shows a simulation result, in which the system goes into a battery lockup condition by temporarily increasing the load power. At the beginning of simulation, the system operates in a shunt mode. The load power is 1250 W and the shunt current is 0.4 A. At 2 msec, the load is increased to 1270 W abruptly. As graphically illustrated in Fig. 3.18, the operating point moves to Point D in the battery-discharge mode. After the load power returns to 1250 W at 10 msec, the system stays in the battery-discharge mode with a smaller discharging current than before.

Figure 3.24 shows a simulation result in which the system comes out of the previous battery lockup condition by temporarily reducing the load power. At the beginning of the simulation, the system is in the battery-discharge mode, with the load power of 1250 W. At 2 msec, the load is step-changed to 1230 W. The system then goes to the shunt mode and stays there after the load power returns to 1250 W at 4 msec.
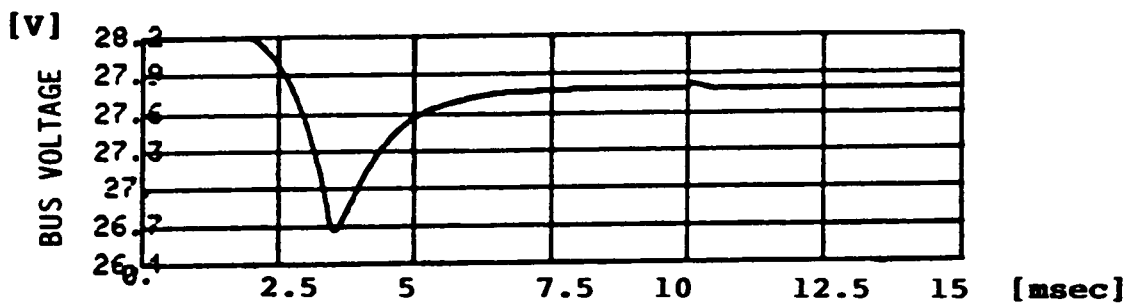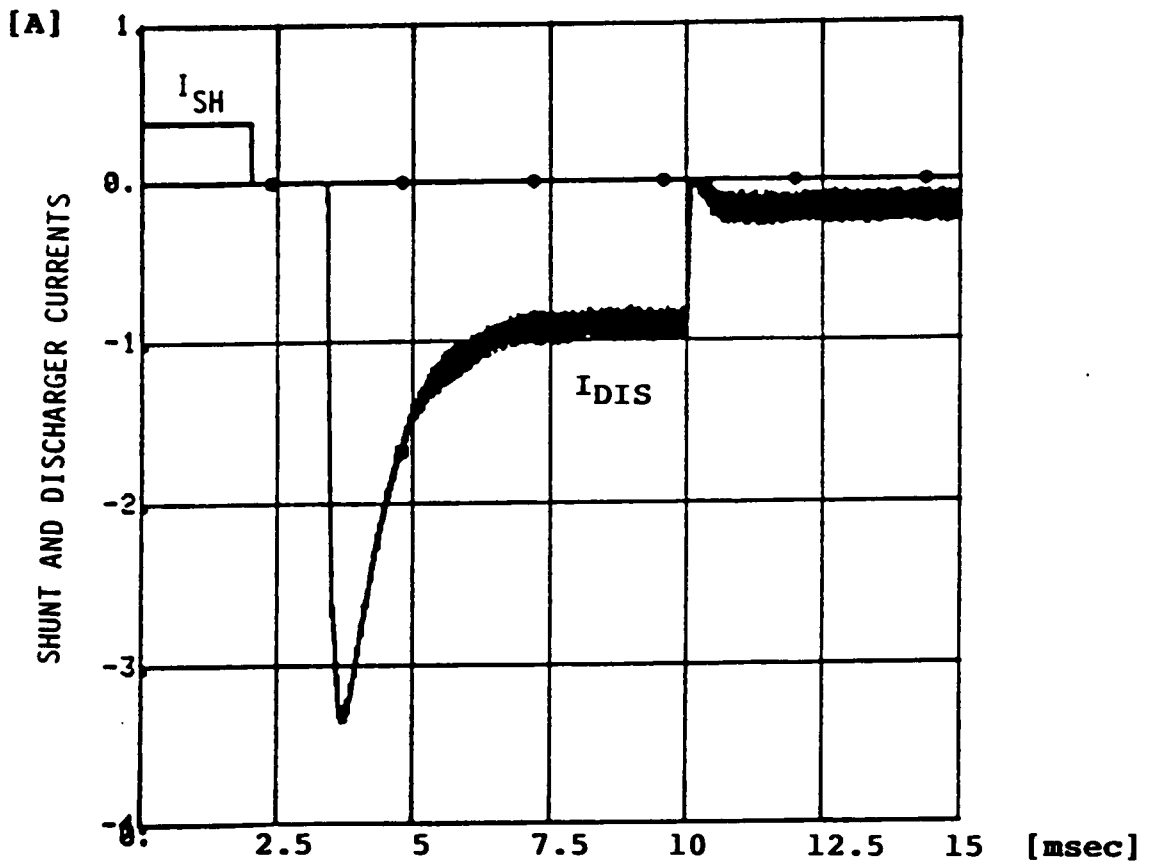
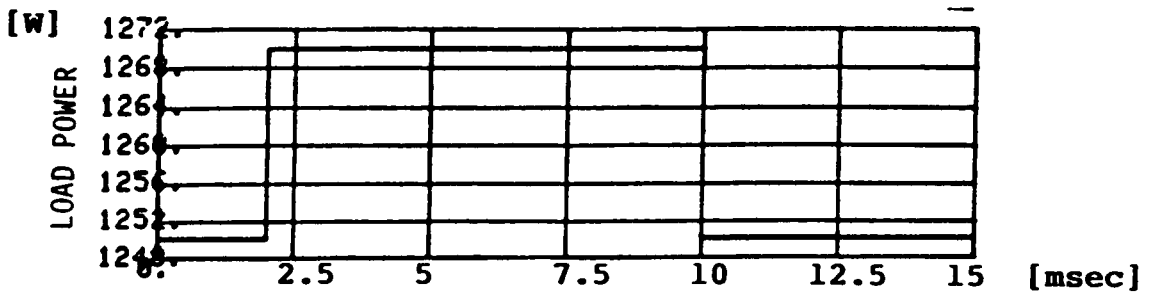These simulation results agree well with the previous analysis.

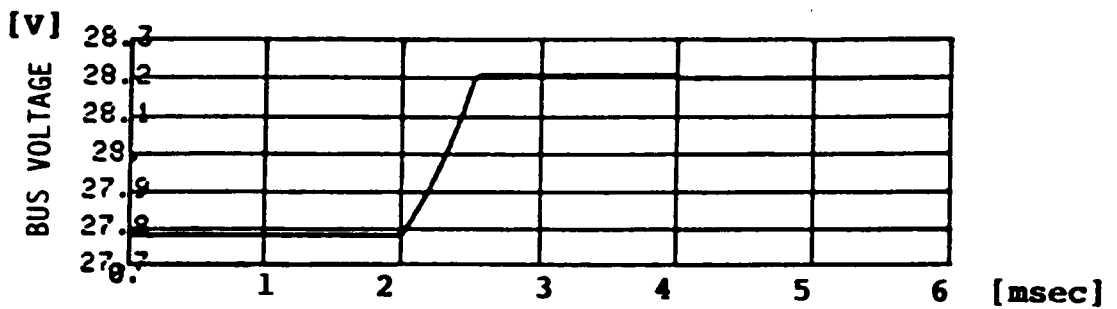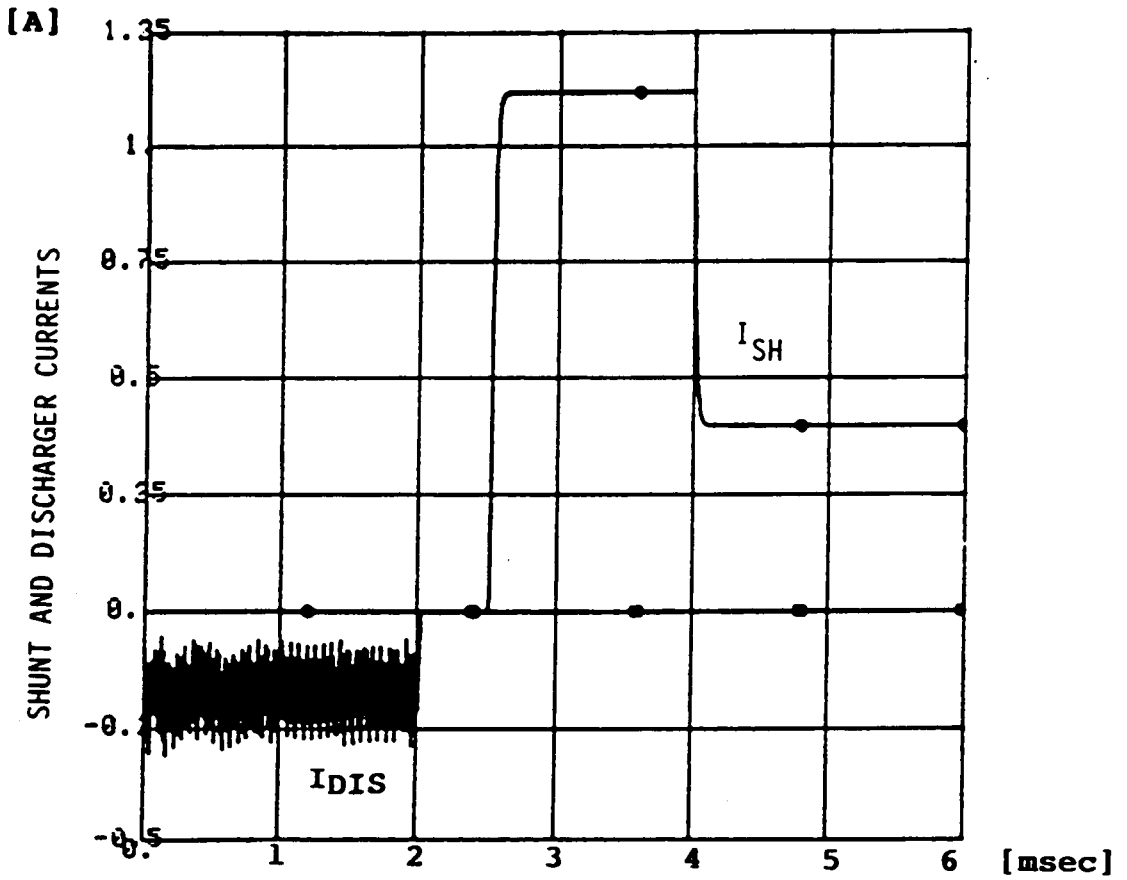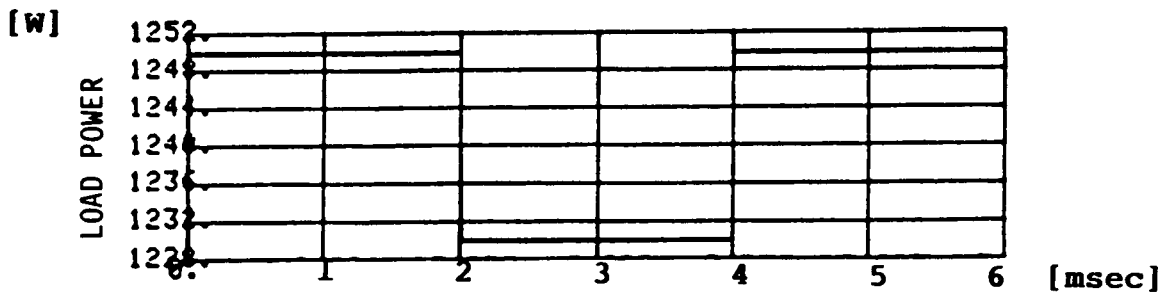Fig. 3.23   Simulation of battery lockup situation

Fig. 3.24   Simulation of escaping from lockup by changing load power

86

3.5 Analysis of Failure Mode

The bus voltage of the DET system is mainly regulated by the shunt regulator and battery discharger. Since spacecraft power systems require high reliability, they are usually designed with a redundancy concept. Two different types of redundancy concepts are used to avoid system failure due to failure of a piece of equipment. One type is implemented with standby equipment, an extra piece of equipment which automatically takes over the function of failed equipment, activated by a switchover signal from a fault detector. The other one is called 'on line redundant.' In this case, parallel modules share current during normal operation, with one module taking over the whole current if the other one fails. In order to properly design failure protection circuits and/or redundant equipment, it is important to predict bus behavior when each piece of equipment fails.

In this section, two major failure cases, shunt failure and battery discharger failure, are analyzed using the large-signal analysis technique. Redundancies are not implemented for this study, however, since the objective is to understand the system's behavior after the failures so that an optimum strategy of failure control, using the forementioned redundancy concept, can be implemented.

3.5.1 Shunt Regulator Failure Mode

During the sunlight period, the shunt regulator is activated to limit the bus voltage. When the shunt regulator fails, i.e., the power devices in the circuit fail, the bus voltage rises to Point B in Fig. 3.25. The increase
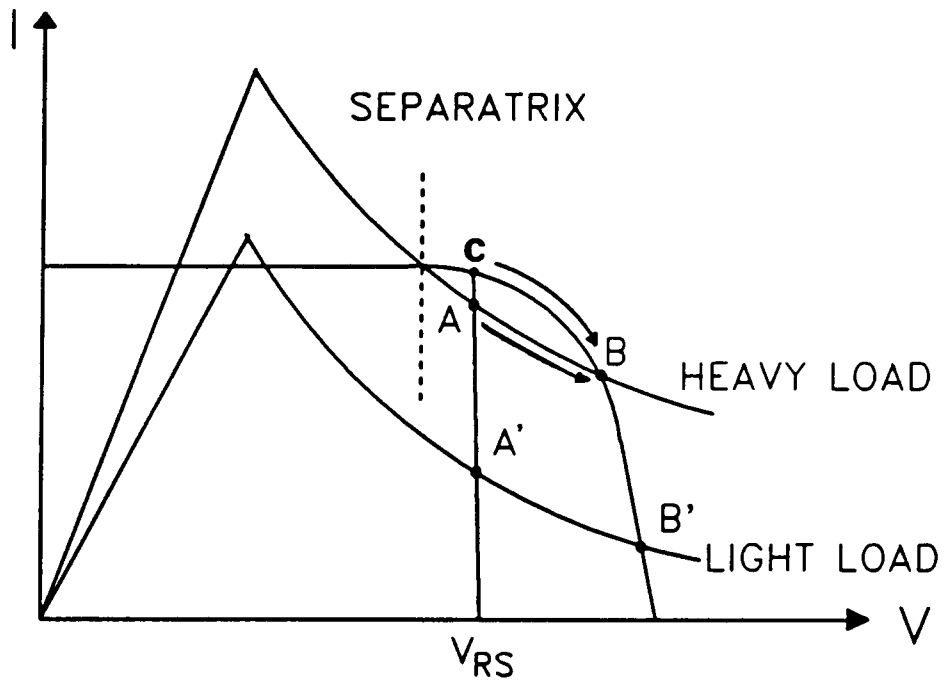
Fig. 3.25 I-V curves of solar array source and constant-power loads

of the bus voltage triggers a redundant shunt regulator through a fault detector.

The shunt failure mode is graphically analyzed using the I-V curves, as shown in Fig. 3.25. In this analysis, the shunt is assumed to be completely inactivated, that is, no shunt current flows, at the moment of a failure. If the operating point on the solar array I-V curve is at Point C before the failure, the operating point moves toward Point B after the failure. In case of a heavy load, the solar array's operating point will move from Point C to Point B, and in the case of a heavy load, from Point C to Point B'. Therefore, the bus voltage rises higher in the case of the light load. During the transient, the difference between the solar array current and the load current will charge up the filter capacitor of the bus. The bus voltage will rise at a much faster rate in the light-load case.

These analyses are verified through simulations. A computer model, consisting of a solar array, a shunt regulator, a battery discharger and a constant-power load, is configured to simulate the shunt failure and battery-discharger failure modes.

Figure 3.26 shows simulation results of the shunt failure. At the beginning of the simulation, the system is in the shunt mode, with a shunt current of 0.4 A. At 1 msec, the shunt regulator fails and the shunt current becomes zero. The solar array current and load current follow the trajectories as shown in Fig. 3.25. The operating point on the solar array I-V curve then moves from the left to the right, as shown in Fig.
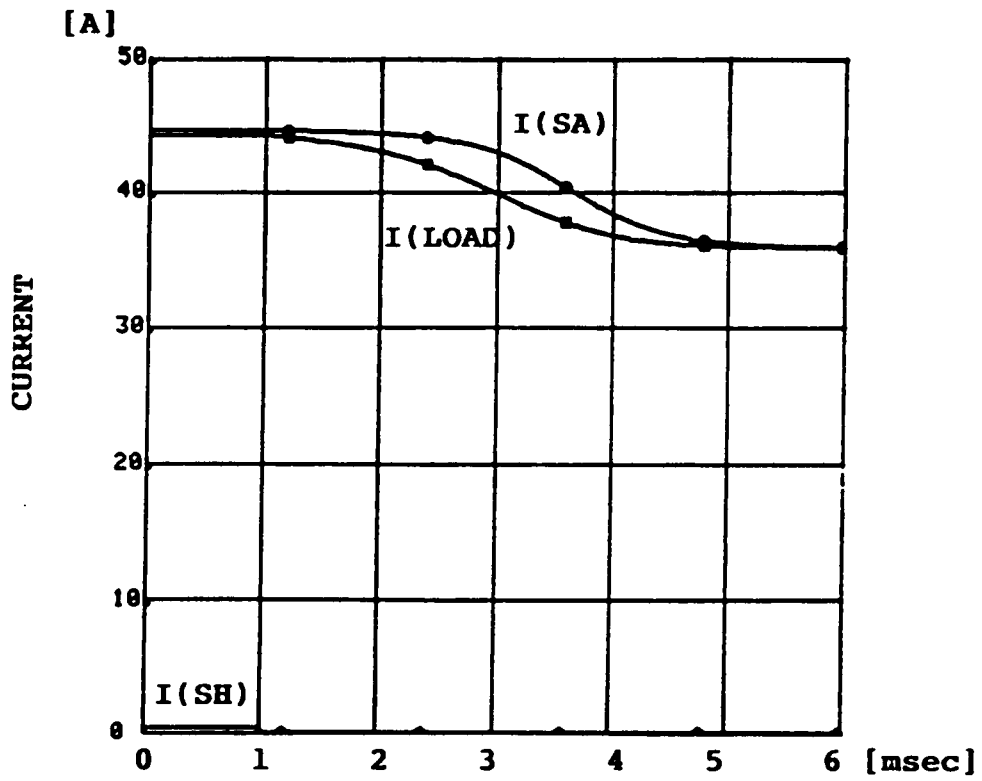
Fig. 3.26   Simulation of shunt failure mode
(heavy load case)

3.27a. An increase of the bus voltage and a decrease of the solar array current are shown in Figs. 3.27b and 3.27c, respectively.

Figure 3.28 shows simulation results of the shunt failure in the case of a light load. As shown in Fig. 3.29, the bus voltage rises at a faster rate, as expected. Since the switch-on of a standby shunt regulator is with a certain time delay, the worst case bus voltage overshoot occurs under the light load condition.

3.5.2 Battery Discharger Failure Mode

During eclipse periods, the battery discharger is activated to supply the load power. When the battery discharger fails, the bus voltage will fall. It is assumed that the discharger is completely disabled during failure.

The parallel modules of the battery discharger are usually used to provide on-line redundancy to the system. Transient response of the on-line redundant system is obviously much better than that of the standby system, because there is no time delay for switchover to the other equipment.

In this section, the discharger failure mode is analyzed to examine the bus voltage and current transient response. As shown in Fig. 3.30, since the source characteristic of the battery discharger disappears and the original source characteristic of the solar array below V_{RBD} is resumed at the moment of the failure, there exists only one equilibrium point, P_{e1}. Therefore, the state trajectories of the solar array and the load will follow the curves shown in the figure.

[A]

S.A Current

BUS VOLTAGE

(a)

[V]

Bus Voltage

(b)

[A]
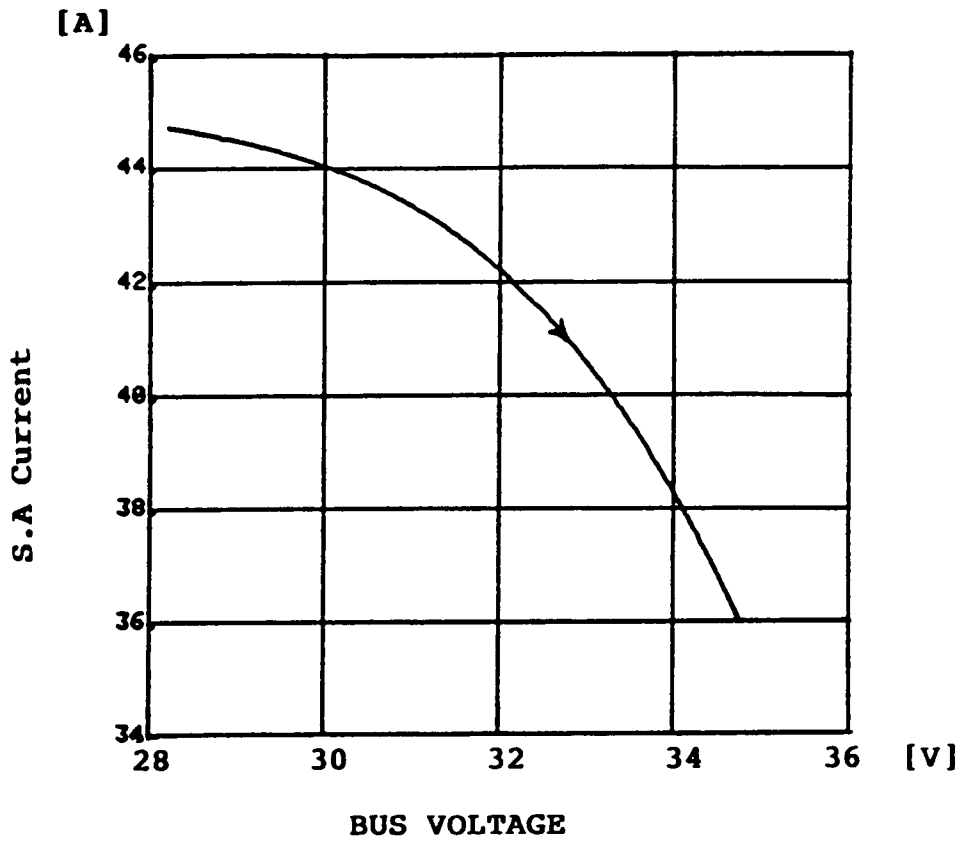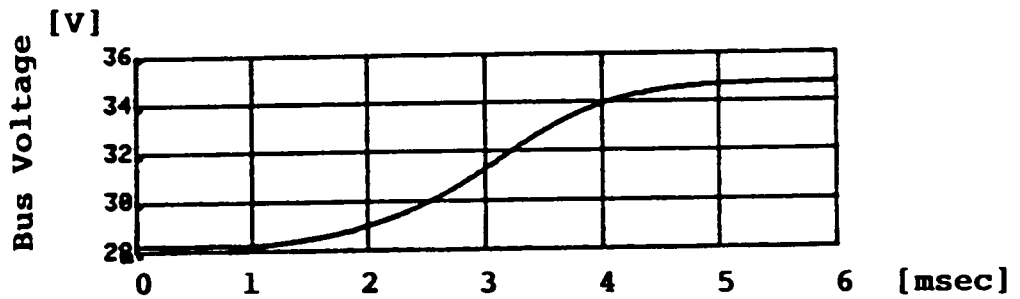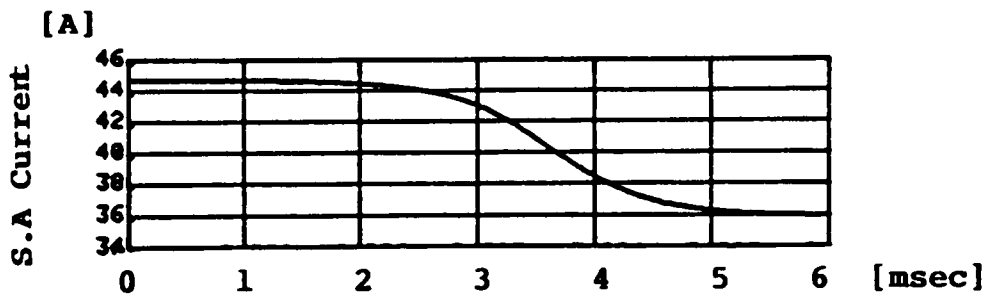
S.A Current

(c)

Fig. 3.27   Simulation of shunt failure mode
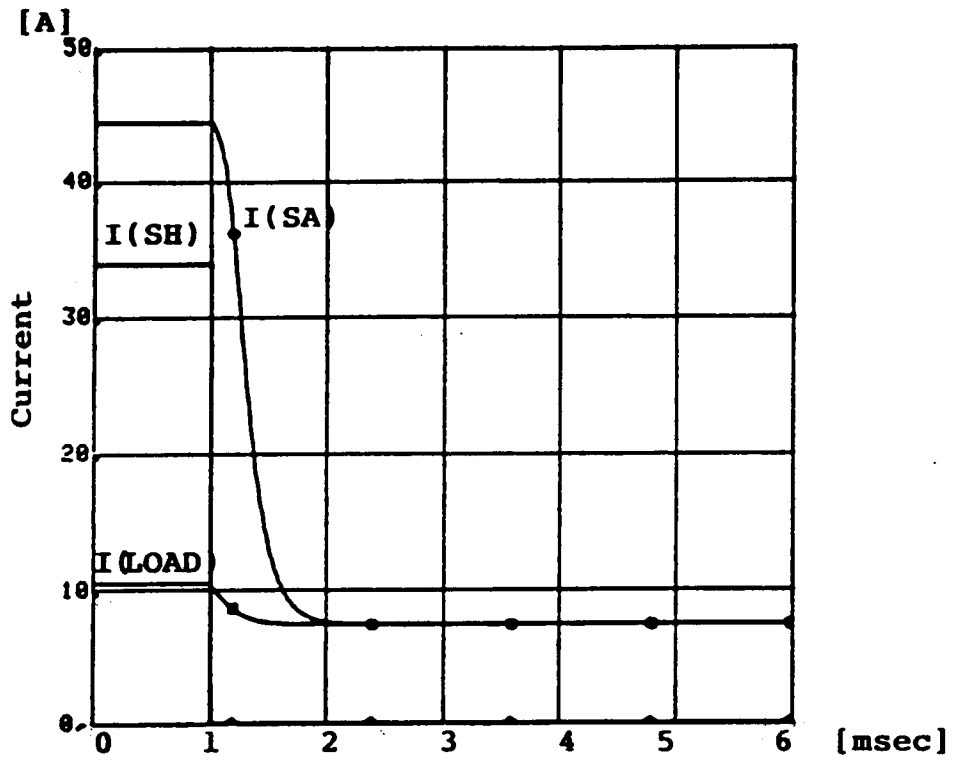(heavy load case)

Fig. 3.28   Simulation of shunt failure mode
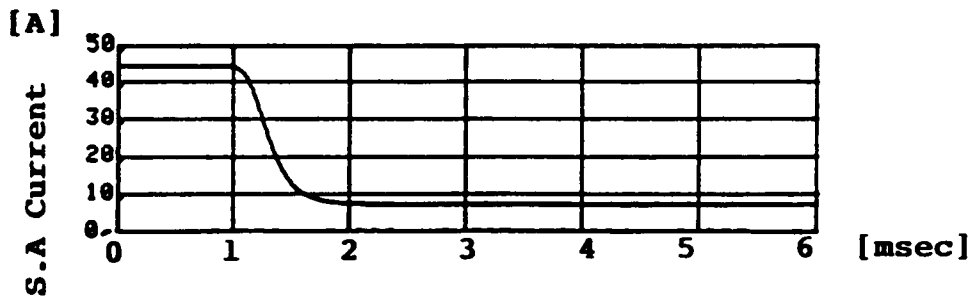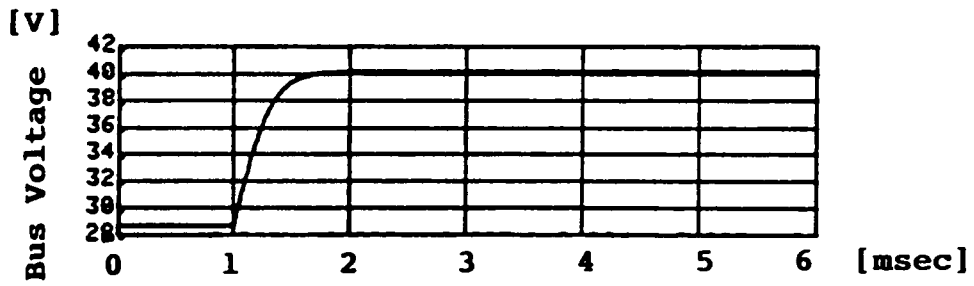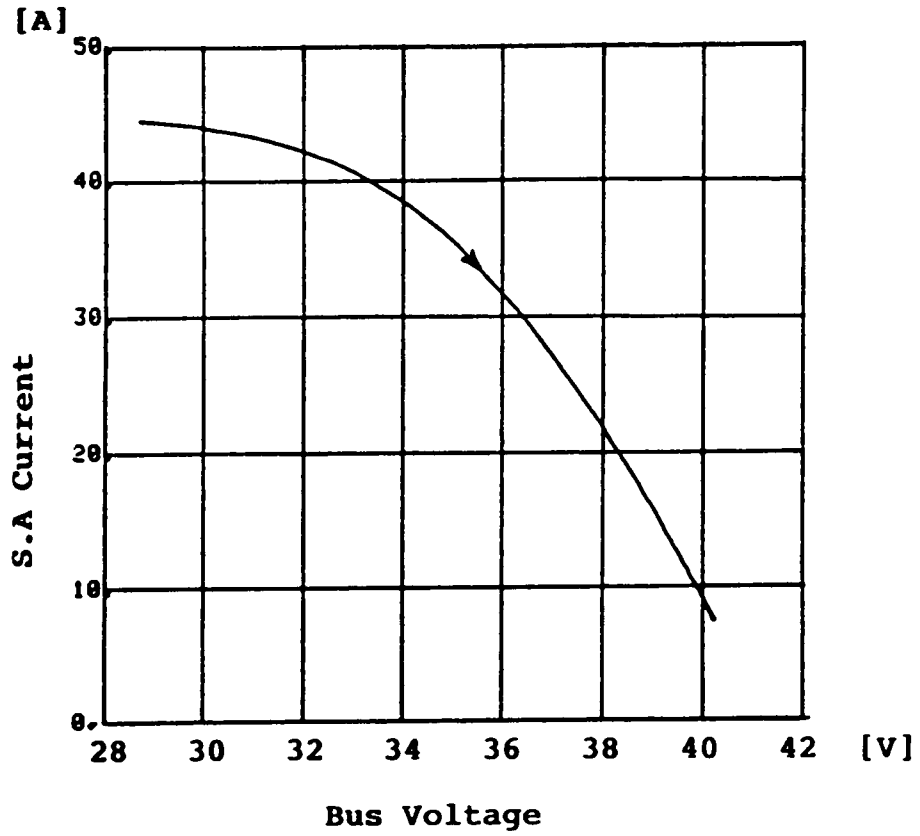(light load case)

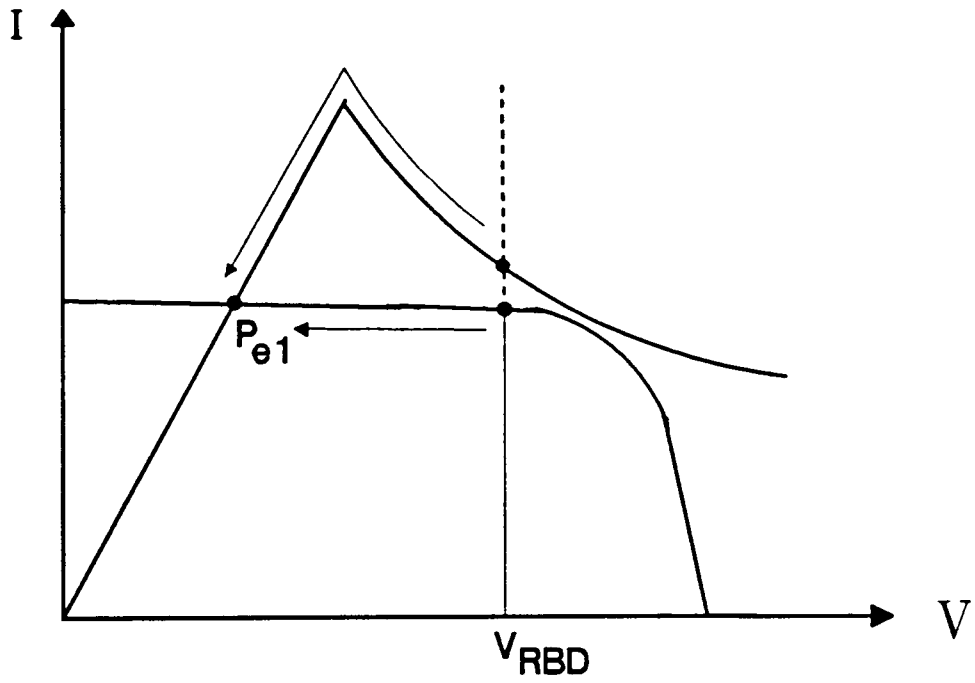Fig. 3.29   Simulation of shunt failure mode
(light load case)

Fig. 3.30 Trajectories of the voltage and current of the solar array
and load after battery-discharger failure

Figure 3.31 illustrates the transient response after the discharger fails. At the beginning of simulation, the system is operated in the battery-discharge mode, with a small discharging current. At 1 msec, the discharger fails, e.g., the output diode fails in the boost converter. Since the load power demand is larger than the solar array power, only one equilibrium point exists.

The simulated trajectory of solar array current and bus voltage are shown in Figs. 3.32a-c, together with their time responses. After the transient period, the bus voltage drops out of the regulation range.
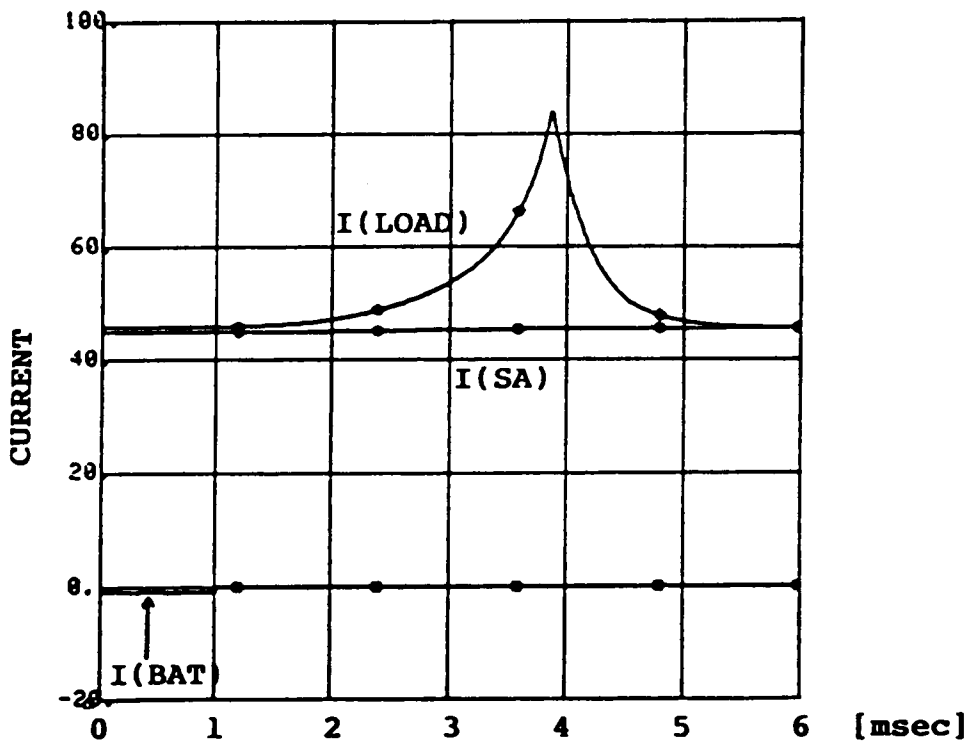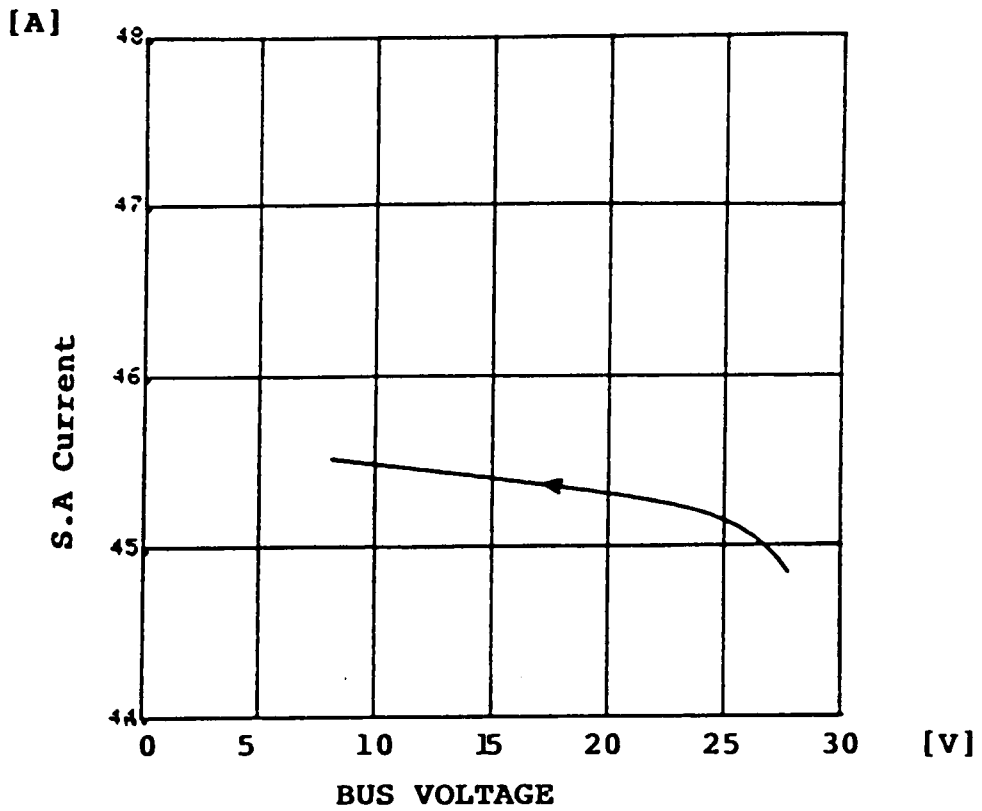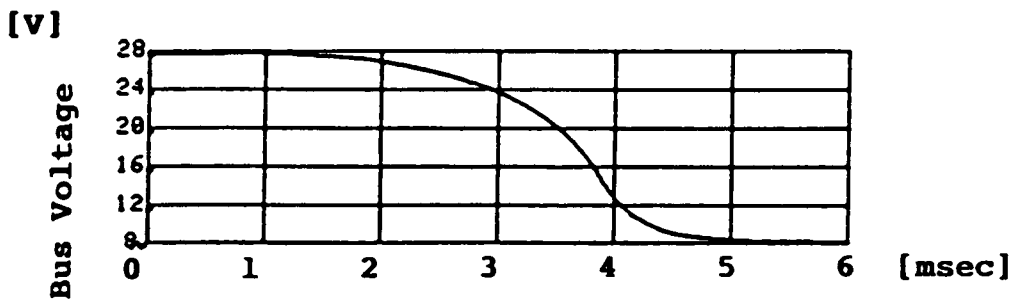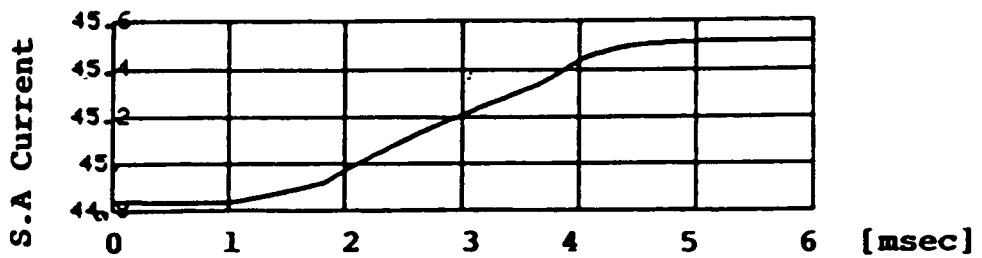
Fig. 3.31 Simulation of battery discharger failure mode

Fig. 3.32   Simulation of battery discharger failure mode

98

3.6   Conclusions

The large-signal state-plane analysis of a typical solar array system with a constant-power load has been reviewed. Three regions, Region #1, Region #2 and Region #3, are identified to cover the entire state plane. The analysis shows that any equilibrium point in Region #2 (the solar array's current source region) is unstable and the equilibrium point in Region #3 (the solar array's voltage source region) is conditionally stable. The equilibrium point in Region #1 is stable but undesirable; it produces low bus voltage. The state trajectories are separated by a separatrix that passes through Region #2. Since the state trajectories always converge to one of the two stable equilibrium points located in Region #1 or #3, the behavior of the system is quite different on either side of the separatrix.

The system can be stabilized in Region #2 when the shunt regulator or the battery discharger is employed. The role of the shunt regulator can be viewed in two different ways; it either makes the source characteristic a stiff source or changes the constant-power load characteristic into a resistive load at the bus voltages above the reference voltage of the shunt regulator, V_{RS} . The role of the battery discharger is the same as for the shunt regulator at the bus voltages below the reference voltage of the discharger, V_{RBD}. Consequently, the source characteristic of the regulated DET system is composed of three components: the battery discharger's dc output characteristics below V_{RBD} , the shunt regulator's dc output characteristic above V_{RS} and the solar array's characteristic between V_{RBD} and V_{RS}.

The solar array/battery lockup phenomenon was analyzed. The battery lockup occurs when a temporary step-up change of load results in a larger power demand than the solar array can provide, or when the solar array output power is temporarily reduced to a level lower than what is required by the load. The system can escape from the lockup by either temporary load-shedding or temporarily tilting the solar array panel toward the sun.

Failure analyses were performed. When the shunt regulator fails, the bus voltage rises. The overshoot of the bus voltage depends on the shunt current level before the failure. When the battery discharger fails during an operation when the solar array alone cannot provide the entire load power, the bus voltage drops to a voltage level where the equilibrium point is located in Region #1.

Since the operating point in Region #3 is stable, it is easy to design the solar array system operating in the region. However, when the solar array is degraded, its output power decreases sharply in this region. Although the operating point in Region #2 is unstable in the case of a constant-power load, the system can be stabilized with the use of shunt regulator and battery discharger. Therefore, for regulated bus systems, Region #2 is the desired operating region for the regulated bus systems.

CHAPTER 4

SMALL-SIGNAL ANALYSIS OF THE MAIN BUS DYNAMICS

4.1 Introduction

In Chapter 3, the large-signal dynamic behavior of spacecraft power systems has been studied using a simplified second-order model with dc characteristics of the power conditioning equipment. It has been shown that the system is stabilized with a large dc gain of the transadmittance of the shunt regulator and a small dc output impedance of the battery discharger. Since only the dc characteristics of each piece of power conditioning equipment was considered in the large-signal analysis, a small-signal analysis is performed in this chapter to observe the system's small-signal dynamics using frequency characteristics of the power conditioning equipment.

Small-signal characteristics of the main bus of a spacecraft power system, operating in various modes (the shunt, charge/shunt, battery charge and discharge), are analyzed for the regulated-bus system using the direct-energy-transfer concept. A methodology is presented to optimize the performances of the bus, such as dc regulation, stability and bus impedance using the system's loop gain. Dynamic performances of the bus are

simulated with small-signal and large-signal component models, using EASY5.

Solar arrays generate their output power over a wide range, according to the changes in cell temperature and illumination level. The operating point of the solar array is determined by its characteristics, the power conditioning equipment and the load. The power conditioning equipment consists of a shunt regulator, a battery charger and a battery discharger. The power conditioning equipment not only balances the power of the system, but also regulates the bus voltage. Throughout a complete orbit cycle, there exist various modes of operation of the system; each piece of conditioning equipment is activated according to the bus voltage. Small-signal dynamic behavior of the bus thus depends on the dynamics of the power conditioning equipment in each mode of operation.

Considering the size and complexity of a spacecraft power processing system, analysis of the system may not be feasible by defining a system entirely in terms of circuit elements. A practical modeling approach is to model each component individually and to define their interconnection. Even though the behavior of individual components may be well understood and documented, once these components are interconnected to form a complex system, the system may not behave as desired, due to unwanted interaction among components.

In order to utilize the modular concept, each component should be modeled and analyzed as an unterminated two-port network; the terminal characteristics of both ports are unknown until the complete system is configured. The two-port modeling allows one to analyze the complete system, with a focus on the local behavior of a particular component. The interaction can then be defined in terms of an impedance matching between components.

In this chapter, small-signal dynamics of the main bus of a spacecraft power system operating in various modes are analyzed by treating each piece of power conditioning equipment as an unterminated component. In Section 4.2, the bus impedance is analyzed in terms of the transadmittance of the power conditioning equipment. The system loop gain is defined and design considerations of the loop gain are discussed. The system's small-signal dynamics in the shunt mode, battery-charge mode and battery-discharge mode are analyzed in the frequency domain, and design consideration of each piece of power conditioning equipment are discussed in Sections 4.3, 4.4 and 4.5, respectively. Finally, conclusions are drawn in Section 4.6.

For the analysis verification, both small-signal and step transient responses of the main bus are simulated with the component models presented in [8] for each mode of the system's operation.

4.2. Dynamics of the System Bus

Figure 4.1 shows a block diagram of a direct-energy-transfer (DET) power system. In the figure, Z_c is the impedance of the main bus filter capacitor, which maintains the bus voltage within acceptable limits during short transients when the power conditioning equipment is not able to regulate the bus. As mentioned before, the power conditioning equipment regulates the bus while maintaining the bus impedance at a low level. To illustrate the small-signal dynamics of the main bus, Fig. 4.2 shows the small-signal equivalent circuit model of the system shown in Fig. 4.1, for each system's mode of operation. In Fig. 4.2, Y is the admittance function of each piece of power conditioning equipment.

Assuming that the dynamics of the spacecraft's load are not yet known, let us first consider a load-unterminated system. The shunt regulator,
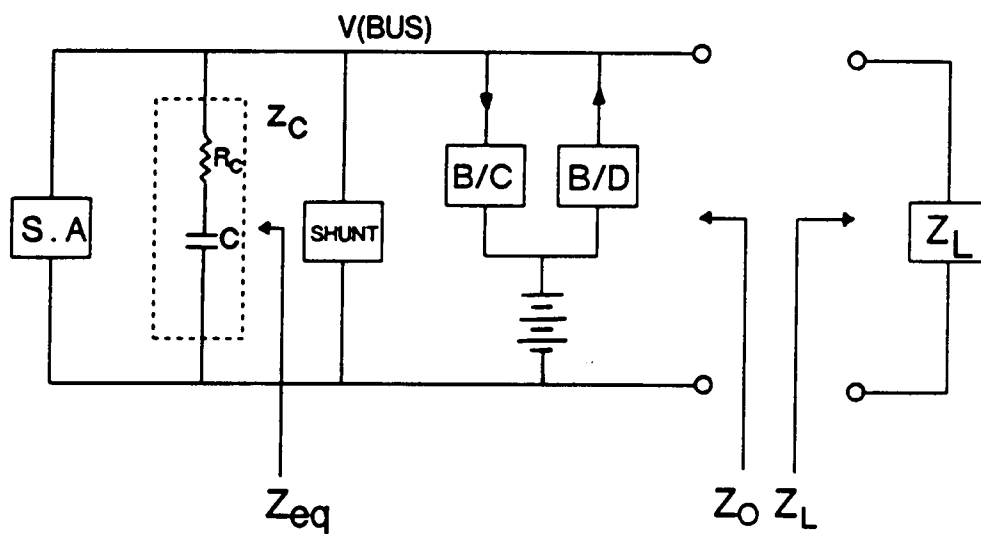
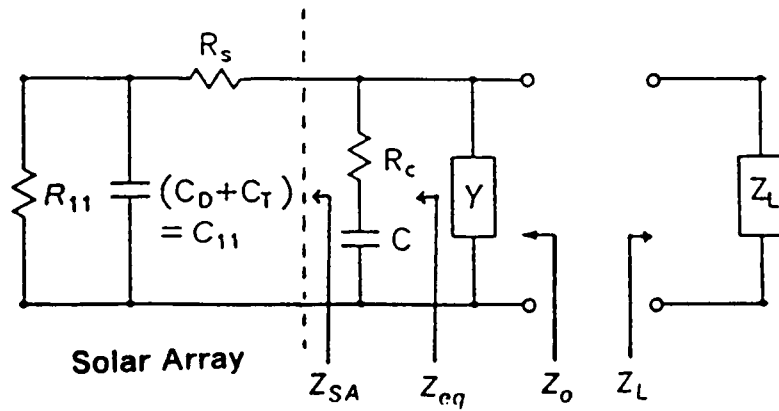Fig. 4.1 Block diagram of Direct-Energy-Transfer
power system

Fig. 4.2 Small-signal equivalent model of Fig. 4.1

R_{11} : $R_D \parallel R_{SH}$ (Dynamic Resistance $\parallel$ Shunt Resistance)

C_{11} : $C_D \parallel C_T$ (Diffusion Capacitance $\parallel$ Junction Capacitance)
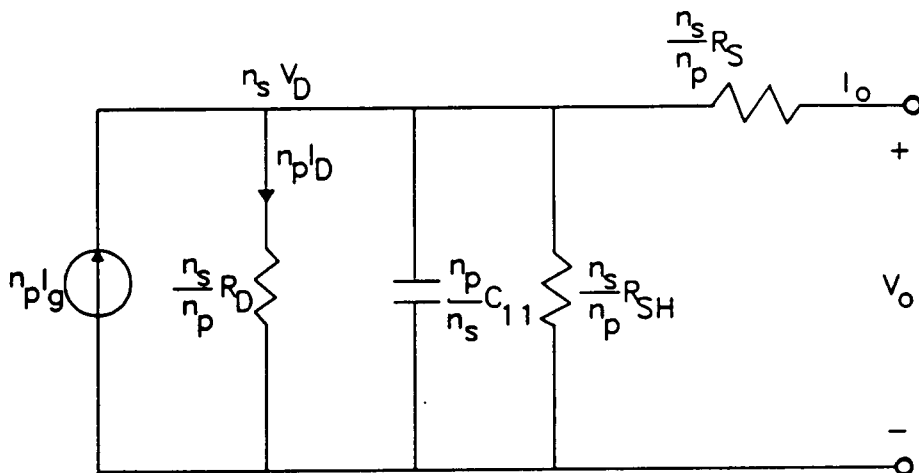

Fig. 4.3 Small-signal circuit model of solar array

105

battery charger (during its bus voltage regulating mode) and discharger function as bus regulators, that is, they regulate the bus voltage by controlling the solar array output current across the source impedance, Z_{eq}. Therefore, the block diagram in Fig. 4.2 forms a simple feedback system, in which the regulator gain function, Y, is the feedback gain to the system. The dynamics of the bus depend on the shape of the system loop gain, T_o , which is defined as

$$T_o = Z_{eq} Y \qquad (4.1)$$

and the output impedance of the regulator, Z_o, is

$$Z_o = \frac{Z_{eq}}{1 + T_o} \qquad (4.2)$$

(These derivations will be clearly shown in a shunt regulator example in the next section.) Thus, if Y is locally stable, then by properly shaping the loop gain, T_o , the system's stability can be ensured and Z_o can be optimized. As discussed in [4], primary considerations in loop gain design are that T_o must drop below unity at a desired frequency with a reasonable stability margin, while, at the same time, T_o should be high at dc to provide good bus regulation.

Before the proper design of Y is considered, Z_{eq} needs to be characterized. Even though the circuit parameter values in Z_{SA} vary widely, depending on the system's operating condition [16], the corner frequency of the pole and zero, due to C_{11}, are much higher than the frequency range of interest, i.e., the loop gain crossover frequency in a typical solar array design.

The circuit model of the solar array's small-signal model is shown in Fig. 4.3. By using this model, the dynamic resistance of the solar array

can be internally calculated under different output conditions. This model is simple and produces good first-order results. Various techniques are given in the literature for determining the parameter values of the model. For this first-order ac model, the parameter values are dependent on the output voltage and current, cell temperature, cell illumination and physical cell dimension. It is therefore necessary to take these factors into account when model parameters are calculated.

The computer model of the array is described as lumped R and C, which are functions of the number of cells in series and parallel (n_S and n_P, respectively [8]).

The parameter values, I_s, C_D, C_T and R_S, are given. The dynamic resistance, R_D, is determined by the operating condition of the solar array, I_o, and V_O in the model program. That is,

$$n_s V_D = V_o + \frac{n_s}{n_p} R_S I_o$$

From the diode equation,

$$I_D = I_{do} \left[\exp \left(\frac{Q V_D}{kT} \right) - 1 \right]$$

Then,

$$R_D = 1 / \left(\frac{dI_D}{dV_D} \right) = 1 / \left[I_{do} \frac{Q}{kT} \exp \left(\frac{Q V_D}{kT} \right) \right]$$

Although the capacitance value, $C_D + C_T$, also varies according to the operating condition [16], one typical value at a constant current region (the output voltage range from zero to peak-power voltage) is used in this simulation.

The computer simulated plot (Fig. 4.4) is obtained using the circuit model shown in Fig. 4.3. In Fig. 4.2, since C_{11} is very small and can be considered an open circuit in the frequency range of interest, Z_{eq} becomes

$$Z_{eq} = (R_{11} + R_S) \parallel (R_C + \frac{1}{sC}) = \frac{R_{11}(sR_C C + 1)}{sC(R_{11} + R_C) + 1}$$

The low frequency value of Z_{eq} is then $R_{11} + R_S \cong R_{11}$. Since, in the current source region of the solar array, the dynamic resistance, R_D, is much larger than R_C, the pole is at $\omega_p \cong 1/(C R_{11})$ and the zero is at $\omega_z = 1/(C R_c)$. The high frequency value of Z_{eq} is R_C , which will be the peak value of the bus impedance if the loop gain T_o is properly designed. The peak bus impedance determines the amount of overshoot/undershoot due to the step-load transient, and the zero at ω_z is the primary factor of the settling time of the system. Therefore, these two important parameters for the bus impedance are primarily functions of the impedance of bus filter capacitor, Z_C . Even though a smaller R_C will give better performance, it may be necessary to add external series resistance in Z_C to have a more reliable system loop gain.

According to Z_{eq}, the power conditioning equipment admittance function, Y, can be designed with the loop gain design criteria discussed earlier. Then the load terminated bus impedance, Z_B, and the loop gain, T_B, can be designed as a function of Z_o and T_o.

$$Z_B = Z_o \parallel Z_L \qquad (4.3)$$

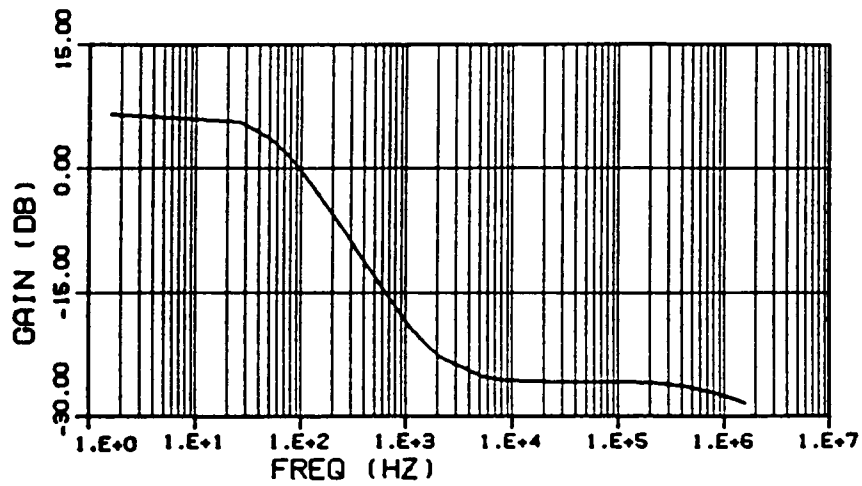$$T_B = T_o \frac{1}{1 + \frac{Z_{eq}}{Z_L}} \qquad (4.4)$$

Fig. 4.4 Source impedance, Z_{eq} (0 dB = 1 Ω)

$$R_{11} = 4.4\Omega, \quad C = 1500\mu F, \quad R_C = 0.05\Omega,$$

$$f_p = \frac{1}{2\pi R_{11}C} = 24Hz, \quad f_z = 2.2kHz$$

Thus, if one can ensure $|Z_o| << |Z_L|$, the bus impedance is independent of the load. Also, from Eq. (4.4), stability of the load-terminated bus will be ensured if $|Z_{eq}| << |Z_L|$. In other words, the load interactions to the system bus and its stability condition are characterized by the impedance ratio of $|Z_{eq}|$ and $|Z_L|$. Therefore, one can concentrate on the system loop gain design without Z_L, and the interaction analysis can then be performed.

The loop gain design with Z_{eq} for each piece of power conditioning equipment will be discussed in the following sections.

4.3. System in Shunt Mode

Shunt regulators are used to regulate the bus voltage during the period when excess solar array power is available. When the solar array output power is larger than the required load power, the bus voltage will increase. The shunt regulator is then activated to limit the bus voltage to a required level. During the shunt mode, the bus voltage is regulated by varying the shunt current through the shunt element.

In the direct-energy-transfer system, the operating point of the bus voltage is usually chosen to be a little lower than the peak-power voltage, which has high source impedance. The solar array behaves like a current source in a voltage range from zero to peak-power voltage. That is, the source impedance of the solar array, Z_{SA}, is very large in this voltage range. The filter capacitor makes the impedance low at high frequencies. To make the solar array source a stiff voltage source, the source impedance should also be low at low frequencies. By introducing a shunt regulator with proper voltage loop gain, the output impedance of the solar array system, including the shunt, can be made low for all frequencies.

To define the loop gain of the system, a control block diagram is introduced in Fig. 4.5. The shunt regulator senses the output voltage of the solar array and produces the shunt current to regulate the bus voltage. In this voltage control scheme, the load current, i_L , and input voltage can be considered as input variables. Therefore, the transfer function from the load current to the output voltage becomes

$$\frac{\Delta V_B}{\Delta i_L} \; = \; \frac{Z_{eq}}{1 + Z_{eq} \, Y_{sh}} \; \equiv \; Z_o \qquad\qquad (4.5)$$

where Δi_L : load current variation

Δv_B : bus error voltage

The transadmittance function, Y_{sh} , can be explained as follows. For a typical linear shunt regulator,

$$Y_{sh} \; = \; \frac{\Delta i_{sh}}{\Delta v_B} \; = \; H_{sh} \, G_{sh}$$

where H_{sh} : compensation network transfer function

G_{sh} : transconductance of the shunt elements

From Eq. (4.5), the bus voltage loop gain becomes $T_o = Z_{eq} \, Y_{sh}$. This loop gain determines the system stability.

The loop gain design considerations are described in detail in reference [4]. The loop gain should be high at dc to have tight regulation, but should be below unity at high frequencies, where the parasitic capacitance of control circuitry prevents proper control. A large loop gain bandwidth is desired to have fast system response. To obtain all these characteristics, the feedback compensator should be designed as shown in Fig. 4.6b. The first plot shows the output impedance of the solar array plus filter
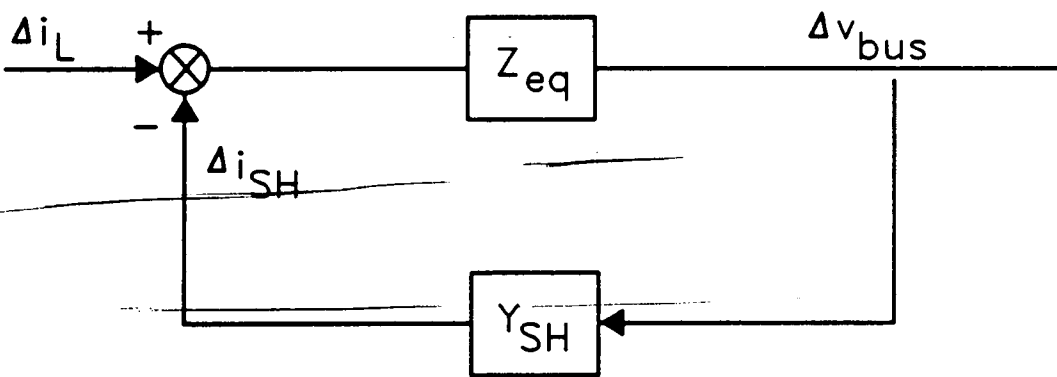
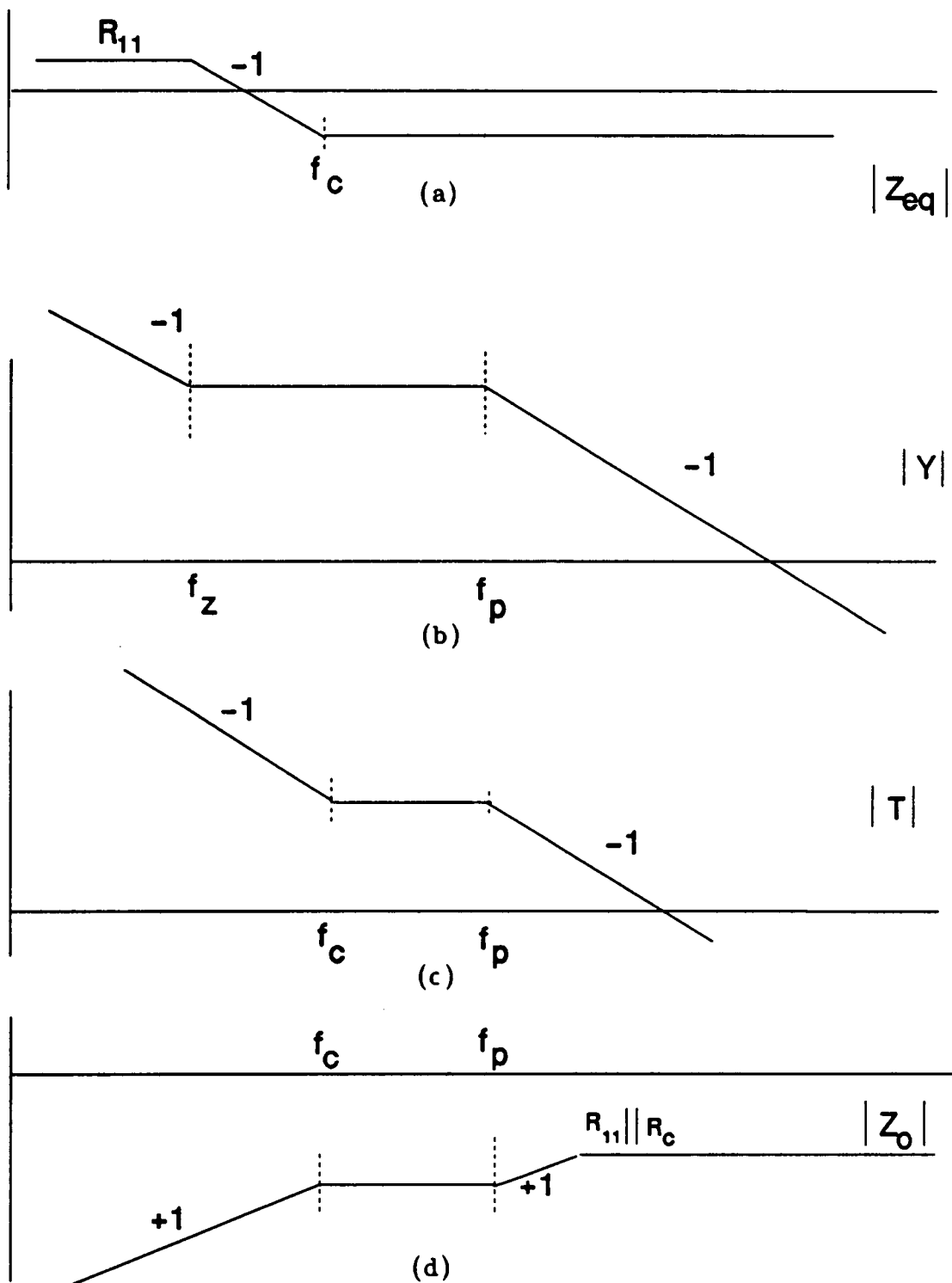**Fig. 4.5 Control block diagram of shunt system**

Fig. 4.6 Desired assymtotes of transfer functions in shunt mode
(+1 slope = 20 dB/dec   -1 slope = -20dB/dec)

113

capacitor. The magnitude of R_{11} varies according to the solar array's operating condition, output voltage and output current.

As shown in Fig. 4.6b, the feedback compensator of the shunt regulator can be designed with a two-pole one-zero compensator; one pole at zero, one zero before f_c and the other pole at a high frequency in the range of 50-100 kHz in order to obtain the desired output impedance characteristics, as shown in Fig. 4.6d.

Simulation of shunt mode

A typical solar array power system with a shunt regulator is modeled using small-signal models. The system is composed of three types of equipment, such as a solar array, shunt regulator and load converter. In this simulation, the load converter is modeled with a constant-power load. Frequency response of a solar array system with the converter load is simulated in the shunt mode, using small-signal models. In this simulation, Y_{sh} of the shunt regulator was implemented with a two-pole one-zero compensator network. The simulation results, shown in Fig. 4.7, agree well with the corresponding plots in Fig. 4.6.

Figure 4.8 shows the step-load transient response using the time-domain model. At the beginning of simulation, the system is in shunt mode with a light load (396 W). At 1 msec, the load is step-changed (10%) to 356.4 W, so that the shunt current increases and the bus voltage shows an overshoot at the moment. From the output impedance curve, settling time is predicted because the smallest eigenvalue of the system dominates system response time. The output impedance can be expressed in the form of transfer function:
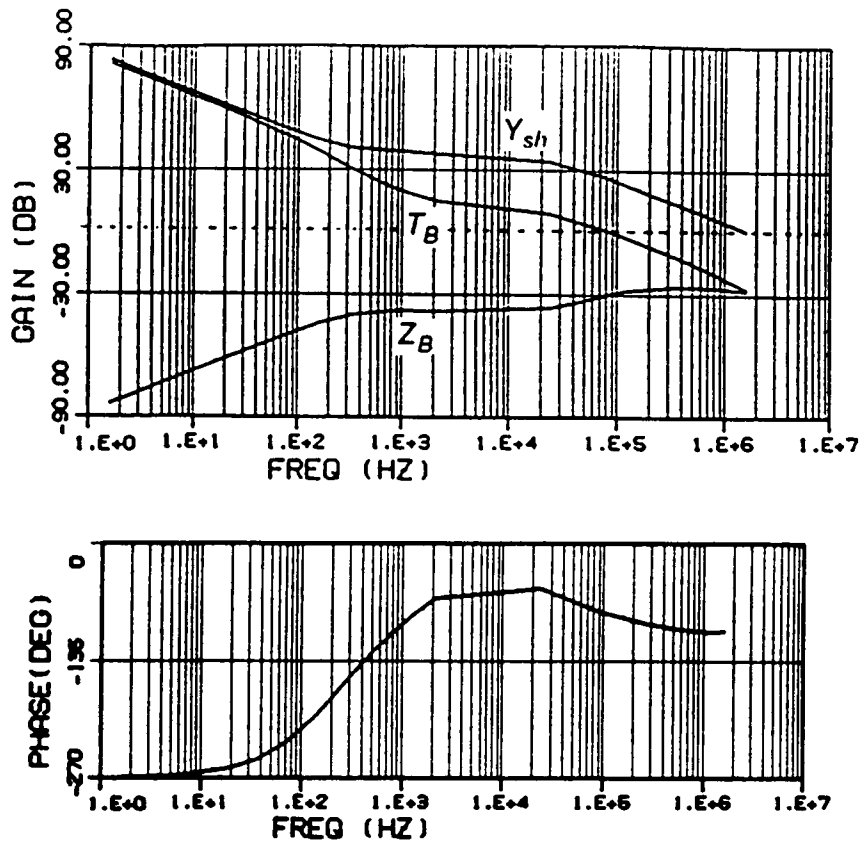
Fig. 4.7.a Transadmittance of shunt, loop gain
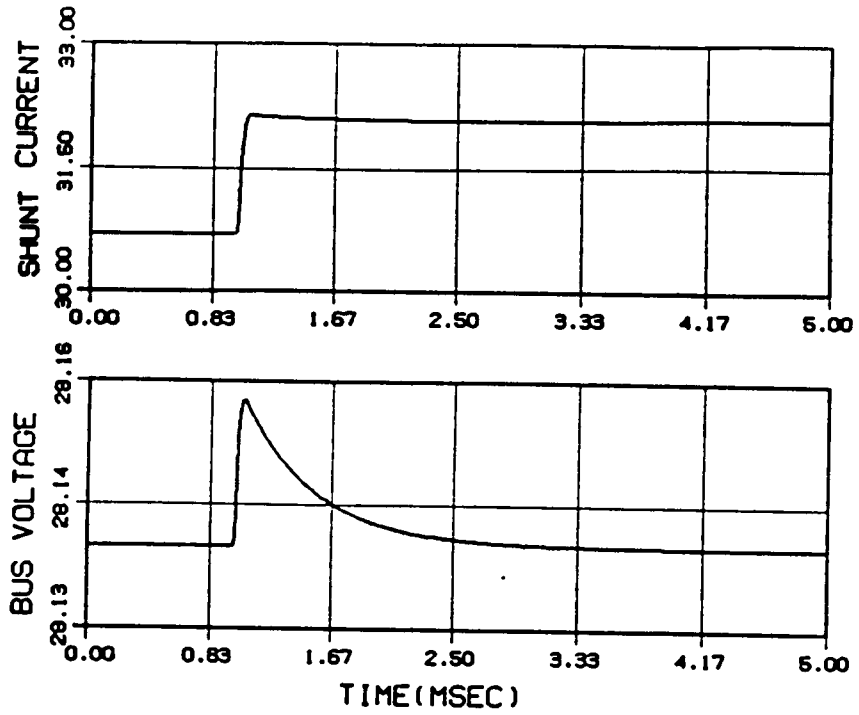and bus impedance
.b Phase of loop gain

Fig. 4.8 Simulation of step-load transient
in shunt mode

$$Z_o = \frac{k \left(1 + s/\omega_{z1}\right) \left(1 + s/\omega_{z2}\right) \ \dots}{\left(1 + s/\omega_{p1}\right) \left(1 + s/\omega_{p2}\right) \ \dots}$$

where $\omega_{p1} < \omega_{p2} < \ \dots$. Since the first pole, ω_{p1}, is at about 300 Hz in this case, the time constant becomes 0.5 msec and the settling time is 2 msec, assuming that the settling time is about four times of the time constant. This prediction agrees well with time-domain simulation result in Fig. 4.8.

4.4 System in Battery-Charge Mode

Several operating conditions exist in the battery-charging mode. There is a period when the solar array can supply the spacecraft load, but the solar array power is not sufficient to charge batteries at their full commanded rate. During this period, the spacecraft bus is regulated by controlling the charge current as a function of the bus voltage error. When there is sufficient current from the solar array to charge the batteries at their commanded rates, the charge rate will be regulated by the charger current regulator. During this period, excess current from the solar array will be shunted by the shunt regulator, hence the bus is regulated by the shunt regulator. When batteries are fully charged, the trickle charger is activated to compensate for the internal loss in the batteries.

As far as dynamics of the bus are concerned, the battery charger controls the bus dynamics only during the **bus voltage regulating mode**. When both the charger and shunt regulator are activated, that is, when the battery charger is in the **charging current regulating mode**, the bus dynamics are controlled by the shunt regulator and the battery charger subsystem can be considered as a load to the bus.

Figure 4.9 shows a schematic of the battery charger, which uses the buck converter topology. An input filter is added to attenuate the buck converter's pulsating input current. It shows, functionally, two control amplifiers for the bus voltage control and the charging current control. During the bus voltage regulating mode, the output of the charging current control amplifier is disabled. As a result, the output of the voltage control amplifier is the PWM error signal, which determines the duty cycle of the converter. To regulate the bus voltage, it is sensed and compared with a reference voltage to produce an error voltage which controls the amount of charging current. Thus, its function is the same as a shunt
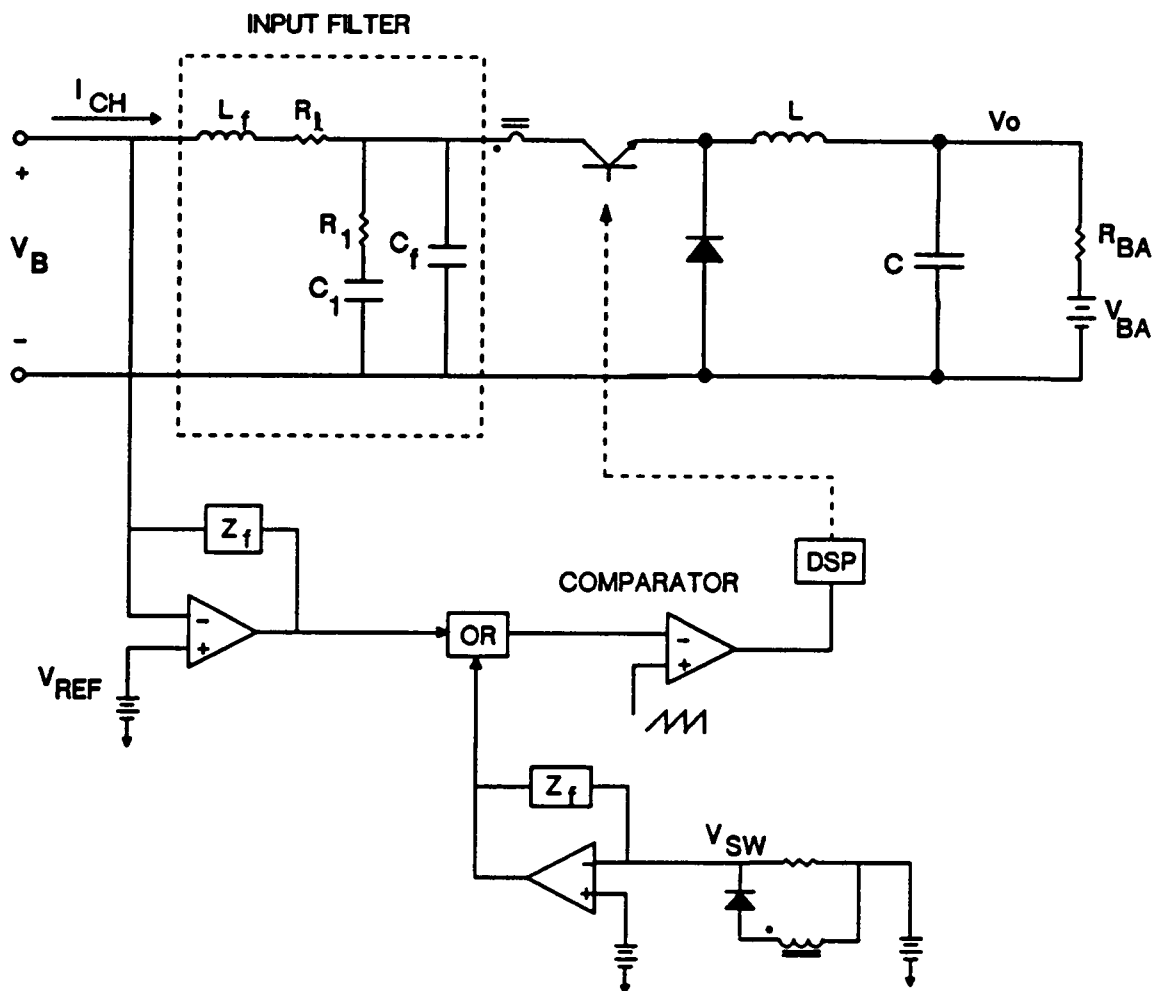
Fig. 4.9 Battery charger circuit using buck converter topology

$L = 50\mu H,\quad C = 100\mu F,\quad L_f = 10\mu H,\quad C_1 = 450\mu F,\quad R_1 = 0.5\Omega$

$C_f = 26\mu F,\quad V_B = 28V,\quad V_{BA} = 25V,\quad f_s = 100kHz$

regulator in this mode. For a linear charger, its design strategies are similar to those of a shunt regulator. However, for a PWM charger, which has size and efficiency advantages over a linear charger, it is more complicated to design the control circuit because of the dynamics in the switching converter and an excessive phase delay introduced by the input filter. Figure 4.10 shows the block diagram of the battery charger in Fig. 4.9, during the bus regulating mode.

The admittance function of the charger is

$$Y_{ch} = \frac{\hat{i}_{ch}}{\hat{v}_B} = G_1 + H_v FM G_2 \qquad (4.6)$$

Since, during the bus voltage regulating mode, only the feedforward loop is activated, there should not be any local stability problem. However, the charger's output filter and the input filter may introduce excessive phase lag to the admittance function of the charger, Y_{ch} . This excessive phase delay in Y_{ch} may cause stability problem in the system's loop gain, $T_o = Y_{ch} Z_{eq}$. Thus, it is very important to design an input filter with suitable damping, such that the phase delay of Y_{ch} at the system's loop gain crossover frequency can be at a minimum. Also, it must meet the ripple-current attenuation specification with low output impedance to minimize the interaction with the buck converter.

Figure 4.9 shows the input filter chosen for this study. The filter transfer function for small R_ℓ is

$$H_s = \frac{1}{1 + \frac{s}{Qw_o} + \frac{s^2}{w_o^2}} \qquad (4.7)$$
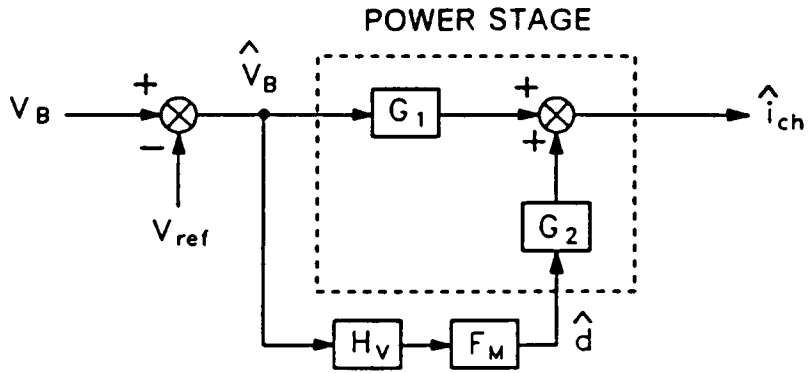
where

Fig. 4.10 Block diagram of battery charger
with voltage loop

$$G_1 = \dfrac{\hat{i}_{ch}}{\hat{v}_B} \qquad \text{; open-loop input admittance}$$

$$G_2 = \dfrac{\hat{i}_{ch}}{\hat{d}} \qquad \text{; control to charge current transfer function}$$

H_v ; bus voltage feedforward compensator

FM ; PWM gain

$$w_o = \frac{1}{\sqrt{L_f C_f}} \quad , \quad Q = R_1 \sqrt{\frac{C_f}{L_f}} \quad , \quad \text{if} \quad C_1 R_1 >> \frac{L_f}{R_1} \qquad (4.8)$$

Thus, this filter can attenuate an input with a -40 dB/dec slope and, at the same time, the damping factor, Q, can be controlled. The input filter resonant frequency, ω_o, is designed at one decade below the switching frequency (100 kHz), so that the charge-current ripple is well below 1% of its dc value. With this input filter and the buck converter, the control-to-charge current transfer function, G_2, is plotted in Fig. 4.10. As shown, the resonant peaking at 10 kHz, due to the input filter, is damped out and the phase delay is quite reasonable to compensate.

Since, in practical designs, $|G_1| << |G_2 H_v FM|$, as shown in Figs. 4.11 and 4.12, the loop gain, T_o, in Eq. (4.1) can be approximated by $T_o \cong Z_{eq} G_2 H_v FM$. To shape the loop gain T with the feedforward compensation function, H_v, the product data, $Z_{eq} G_2 FM$, can be used. Z_{eq} and G_2 are shown in Figs. 4.4 and 4.12. According to this data, H_v is designed such that the loop gain can have a -20 dB/dec slope at low frequencies and proper phase margin at crossover frequency. Therefore, ω_{z2} of H_v is chosen at the resonant frequency of H_F to improve the phase margin, as shown in Fig. 4.13. Figures 4.14a and 4.14b show the resultant loop gain, T_B, and bus impedance, Z_B.

Figure 4.15 shows the step-load transient response in this mode of operation, using a time-domain simulation model. The simulation starts in the steady state of the battery-charge mode. At 0.5 msec, a step-load change from 1000 W to 900 W is applied to the system. The charger then performs as a bus voltage regulator, so that the charger current increases to take over the excess current from the solar array source. The bus voltage response gives about 0.06 V overshoot and 0.1 msec settling
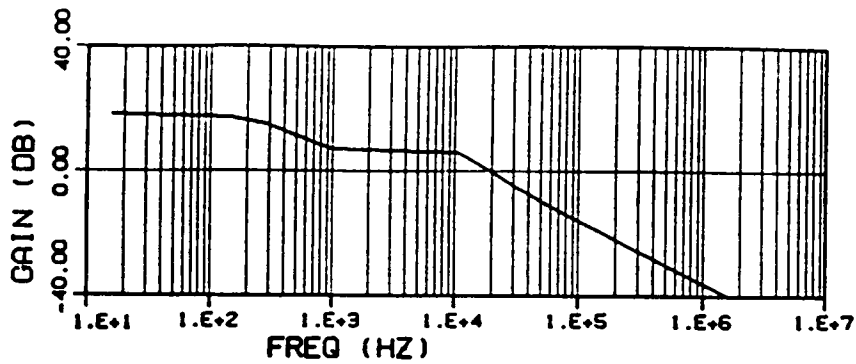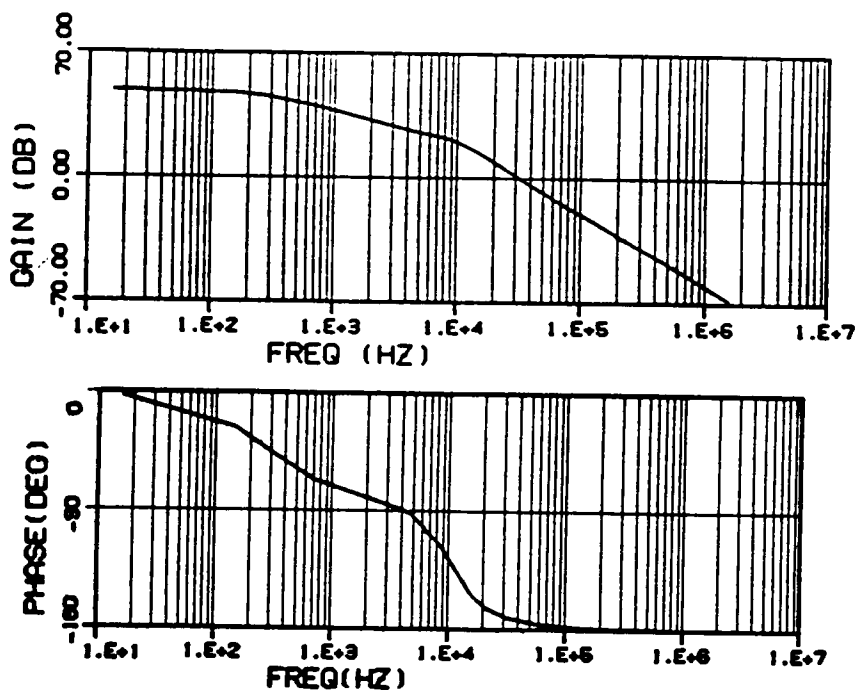
Fig. 4.11 Open loop admittance, G_1

Fig. 4.12 Control-to-input current
Transfer function, G_2

123

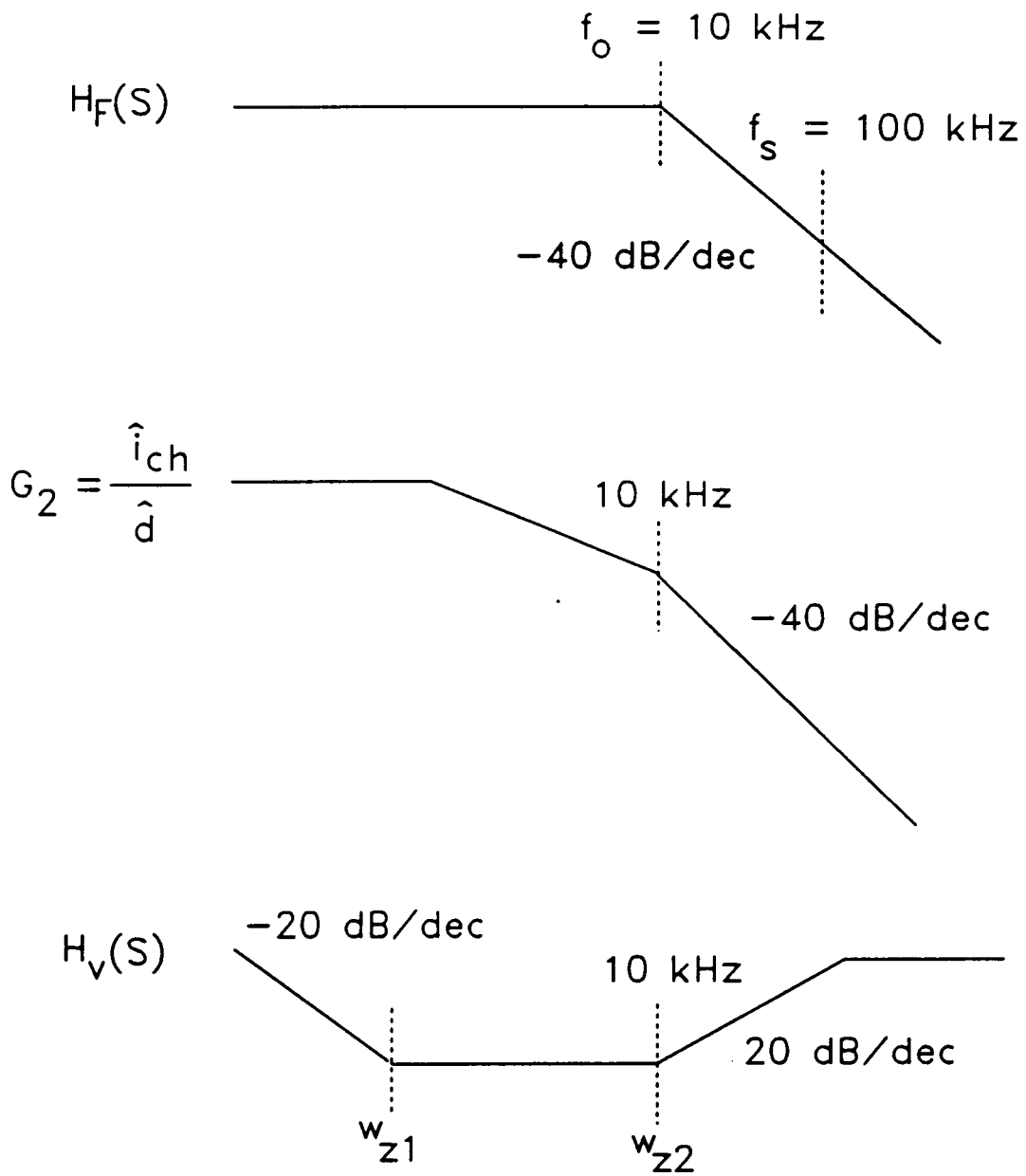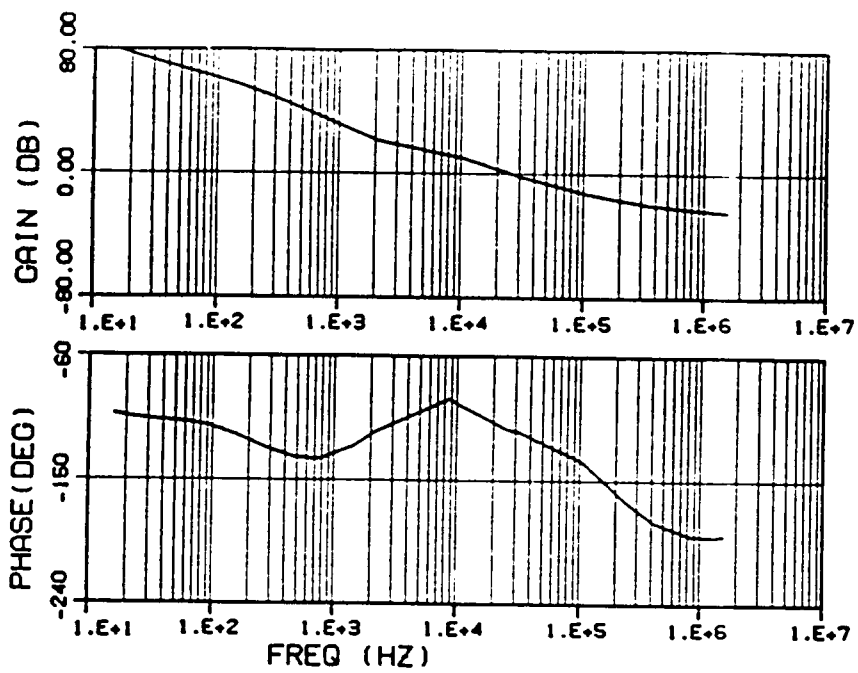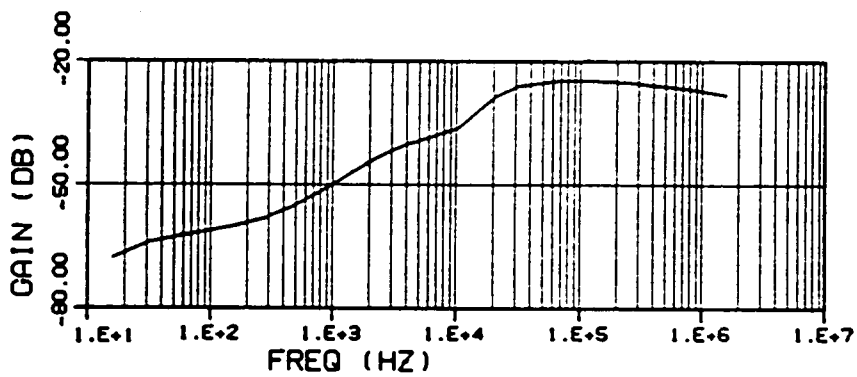Fig. 4.13 Asymptotes of transfer functions

GAIN (DB) vs FREQ (HZ)

PHASE(DEG) vs FREQ (HZ)

(a)

GAIN (DB) vs FREQ (HZ)

(b)

Fig. 4.14.a Loop gain, T_B
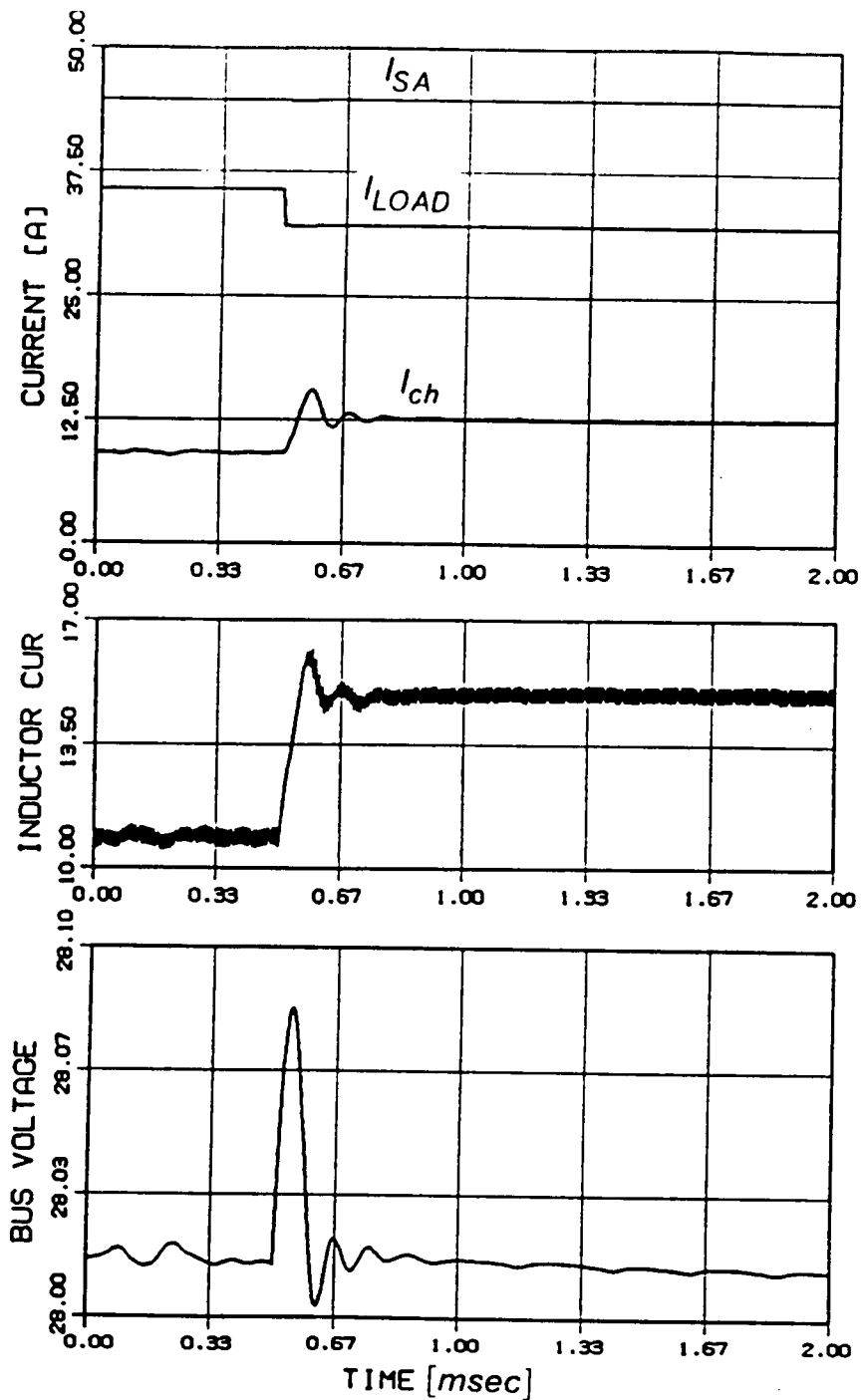 .b Bus impedance, Z_B

125

Fig. 4.15 Step-load transient in battery-charge mode

time. It can be approximately predicted from the shape of the output impedance.

For the charging current regulating mode, the output current of the charger should be sensed and fed back to control the duty ratio of the PWM charger. The control block diagram of the constant current mode is shown in Fig. 4.16. The current loop gain should be designed to have high gain at low frequency and wide bandwidth with proper stability margin. The loop gain is determined by the transfer function from input voltage to output current.

$$\frac{\hat{i}_o}{\hat{v}_B} = \frac{G_3}{1 + G_4 H_i FM}$$

where

$$G_3 = \frac{\hat{i}_o}{\hat{v}_B} \qquad G_4 = \frac{\hat{i}_o}{\hat{d}}$$

Therefore, the loop gain T is

$$T = G_4 H_i FM$$

In the buck converter,

$$G_4 = \frac{V_B}{R} \frac{(1 + s/w_z)}{1 + s/Qw_o + s^2/w_o^2}$$

where

$$w_z = \frac{1}{RC} \quad w_o = \frac{1}{\sqrt{LC}} \quad Q = R\sqrt{C/L}$$
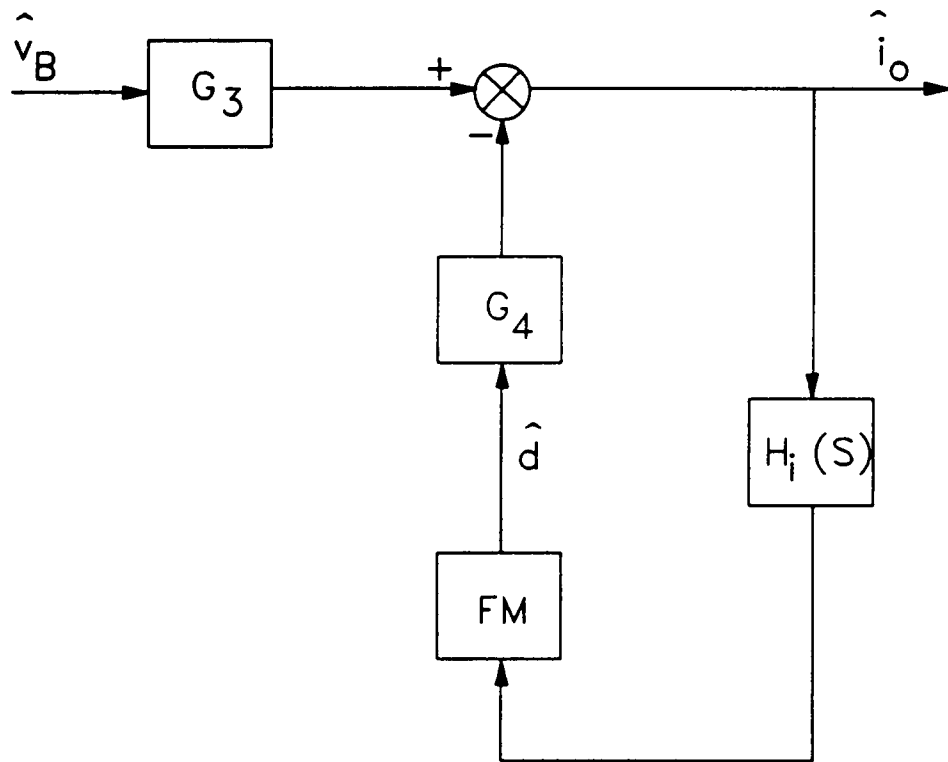
Fig. 4.16 Control block diagram of constant current mode

For the battery charger, the load resistance, R, is very small because the load is a battery. The G_4 has two separate poles at low and high frequencies instead of a double pole at resonance frequency. The zero locates at high frequency. Since the high frequency pole cancels the effect of zero, the overall shape of G_4 becomes as shown in Fig. 4.17, which looks like a system with one low frequency pole.

To satisfy the loop gain requirement, the current loop compensator should be designed as an integrator with a low frequency zero. By properly adjusting the gain of the compensator, the loop gain can have a maximum bandwidth which is normally half of the switching frequency of the converter. The simulated loop gain of the charger is shown in Fig. 4.18.

During a constant-current charging mode, the charging-current level, as well as the battery output voltage and temperature, should be continuously monitored to control the charging current at a preset value. In the constant current charging mode, since the charging current is limited, the bus voltage feed-forward loop is deactivated. The bus voltage will then rise up and the system will enter a charge/shunt mode. Therefore, the charger and the shunt regulator are both activated, and the system loop gain becomes

$$T = Z_s (Y_{ch} + Y_{sh})$$

where Y_{ch} is an input admittance of the battery charger. Since, in this mode, Y_{ch} is much smaller than Y_{sh}, as shown in Figs. 4.19 and 4.7, respectively, the bus impedance of the constant current charging mode can be considered to be the same as that of the shunt mode.
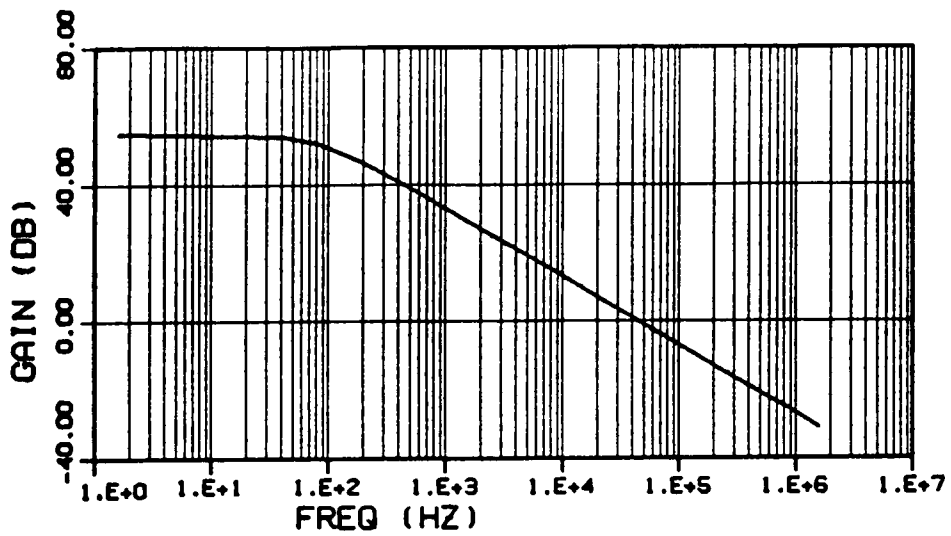
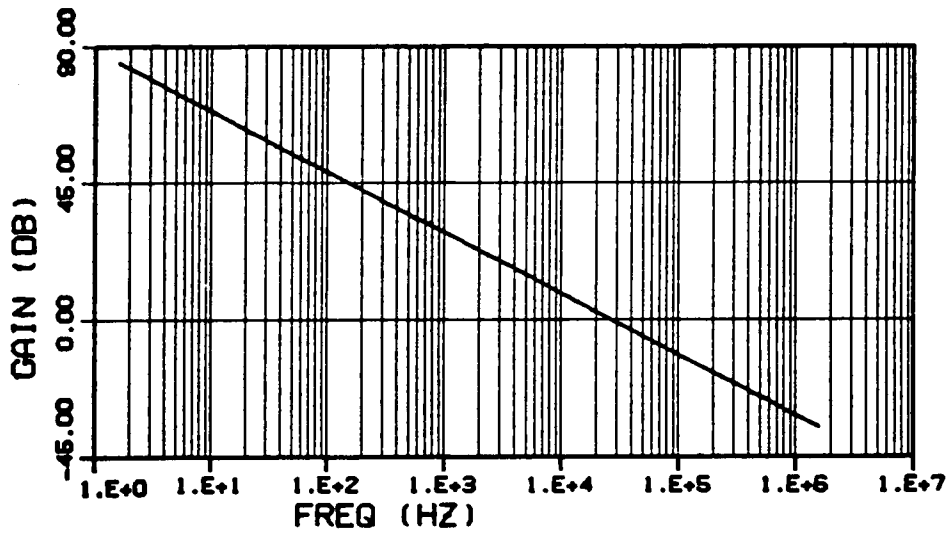Fig. 4.17 Control-to-output current
Transfer function, G_4

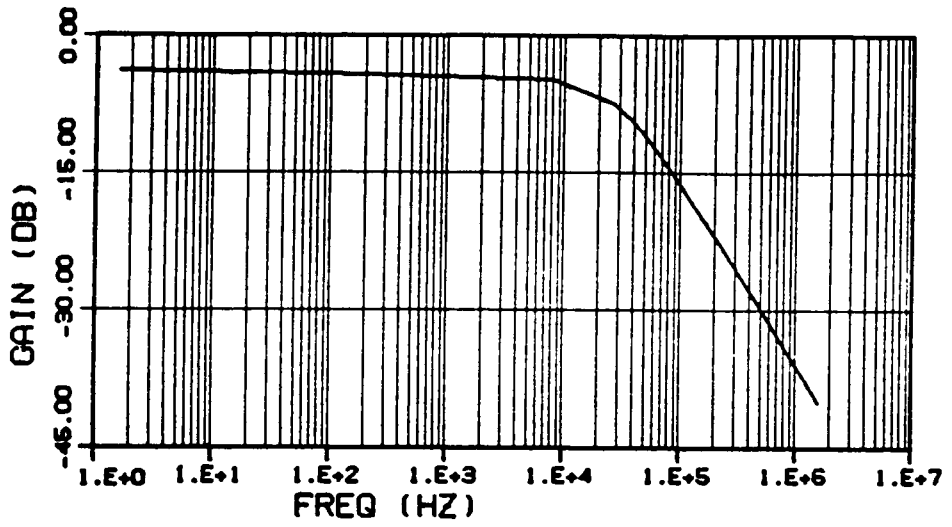Fig. 4.18 Loop gain, T, of constant current mode

130

Fig. 4.19 Closed-loop input admittance, Y_{ch}

4.5 System in Battery-Discharge Mode

When there is insufficient solar array current to supply the spacecraft load, the battery discharger is activated. For a regulated dc bus system, the bus dynamics are dependent mainly on the dynamic characteristic of the regulator. Figure 4.20 shows the system in the battery-discharge mode. Since the output of the battery discharger is the bus voltage, the bus filter capacitor should be treated as a part of the battery discharger. Thus, the system is simplified, as the regulator and equivalent load impedance seen by the regulator, Z_{eq}' , which is the parallel combination of the spacecraft load impedance, Z_L, and the solar array output impedance, Z_{SA} . The regulator performance parameters, such as audio-susceptibility, output impedance and loop gain, can be derived as an implicit function of Z_{eq}'. However, if Z_{eq}' is complex-frequency dependent, it is neither easy to obtain design insight nor to analytically determine the stability of the regulator. For a spacecraft power system, it may not even be feasible to find an analytical function for Z_{eq}' . Quite often, a resistive load is commonly assumed when a regulator is designed. However, even though the regulator is designed to be stable and well-behaved, using a resistive load, stability and performance cannot be guaranteed because of the dynamic interaction between the regulator and Z_{eq}' , as discussed in Section 4.2.

As discussed in detail in [2], the regulator can be designed independently of the dynamics of its load, using the unterminated two-port analysis. Therefore, the load-terminated system performance can be expressed explicitly as a function of Z_{eq}'. For instance, the bus impedance is
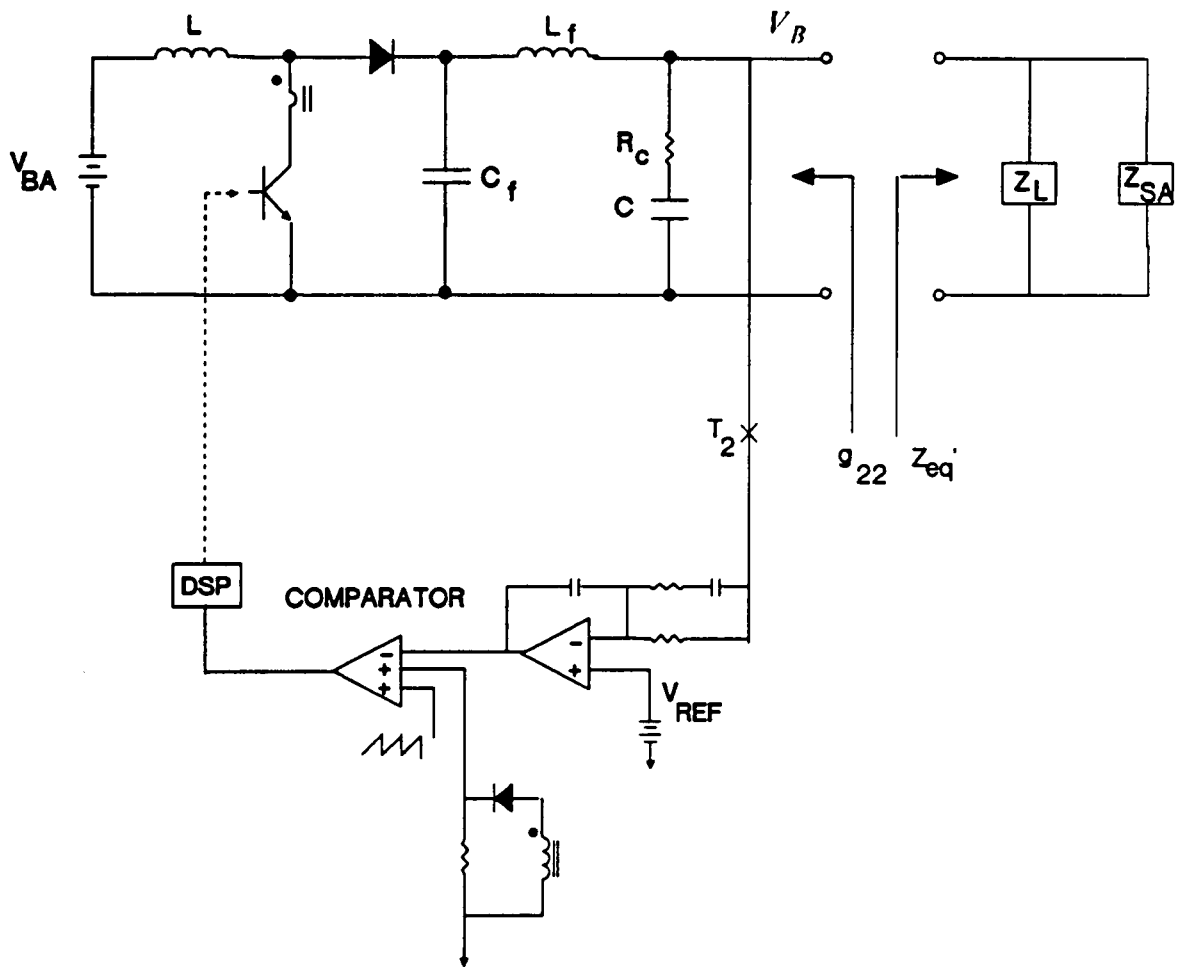
Fig. 4.20 Schematic of battery discharger with secondary filter

$L = 13.5\mu H$, $C_f = 100\mu F$, $L_f = 2.5\mu H$, $C = 1500\mu F$, $R_C = 0.05\Omega$

$V_{BA} = 25V$, $V_B = 28V$, $f_s = 100kHz$

$$\frac{\hat{v}_B}{\hat{i}_B} = \frac{g_{22}}{1 + \dfrac{g_{22}}{Z_{eq}'}} \equiv \frac{g_{22}}{1 + T_B'} \qquad (4.9)$$

where g_{22} is the output impedance of the unterminated regulator and is independent of the dynamics of Z_{eq}'. Thus, one can easily design the unterminated regulator with optimum performance (g's) ensuring stability. As shown in Eq. (4.9), the stability of the load-terminated regulator can be determined using the system loop gain T_B' . If the unterminated regulator is stable (g_{22} is stable), then the sufficient condition for system stability is simply $|g_{22}| < |Z_{eq}'|$ for all frequencies. By examining these quantities, the degree of interaction can be also characterized, i.e., the larger the difference between these quantities, the less the interaction of the dynamics of Z_{eq}'. Therefore, a design specification for g_{22} can be determined by examining $|Z_{eq}'|$, which can be obtained empirically or through computer simulation, if an analytical model is not available.

For the discharger, a boost regulator with a secondary output filter, as shown in Fig. 4.20, has been designed. The current mode control, in which the output voltage and the switch current are sensed for feedback control, is employed because of the many advantages over a single-loop control. These advantages include superior dynamic response with good stability margins, inherent overcurrent protection and current sharing among parallel modules. Unlike the battery charger, since the battery discharger supplies full spacecraft load power during the complete darkness period, a parallel module scheme may be necessary to share the power. In addition to the many advantages of the parallel-module scheme over single module power processing, such as higher efficiency and smaller size, redundancy can be easily incorporated, a very important consideration for a system requiring high reliability.

The secondary filter exists to attenuate the switching ripple at the bus, because the pulsating diode current flowing through the output filter network generates considerable switching ripple at the bus due to the ESR of the filter capacitor. Design of a current-mode controlled boost regulator is discussed in many papers [17, 18]. Also, the secondary filter design consideration is discussed in [19].

Frequency-domain simulations and time-domain simulation are shown in Figs. 4.21-4.23. Figure 4.21 shows the loop gain of the boost regulator measured at T_2, as marked in Fig. 4.20. It can be seen that the secondary filter resonant frequency at 10 kHz, which is placed above the loop gain crossover frequency, obtains minimum interactions from this filter. As it clearly shows, if the loop gain is increased beyond a certain gain (i.e., factor of 3), the phase margin decreases rapidly and the regulator becomes unstable due to the interaction with the secondary filter. Designing the resonant frequency of the secondary filter depends on the bus voltage ripple specification.

Figure 4.22 shows the bus impedance, including Z_L and Z_{SA}. The peaking, at around 1 kHz, is due to the limitation on the loop gain crossover frequency discussed earlier. With these parameter values designed from the small-signal analysis, a time-domain simulation was performed, as shown in Fig. 4.23. The bus voltage response, with a load step-change of 10%, shows good dc regulation and a reasonable settling time.
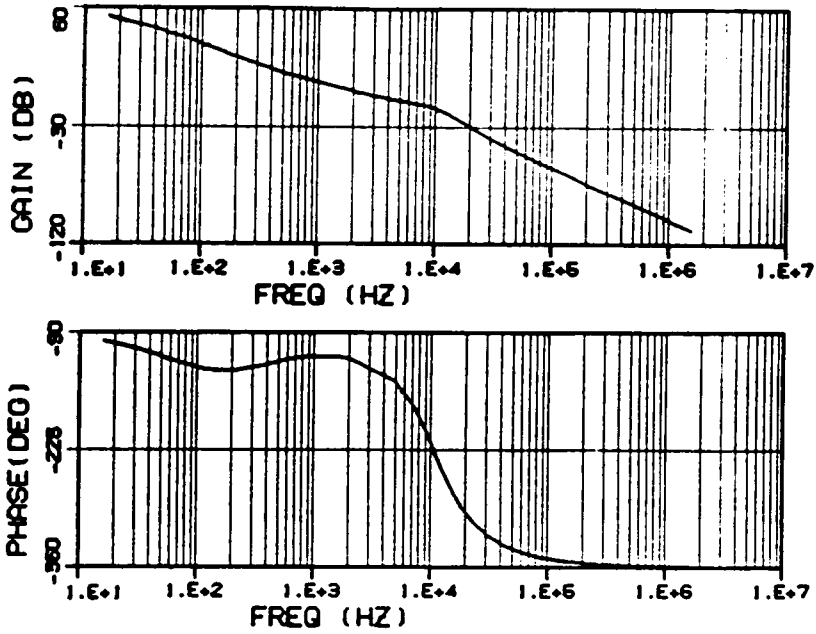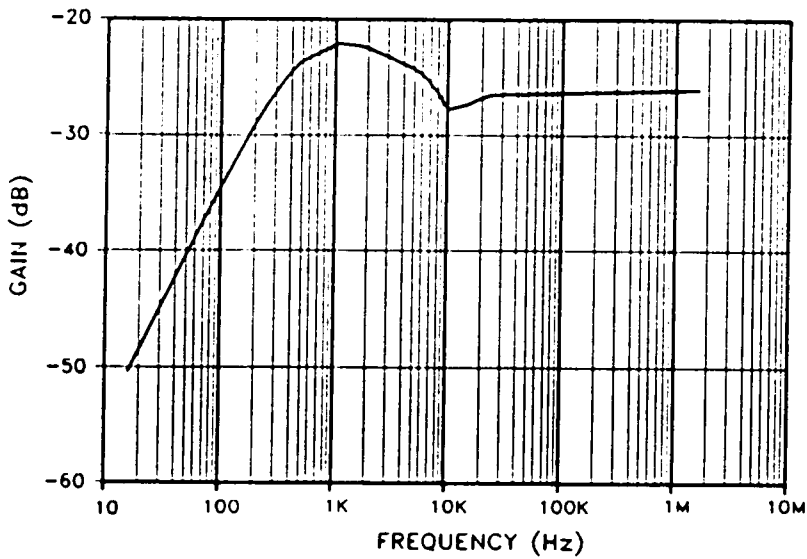
Fig. 4.21 Loop gain T_2

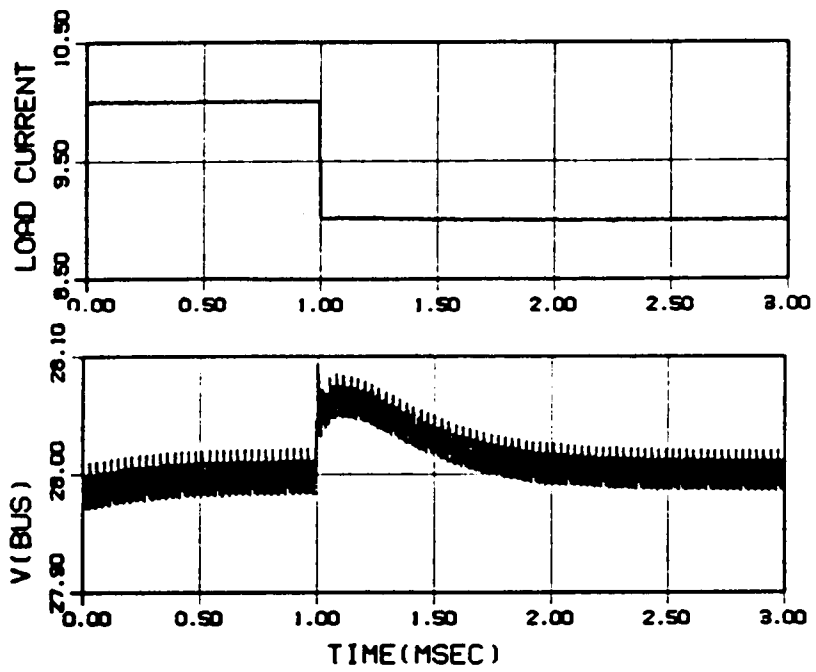Fig. 4.22 Bus impedance in battery-discharge mode

136

Fig. 4.23 Step-load transient in battery-discharge Mode

4.6 Conclusions

Design, analysis and simulation of the main bus dynamics of spacecraft power systems, in all possible modes of operation, have been presented. A two-port subsystem coupling method is utilized, in which a system is broken into manageable pieces. For each system's mode of operation, the power conditioning equipment is analyzed as an unterminated two-port. The main bus dynamics, such as stability and output impedance, are analyzed with a focus on the transadmittance, Y, of each power conditioning equipment and its terminating impedance.

The main bus impedance, Z_B, and the system loop gain, T_B , are derived as explicit functions of the load impedance. This analysis not only characterizes the main bus dynamics, but also identifies the load interaction criteria of the main bus.

Design considerations of the power conditioning equipment for each system's mode of operation are discussed. Using the system's loop gain, minimum output impedance, faster settling time and good stability margins are considered. For shunt regulators, a linear-type full shunt is designed. The output impedance of the partially-shunted solar array system is also derived. Design considerations of the charger in the bus voltage regulating mode are discussed. Large phase delay, introduced by an input filter (which is necessary in the buck converter), forces down the system loop gain crossover frequency very low to stabilize the system. An input filter is designed to minimize the phase delay at the loop gain crossover, with suitable damping providing the required attenuation of the switching current ripple to the bus.

The boost converter, using current mode control, is designed. A secondary filter is added to reduce the switching ripple voltage at the bus. Two feedback loops are designed to optimize the load unterminated output

impedance, g_{22}, ensuring local stability. The bus impedance and system loop gain are derived to analyze the system stability.

A complete DET power system model has been configured using previously-developed small-signal and time-domain simulation component models. Small-signal dynamics and load step transient response of the main bus are simulated to verify the performed design and analysis for each system's mode of operation.

CHAPTER 5

ANALYSIS AND SIMULATION OF VARIOUS SPACECRAFT POWER SYSTEMS

5.1 Introduction

Many different power systems and power conditioning equipment have been developed to avoid high heat dissipation in the power system, because it is difficult to get rid of heat in space. For the regulated bus system, various shunt regulators and subsystems, such as linear shunt and PWM shunt regulators, and sequential shunt and partial shunt subsystems, have been used to reduce the heat dissipation in the shunt circuit. In the linear shunt, the active elements of the power shunt section operate in the linear mode, while in the PWM shunt the active elements operate in the switching mode. The PWM shunt dissipates less power than the linear shunt in the active elements, because the switches operate either in a saturation region or a cutoff region. In the partial shunt system, the bus voltage is regulated by shunting current from a lower portion of solar

array, instead of shunting from the whole solar array, thus dissipating less power.

The peak power tracking system has been introduced to achieve efficient operation of the solar array without any shunt dissipation. PWM type regulators, in series with the solar array source, provide a means of tracking the peak power point of the solar array. As the power level of spacecraft grows in large spacecraft, such as a space station or space platform, the conventional power system configuration with a shunt regulator may not be adequate to handle the thermal problem in the shunt regulator. Bus voltage regulation, using solar array switching techniques, could alleviate the thermal problem.

In this chapter, various power systems, such as a solar array switching system, partial shunt system and peak power tracking system, are investigated. Dynamic characteristics of these subsystems are analyzed and their design strategies are identified. Each subsystem is modeled and simulated to verify the qualitative analyses.

In Section 5.2, operation characteristics of two different solar array switching systems, a solar array switching unit (SASU) with a linear shunt regulator and a PWM-type sequential switched shunt regulator (SSSR), are investigated through analysis and simulations. A partially-shunted solar array system is modeled and simulated in Section 5.3, to show its advantages compared with the full shunt system in terms of thermal dissipation. In Section 5.4, operation characteristics of the peak power tracking system are introduced. To show the capabilities of this modeling technique, an existing spacecraft power system, Cosmic Background Explorer (COBE), is modeled and simulated for the various system's operating modes and one orbit cycle in Section 5.5.

CHAPTER 5

5.2 Solar Array Switching System

5.2.1 Introduction

Most regulated-bus spacecraft power systems use a shunt regulator to limit the bus voltage during the sunlight period. The shunt regulator is essential, because the output voltage of the solar array rises almost two times as high as its normal operating voltage when the spacecraft exits an eclipse. This is because the solar cell temperature is relatively low immediately after the eclipse period.

A linear shunt system is subject to potentially high heat dissipation in the shunt elements. This problem becomes more serious as the power level goes up. Therefore, a solar array switching unit (SASU) system is more desirable for the high power systems. A SASU system can regulate the bus voltage and minimize heat dissipation in the power conditioning equipment. The SASU regulates the bus voltage by switching off unnecessary sections of the solar array when excess power is available. As shown in Fig. 5.1, this is accomplished by either short-circuiting (shunt switching) or open-circuiting (series switching) a portion of the solar array [20].

In the case of short-circuiting, transistors successively short out parallel sections of the array to maintain the bus voltage below some desired limit. Although shorting an individual cell is acceptable, problems arise if a string of series-connected cells is shorted. When the series-connected cells are shorted, the operating point of each cell is ideally at the point of short circuit current and zero voltage. However, any poor cell producing mismatched output in the cell string causes a current level different from the short circuit current. This moves the operating point of the cells to a nonzero output voltage and, consequently, the mismatched cell is
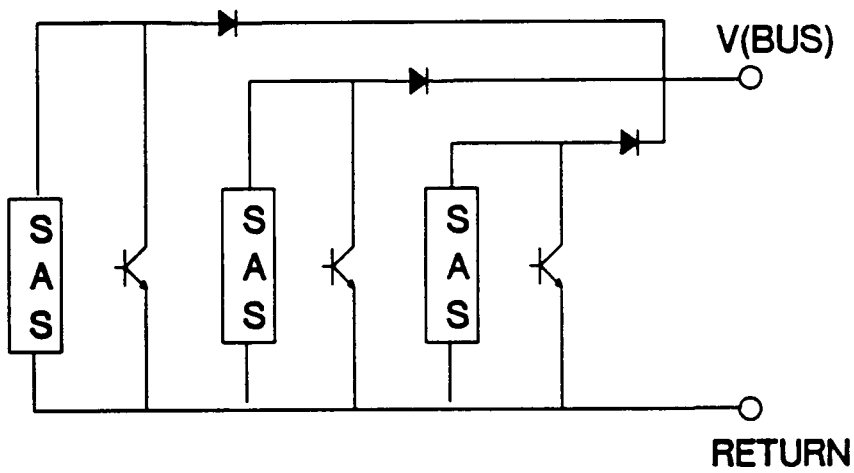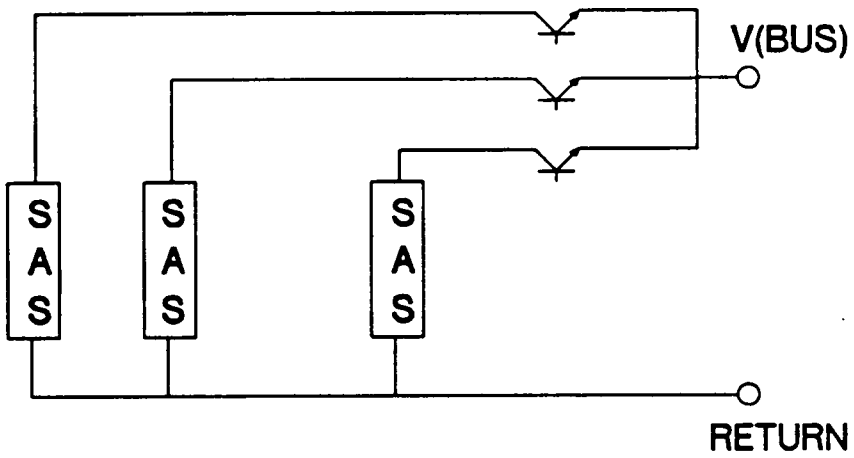
Fig. 5.1 Basic configurations of solar array switching system

reverse-biased. Thus, this cell dissipates the power generated in the other cells and can result in a damage in the cell.

Two techniques are used to avoid the problem: series-paralleling of solar cells and the use of bypass diodes. The series paralleling technique increases the numbers of series blocks and parallel strings in the solar array module, as shown in Fig. 5.2a. This arrangement can lower the reverse-bias voltage when one cell is bad or the cells are partially shaded. The other approach is to use a bypass diode connected across one or more series blocks in the module, as shown in Fig. 5.2b. The bypass diode becomes forward-biased when a series block becomes reverse-biased. This limits the power dissipated in this block as well as providing a low-resistance path for the module or a current path for branch strings.

An alternative technique is to open-circuit the parallel sections. An advantage of this technique is that series-blocking diodes are not required if the switches have sufficient blocking capability. Also, there is no stress on the array due to shadowing, because any poor cell can provide smaller voltage and the other cells in the same string produce larger voltage to match with the bus voltage. A disadvantage is that the lead inductance in series with the switch may cause a high voltage spike when the switch is opened. Also, the full array current must pass through the switch when the array power is needed by the loads, thus producing additional loss.

In large spacecraft power systems, since the lead length from the solar array panel to the switches is long, the solar array lead inductance becomes significant. The lead inductance, L, with the solar array switching action may cause the voltage spike on either the switching device or the bus. The inductance, L, sees higher $\frac{di}{dt}$ in the open-circuiting case than the
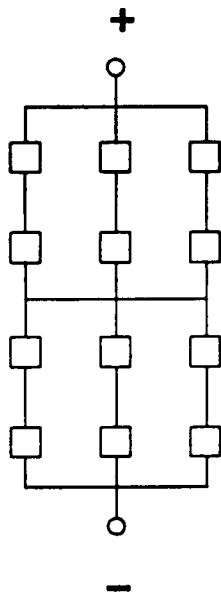
3 Parallel Strings
2 Series Blocks
2 Cells per Substrings
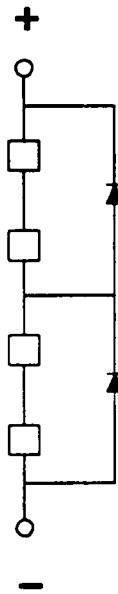
2 Series Blocks
2 Celles per Substrings

(a)

(b)

Fig. 5.2 Module circuit techniques of solar array

short-circuiting case. This is because the current changes from the operating point to the open circuit current, zero, of the solar array in the open-circuiting. In short-circuiting, however, the current changes from the short circuit current to the operating point current of the solar array, which is very small because the operating point is in the constant current region.

5.2.2 Comparison of two SASU systems

Two types of solar array switching systems have been studied and tested in references [22, 23]. The first, shown in Fig. 5.3, uses a solar array switching unit with a shunt regulator. In this scheme, a linear shunt regulator, without the attendant high thermal dissipation, can be used. This has been accomplished by combining an active linear shunt regulator with a sequentially switched control, which expands or contracts the size of the solar array to minimize the power dissipation in the shunt regulator.

The combined operation of the active and switched-array sections is described by the operation of the system during exit from an eclipse. When the spacecraft is in the eclipse, the bus voltage is less than the reference voltage setting of the shunt regulator. Given these conditions, the shunt is turned off and the current sensors are producing a 'count-up' signal so that all of the array is switched on.

As the spacecraft exits the eclipse, the full array is on and the output current is sufficient to charge the battery and supply the load demand. The bus voltage rises continuously until it reaches the voltage reference of the shunt regulator. The shunt regulator activates to absorb excess solar array's output power. When the shunt current increases to a lower preset value (e.g. 2 amperes), the 'count-up' signal is turned off. As the current increases to an upper preset value (e.g. 5 amperes), the shunt
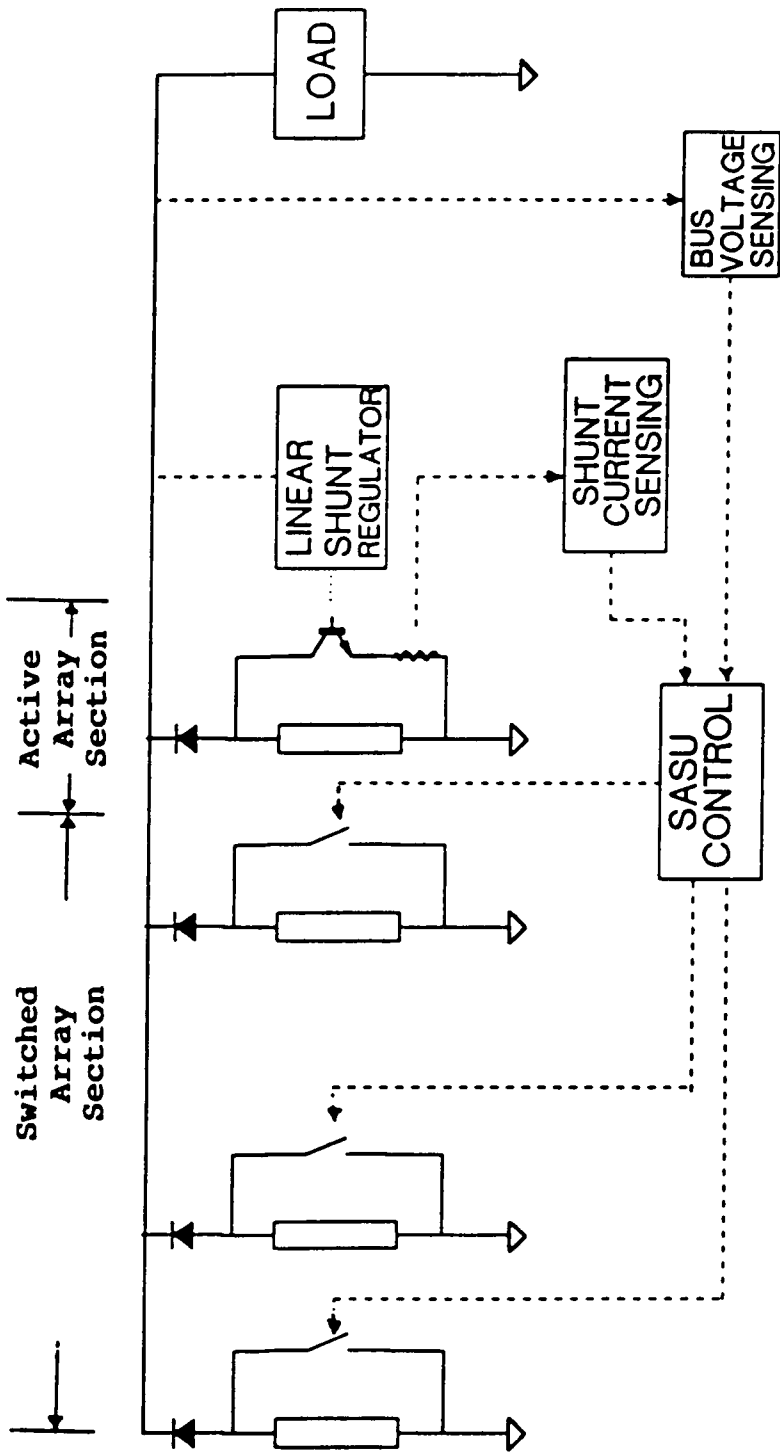
Fig. 5.3 Solar array switching unit with shunt regulator

current sensors initiate a 'count-down' signal, which switches off the array sections, one by one, until the shunt current is stabilized between 2 amperes and 5 amperes. This is defined as the hysteresis band of the SASU. During this time, the switching action stops and the shunt regulator regulates the bus with the active array section. Figure 5.4 shows the array characteristics under static condition.

There are two major design parameters for this SASU control. One is the size of each array segment. The sizes of both the active- and switched-array segments must be properly chosen to minimize the linear shunt dissipation and to ensure good voltage regulation.

The upper limit of the hysteresis band is determined by the short-circuit current of the active array sections. The size of the active array section is determined by the amount of shunt dissipation allowed in the power system. The lower limit should be larger than the short-circuit current of one switched-array section, to stay in the shunt mode of operation during a transient period. The width of the hysteresis band must also be larger than the short-circuit current of one switched-array section, to avoid repeated turning on and off of a switched section.

The rate of switching for switched array sections depends on how fast the shunt regulator responds to the line and load changes.

To illustrate how this SASU system works, the SASU system shown in Fig. 5.3 is modeled and simulated, as shown in Fig. 5.5. Initially, 240 parallel solar array strings, each consisting of 412 solar cells in series, are connected to the main bus. The solar array parameters are chosen to have a bus voltage of 160 V with about 5.5 kW power capacity. In the simulation, a constant power type of load, 5.1 kW, is initially applied to the bus. The excess power of the solar array is consumed in the shunt regulator. When the load power decreases linearly, the shunt current re-
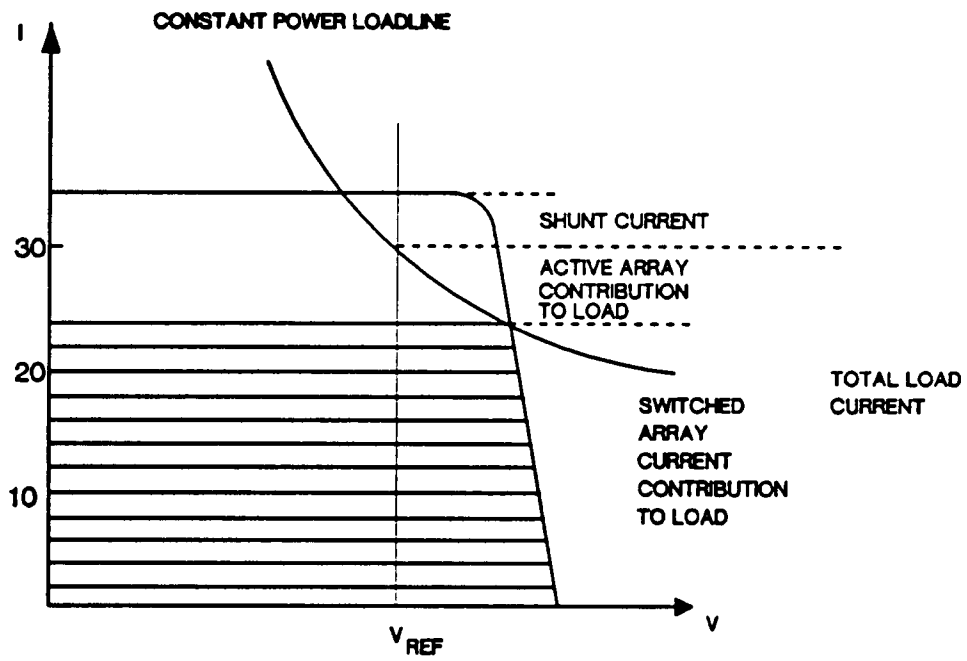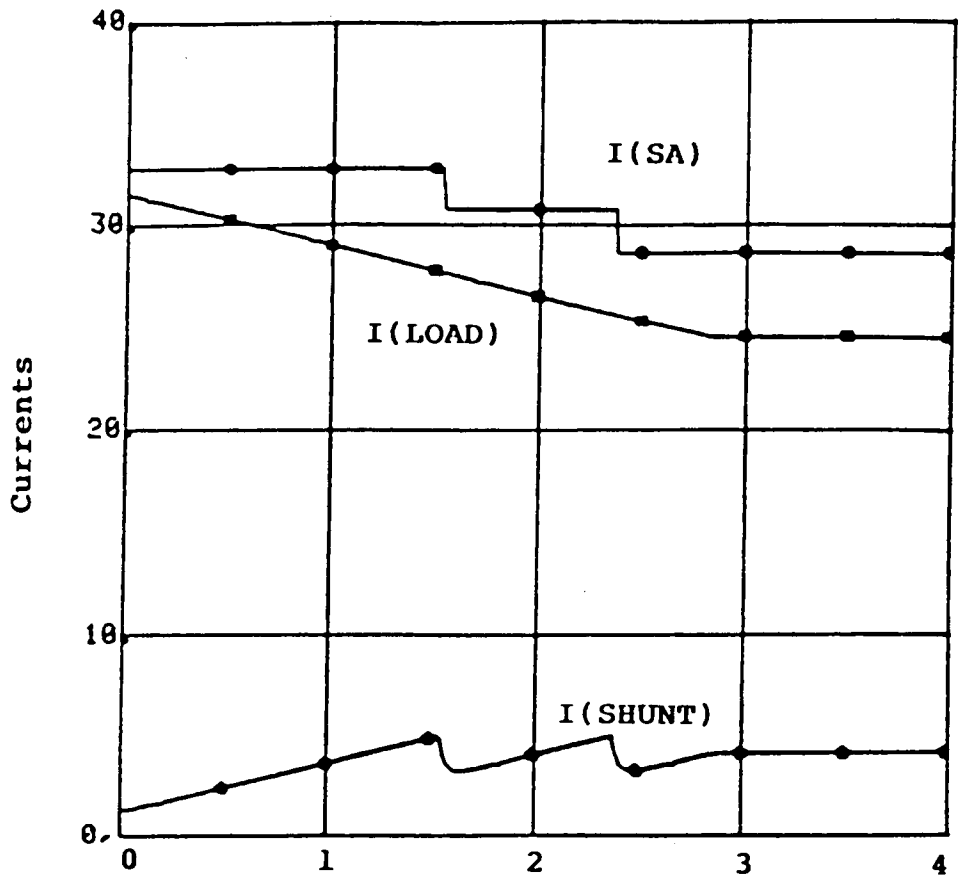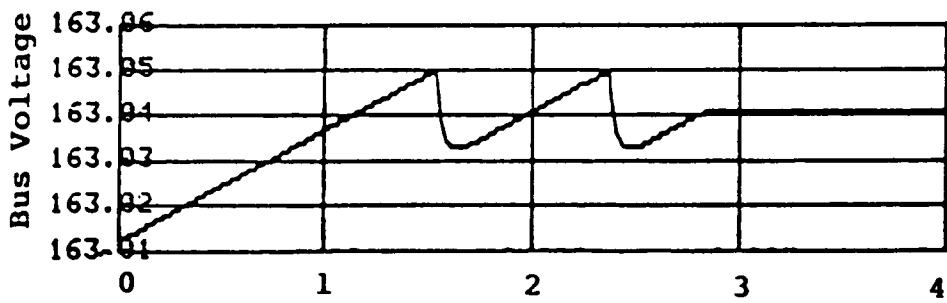
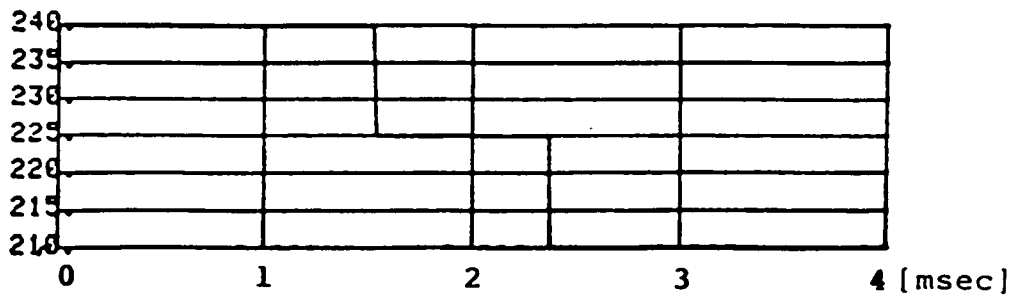Fig. 5.4 I-V characteristics of SASU with shunt regulator

Fig. 5.5 Simulation result of SASU with shunt regulator

aches 5 amperes and one switched-array section, consisting of 15 parallel strings, is switched off. The solar array current and the bus voltage drop accordingly. The switching action stops as the shunt current settles within the hysteresis band. Since the shunt regulator is always activated, the bus voltage is well regulated.

The second scheme, shown in Fig. 5.6, is called a PWM-type sequential switching shunt regulator (SSSR). Bus voltage regulation is accomplished in a manner similar to a PWM switching power converter. The excess power from the solar array is shunted by PWM-controlled switches and the bus filter capacitor charges and discharges continuously to keep its voltage constant by a feedback control.

As shown in the figure, the bus voltage error signal is fed to several comparators. The error signal is compared with a ramp voltage summed with a reference voltage for each solar array section. The reference voltage to each comparator is slightly different, so that only one transistor is pulse-width-modulated, while all the other transistors are either fully on or fully off. Bus voltage ripple is minimized by having only one array section at a time under PWM control.

The switching frequency and the size of each array section are the design parameters of this system. A higher switching frequency and smaller array sections can provide lower output ripple. The maximum operation frequency is limited by the switching speed of the switching devices, such as a transistor and diode, and the time delay of the solar array due to internal capacitance. The smaller array sections require more switches and more complex wiring.

Figure 5.7 shows the results of a simulation of a subsystem model having the SSSR and a constant power load. The simulation shows how
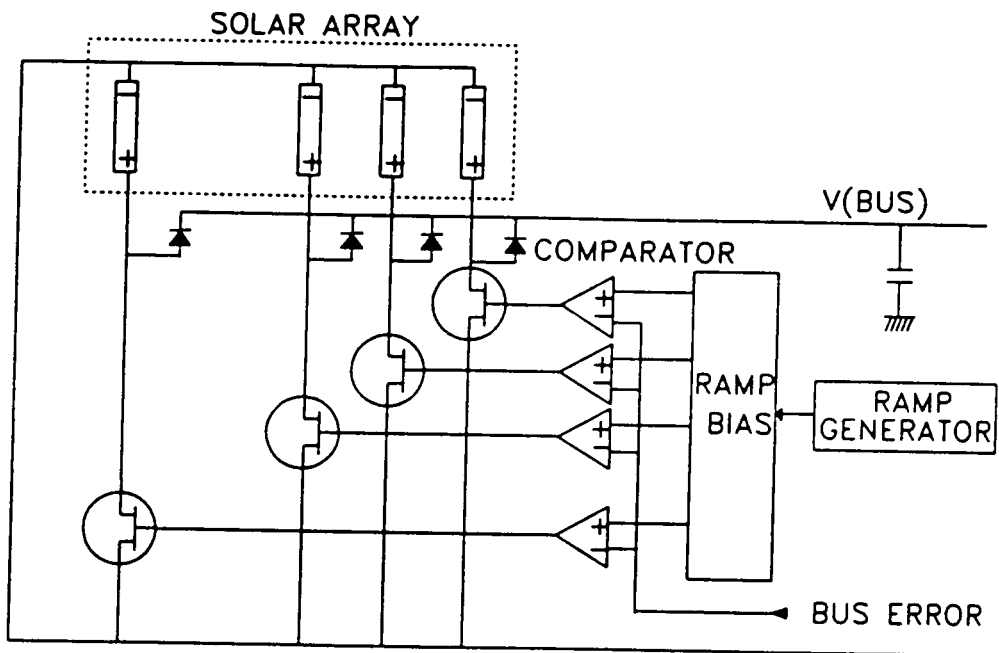
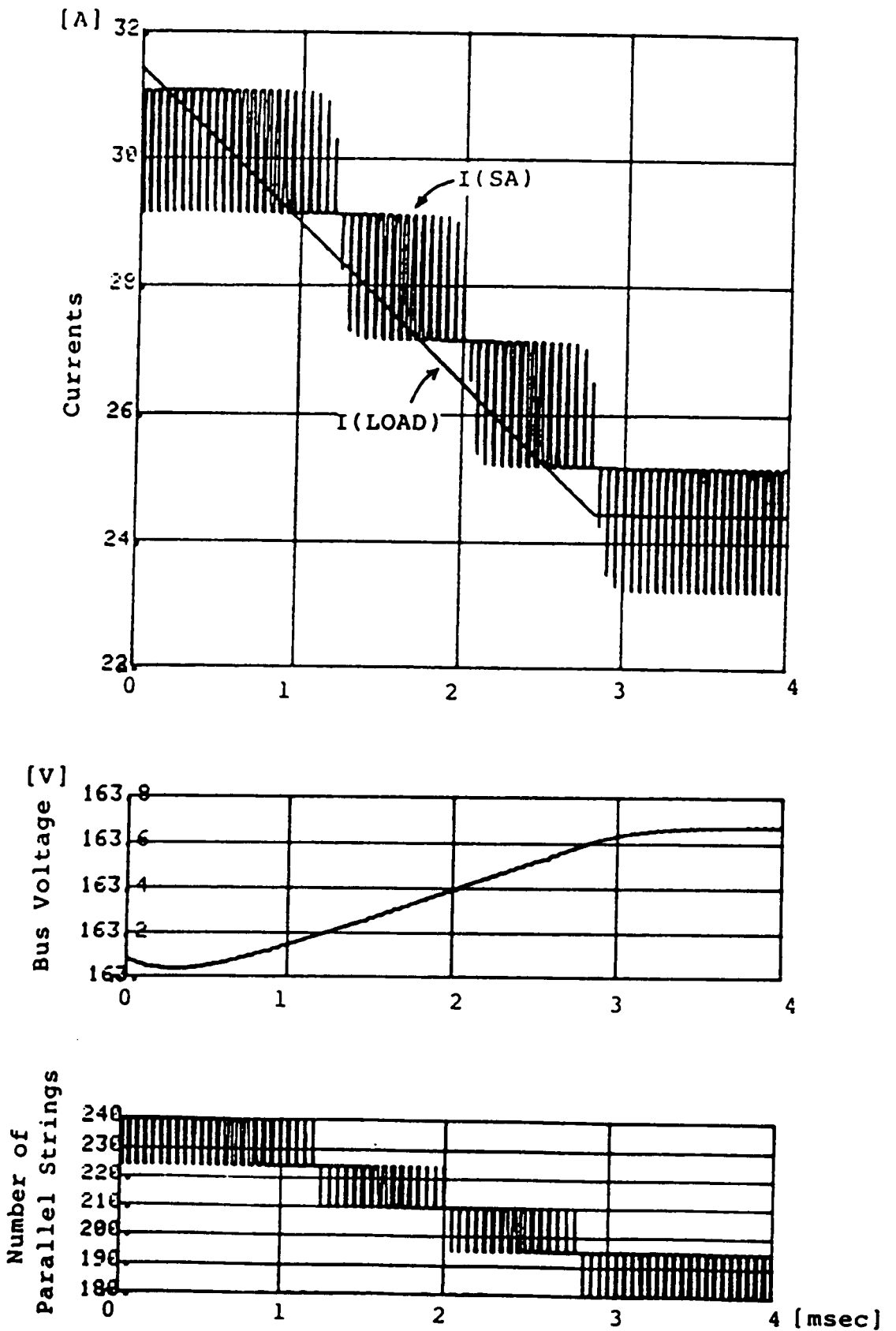**Fig. 5.6 Sequential switched shunt regulator**

Fig. 5.7 Simulation of SSSR with linear load change

the bus voltage is regulated by the SSSR in the specified voltage range of 159 - 167V.

From the beginning of the simulation, the load power linearly decreases from 5.1 kW to 4.0 kW, so the load current also decreases accordingly from 31.5 A to 24.5 A, as shown in the figure. Since the load current decreases, the bus voltage increases. The error voltage from the bus triggers the shunt switches, to shunt unnecessary sections of the solar array. The SASU output is proportional to the effective number of parallel solar array strings, n_{eff}. This number goes up and down according to the PWM signal. In a steady state, only one shunt switch is repeatedly turned on and off by the PWM signal and all the other switches are either on or off.

The shunt reference voltage is 163 V in this simulation. The bus voltage is well regulated within the specified range. Since a simple gain was used for the shunt feedback circuit, the bus voltages rises slightly as the number of shunted array sections increases. (Design considerations of the feedback compensation circuit will be discussed in the next section.)

The ripple voltage at the steady state is about 10 mV, which is very small. In this simulation, since the number of parallel strings in one section is 15 and the capacitance of the filter capacitor is 3000 μF, there are some margins either to increase the number of strings in one section or to reduce the capacitance of the filter.

From the above discussions, the SASU system with a shunt regulator provides fine regulation of bus voltage and has some thermal dissipation in the shunt regulator. The PWM SSSR system, however, provides minimum thermal dissipation and the bus voltage ripple exists due to the PWM operation.

CHAPTER 5

5.2.3 Analysis of SASU system

5.2.3.1 SASU system with a shunt regulator

For the SASU system with a shunt regulator, the small-signal dynamics of the system are exactly the same as that in the regular shunt mode, because the shunt regulator of the SASU system is always active during the sunlight period. DC regulation of the bus voltage depends on the dc gain of the shunt regulator control loop. As derived in Chapter 4, the output impedance of the system in the shunt mode becomes

$$Z_o = \frac{Z_{eq}}{1 + T} = \frac{Z_{eq}}{1 + Y_{sh}Z_{eq}} \tag{5.1}$$

One difference between this and the previous shunt system described in Chapter 4, is that the Z_{eq} varies according to the size of the effective array sections connected to the bus.

5.2.3.2 PWM-type SSSR system

For the PWM-type SSSR system, current and voltage waveforms of the system are first investigated to understand the system's operation. At a steady state, the bus voltage is regulated at V_{ref} by the PWM operation, with a feedback control as shown in Figs. 5.8a and 5.8b. Figure 5.8a represents the circuit schematic of (N+1)th section. In the figure, the number of parallel strings in one section is given by n, and I_g represents the current of one array string. The output current of one array section is defined as I_n. The actual operating point, C, is determined by the duty ratio of the shunt switch of (N+1)th section. The waveforms of the diode current, shunt switch current and bus voltage ripple are shown in Fig.
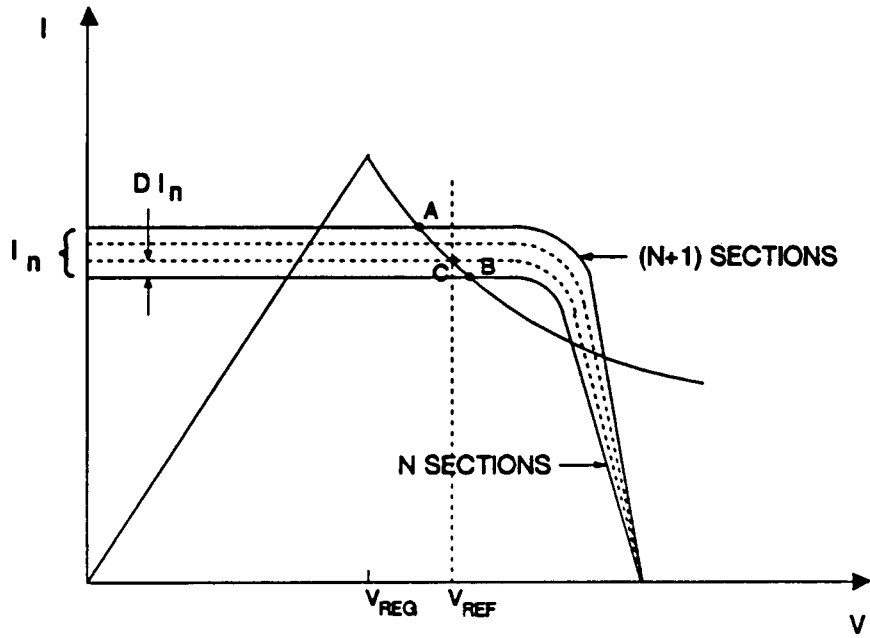
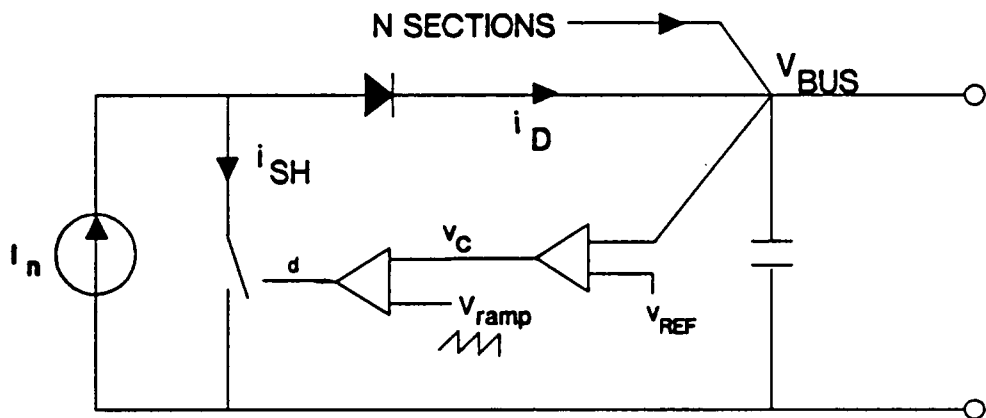Fig. 5.8a I-V characteristics of SSSR system with constant-power load

Fig. 5.8b Schematic of (N + 1)th section of SSSR

5.9. The average diode current, I_D, and shunt switch current, I_{SH}, are given by

$$I_D = D I_n \qquad (5.2)$$

$$I_{SH} = D' I_n$$

where D is the duty ratio of diode conduction and $D' = 1 - D$.

Assuming that the ESR of the filter capacitor is negligible, the output ripple voltage can be obtained from

$$\Delta V_C = \frac{1}{C} \int_{t_1}^{t_2} (I_n - I_D) \, dt = \frac{1}{C}(t_1 - t_2)(I_n - I_D) \qquad (5.3)$$

$$= \frac{1}{C} DT I_n (1 - D) = \frac{1}{C} DD' I_n T$$

From Eq. (5.3), the largest ripple occurs when the duty ratio is 0.5. Therefore,

$$\Delta V_C(\max) = \frac{1}{C} \frac{T}{4} I_n \qquad (5.4)$$

From the above equation, the capacitance of the filter capacitor can be obtained with a given ripple specification and switching frequency.

Secondly, the dynamic behavior of the system is investigated to see how the control loop stabilizes the system. When the load of the SSSR is resistive-type, the system is always open-loop stable. However, when the load is of constant-power type, it is open-loop unstable if the system operates in Region #2, as defined in Chapter 3. The regulation voltage (bus voltage) should be selected to correspond with the solar array end-
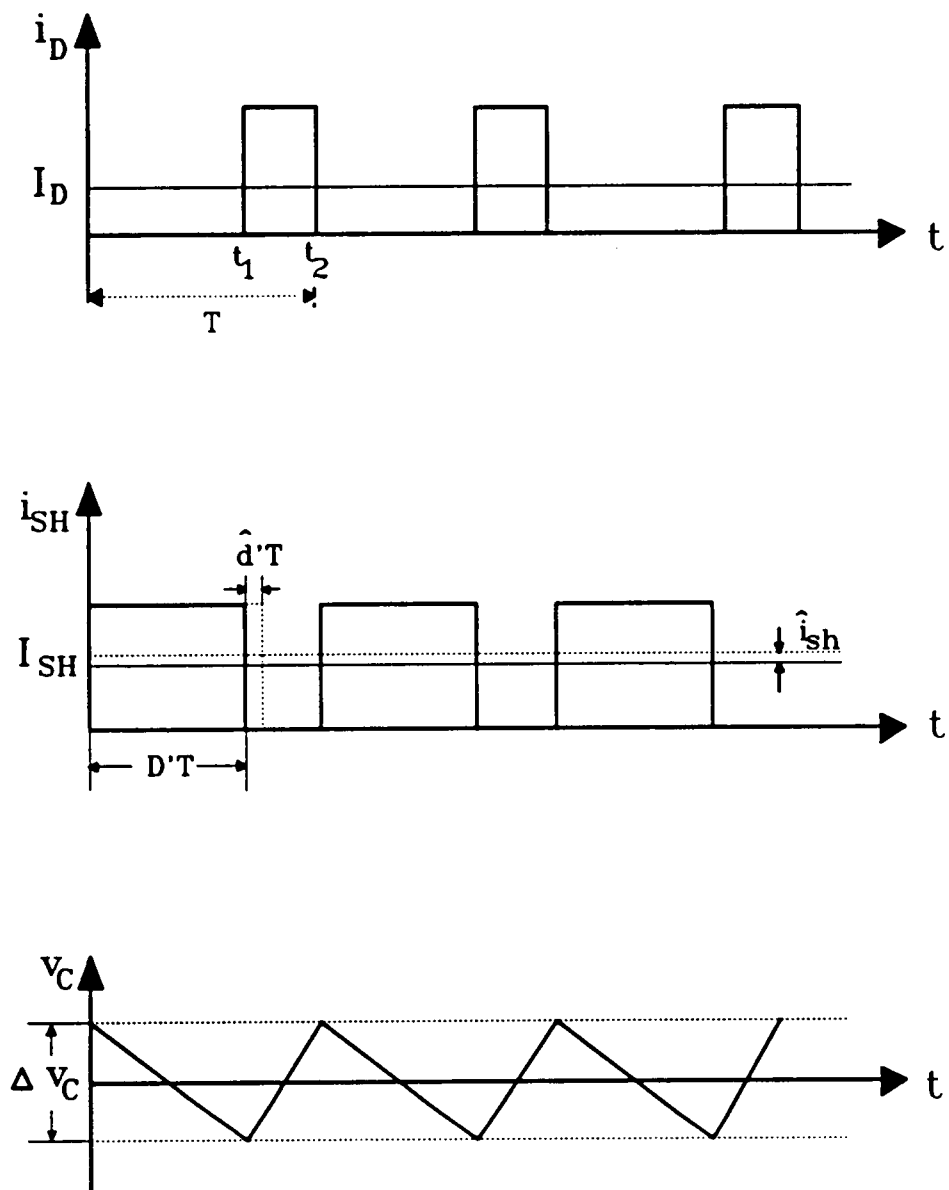
Fig. 5.9 Current and voltage waveforms of SSSR system

of-life peak-power voltage, in order to obtain high efficiency throughout the mission period, as mentioned in Chapter 3. Therefore, the system operating point should be in Region #2.

Here, in order to understand the function of the feedback circuit in the SSSR system, the stability of the system is analyzed with a simplified system, as shown in Fig. 5.10. The duty ratio of the SSSR system controls the average current from the solar array. The effect of changing the effective number of parallel strings, n_{eff}, is the same as that of changing the output current from the solar array, below the peak power voltage. As a result, the PWM operation with sequential switching can be modeled by changing the number of parallel strings of the solar array, as shown in Fig. 5.11. Unlike the previous analysis in Chapter 3, the line inductance is omitted to further simplify the system.

The circuit equation of Fig. 5.10 without the feedback circuit is derived as

$$C \frac{dv_C}{dt} = i_S - i_R \tag{5.5}$$

To investigate the dynamic characteristic of the system, the state, v_C, is perturbed at an equilibrium point, A, in Fig. 5.11. Then, the perturbed circuit equation is

$$C \frac{d}{dt} (V_C + \hat{v}_C) = I_S + \hat{i}_S - (I_R + \hat{i}_R) \tag{5.6}$$

Since the source impedance of the solar array and the impedance of constant-power load can be considered constant while one array section is switched on or off, the linearized small-signal equation becomes
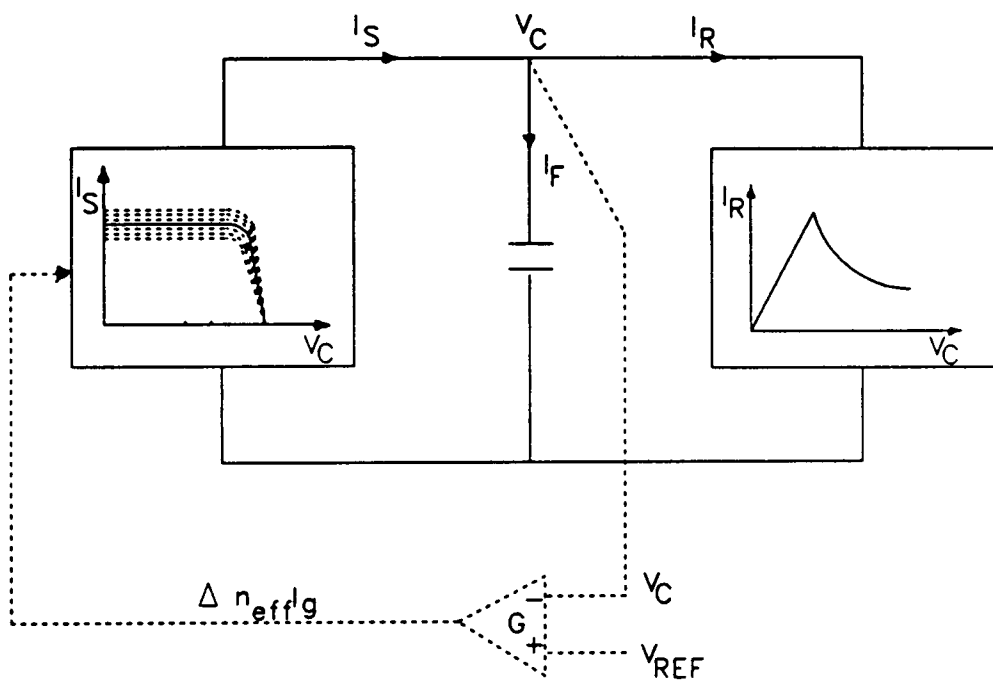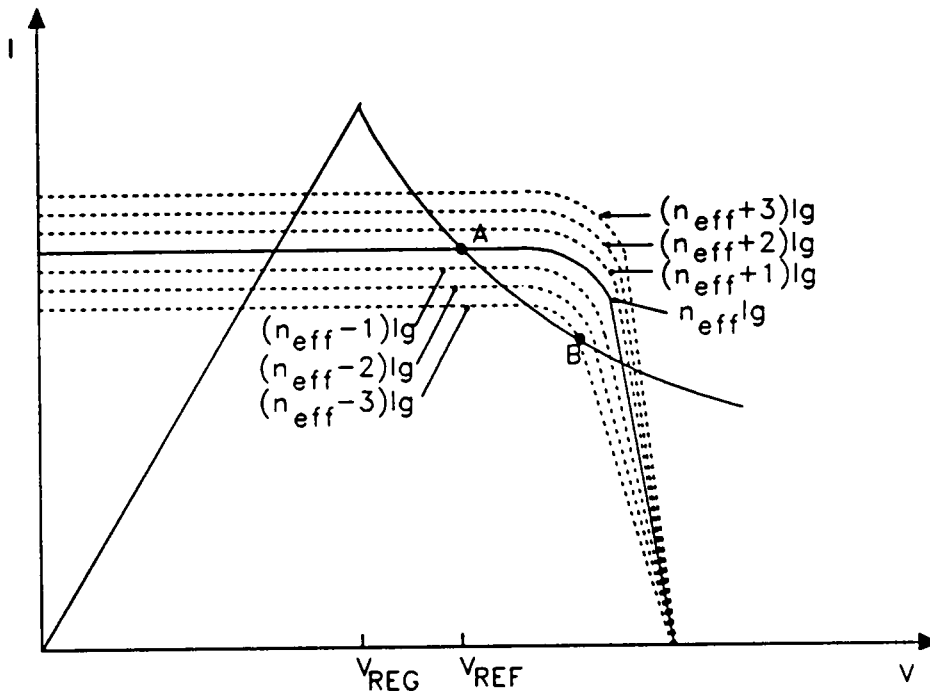
Fig. 5.10 Simplified SSSR control system

Fig. 5.11 I-V characteristics of simplified SSSR model

$$C \frac{d\hat{v}_C}{dt} = \hat{i}_S - \hat{i}_R = \left(\frac{1}{r_S} - \frac{1}{r_L} \right) \hat{v}_C \qquad (5.7)$$

where r_S and r_L are the incremental resistance of the solar array and the constant-power load, respectively, at the equilibrium point A. In Region #2, $\left(\frac{1}{r_S} - \frac{1}{r_L} \right)$ is greater than zero because $r_S < 0$, $r_L < 0$ and $|r_S| > |r_L|$. Therefore, since the system eigenvalue is positive in Eq. (5.7), the system becomes unstable.

In the SSSR system, the bus voltage is compared with a reference voltage and the difference causes the solar array output current to be changed. This control action, using the bus voltage feedback, stabilizes the system as shown with the dotted line in Fig. 5.10. The perturbed circuit equation with the feedback is

$$C \frac{d}{dt} (V_C + \hat{v}_C) = I_S + \hat{i}_S - g(V_C + \hat{v}_C - V_{REF}) - (I_R + \hat{i}_R) \qquad (5.8)$$

If there is no steady state error in this system, V_C is the same as the reference voltage, V_R and I_S is equal to I_R. Therefore, the linearized small-signal equation is

$$C \frac{d\hat{v}_C}{dt} = \hat{i}_S - g\hat{v}_C - \hat{i}_R = \left(\frac{1}{r_S} - g - \frac{1}{r_L} \right) \hat{v}_C \qquad (5.9)$$

From Eq. (5.9), one can notice that the feedback works like a shunt regulator in the solar array power system having a shunt regulator. Actually, the feedback term, $g\hat{v}_C$, is implemented by changing the duty ratio of the shunt switch or the number of parallel strings in various solar array switching systems.

If g in Eq. (5.9) is chosen to be larger than $\left| \dfrac{1}{r_S} - \dfrac{1}{r_L} \right|$, the system becomes stable.

In this SSSR system, the feedback term, $g\hat{v}_C$, has the same role as the shunt current of the shunt regulator. That is, this term represents the current subtracted from the source current according to the bus voltage error. This current is either shunted in the solar array panel or disconnected from the solar array bus, while in a shunt regulator system this current is dissipated in the shunt circuit. The source current change can be expressed as

$$g\,\hat{v}_C = \hat{n}_{eff}\,I_g \qquad \hat{n}_{eff} = \frac{g}{I_g}\,\hat{v}_C = \frac{g}{0.14}\,\hat{v}_C \tag{5.10}$$

where I_g is assumed to be 0.14 ampere. Then,

$$\Delta n_{eff} = G\,(v_C - v_{REF}) \tag{5.11}$$

From Eq. (5.11), the gain, G ($= g/0.14$), can be used for designing the feedback gain of the system.

Computer simulations are performed to verify the analysis. A system consisting of the SASU and constant-power load, together with a capacitor voltage feedback, is modeled and simulated. In this simulation, the effective number of parallel strings changes continuously instead of discretely to match with the small-signal assumption. In this simulation, the bus voltage reference is chosen as 28V, which is commonly used in spacecraft power systems. At the equilibrium point in Region #2 of this simulation example, r_S is -34.4 and r_L is -0.64. Therefore, g should be greater than approximately 1.6 to make the system stable. When the feedback gain, g, is chosen as a value larger than 2, the system is stable, as shown in Fig. 5.12. The operating point stays at point A in Region #2, as shown
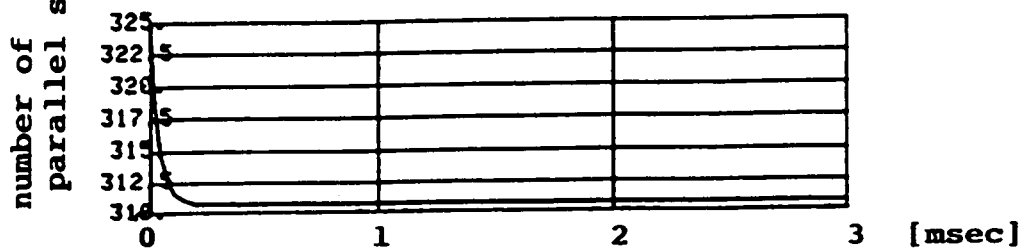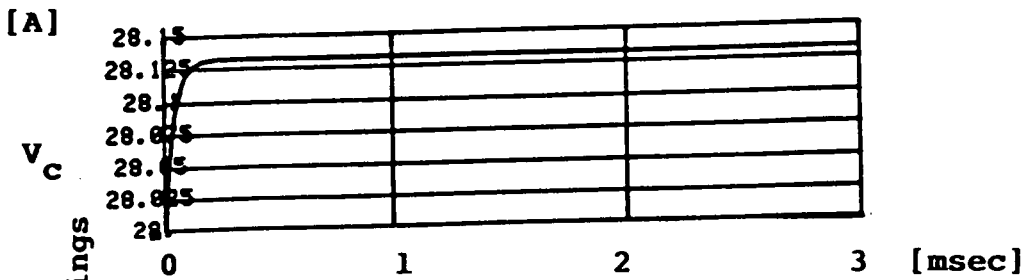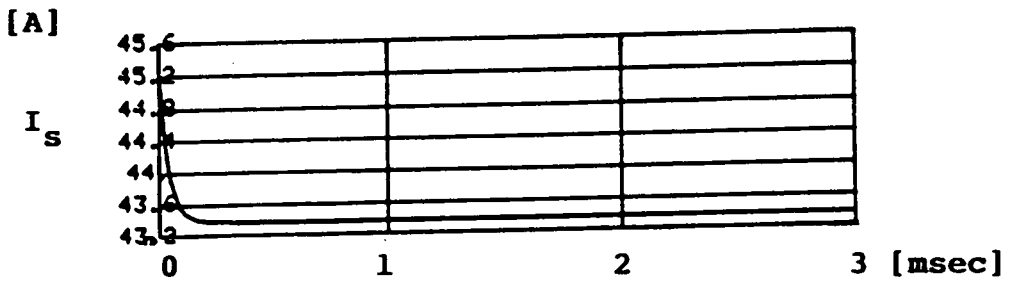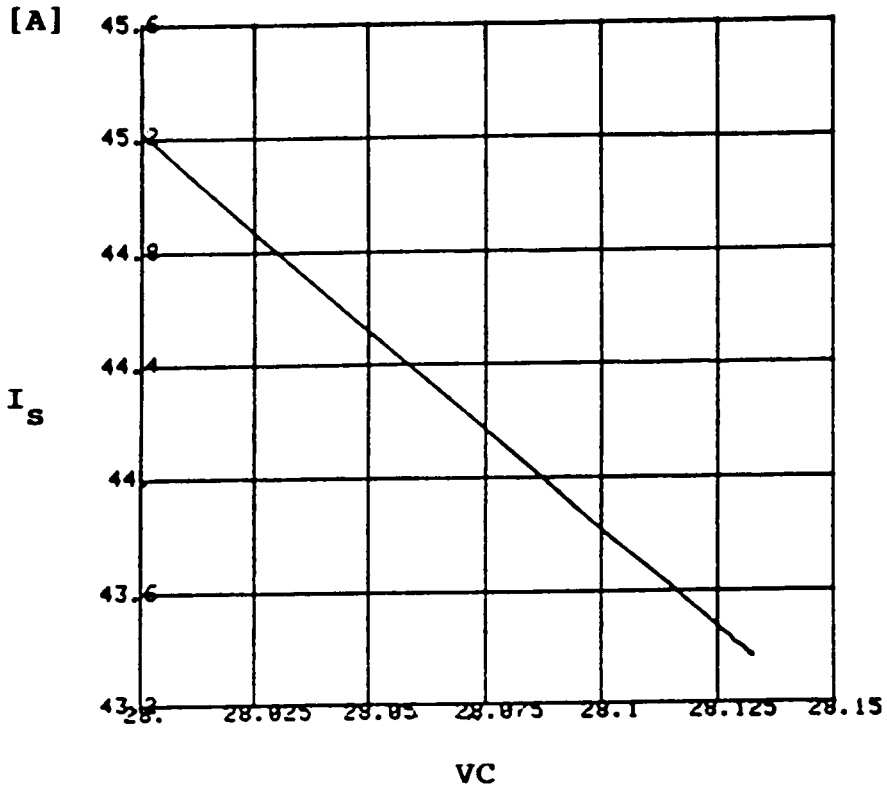
Fig. 5.12 Simulation of the stable case ($g = 14$)

in Fig. 5.11. However, when a gain, g, of less than 1.6 is used, the system becomes unstable, as shown in Fig. 5.13. The bus voltage is settled at 41.7V, which corresponds to point B in Region #3 in Fig. 5.11. The bus voltage is not regulated in this case. The number of parallel arrays becomes smaller than that of the stable case, because the operating point moves to point B.

From the above analysis and simulation, it is shown that the feedback circuit of the solar array switching system works as a shunt regulator. As a result, a small-signal control block diagram of the system can be drawn, as shown in Fig. 5.14. From Eq. (5.2), the gain of the transfer function from the duty ratio to the shunt switch current becomes

$$\frac{\hat{i}_{sh}}{\hat{d'}} = I_n \tag{5.12}$$

In the figure, H_v is a transfer function of the error amplifier circuit and FM is a PWM gain. The transadmittance from the bus voltage error to the shunt switch current is

$$Y_{sh} = H_v FM I_n \tag{5.13}$$

Y_{sh} must be designed with the same criteria as for the shunt regulator described in Chapter 4. Therefore, the system's loop gain, T, and the output impedance can be derived as

$$T = H_v FM I_n Z_{eq} = Y_{sh} Z_{eq} \tag{5.14}$$

$$Z_o = \frac{Z_{eq}}{1 + T} \tag{5.15}$$
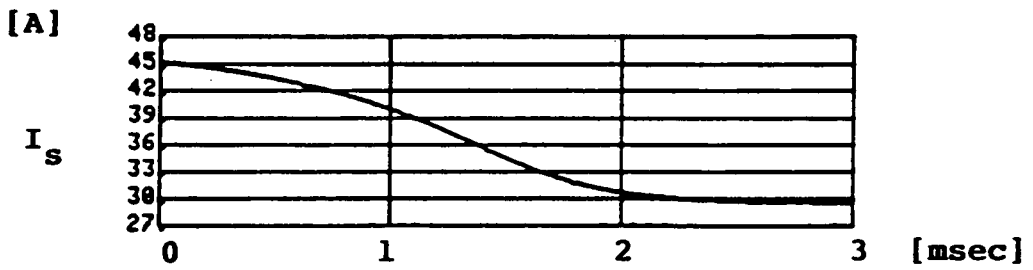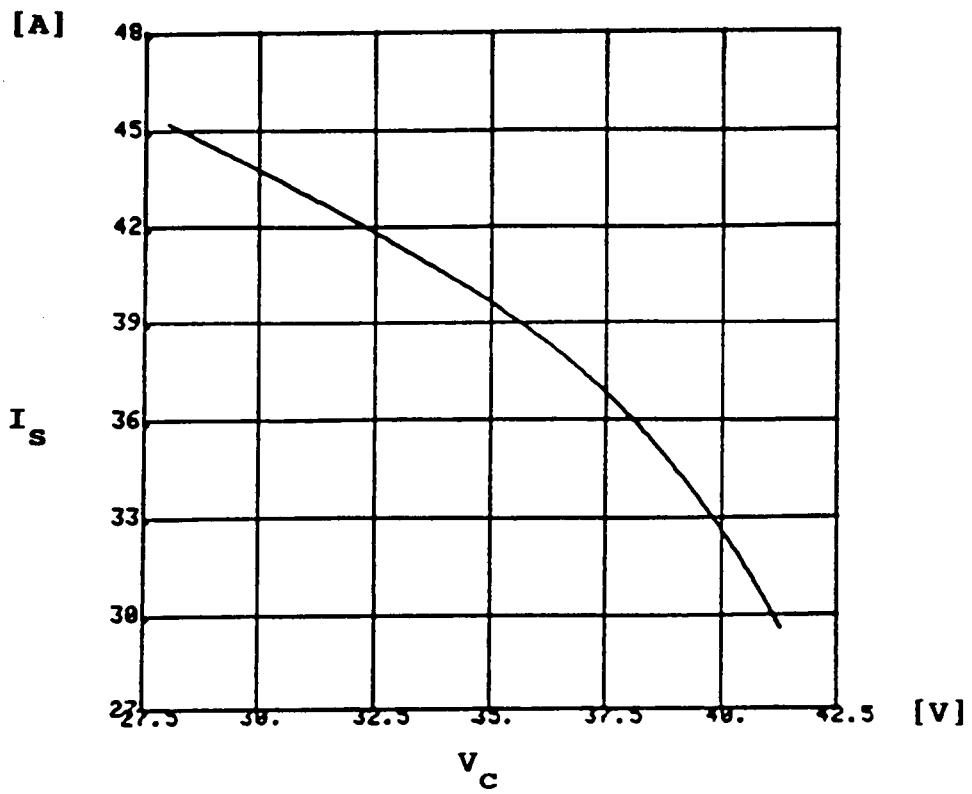
Fig. 5.13 Simulation of the unstable case ($g = 1.4$)
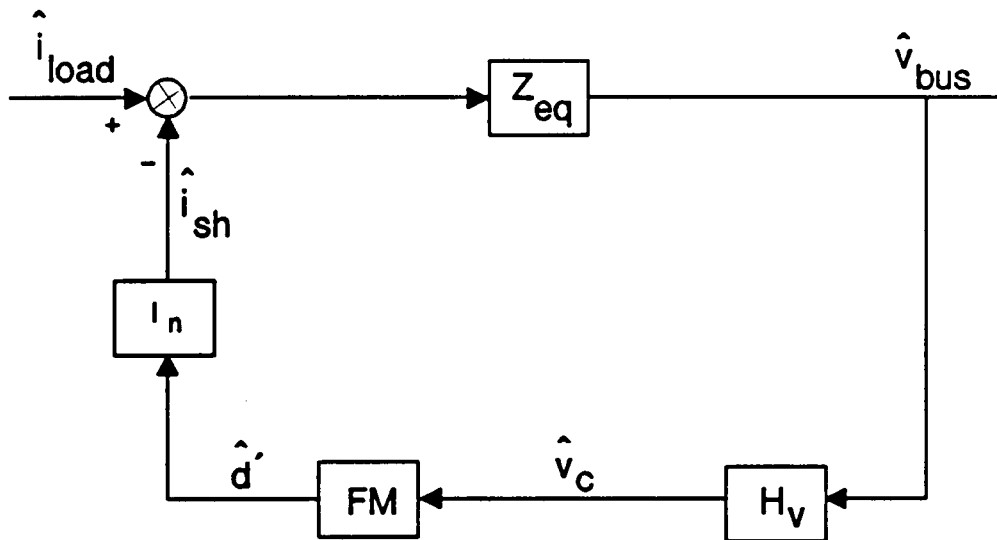
Fig. 5.14 Small-signal control block diagram of SSSR system

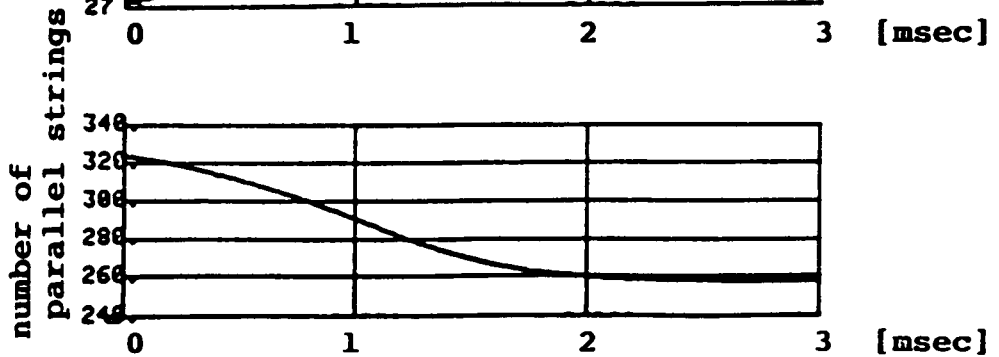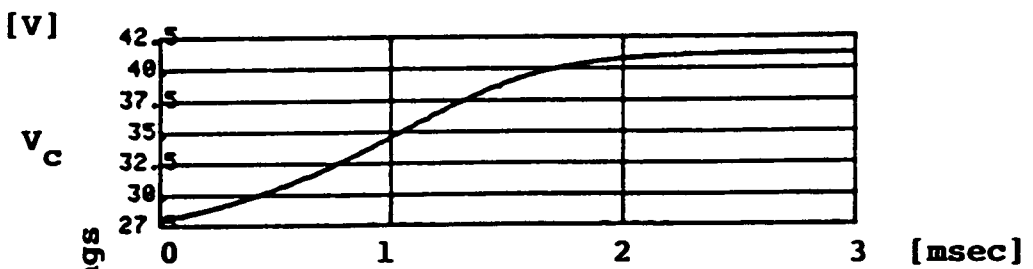where Z_{eq} is the source impedance of the solar array sections with the shunt switches fully off, in parallel with the bus filter defined in Chapter 4.

5.3 Partially-Shunted Solar Array System

5.3.1 Introduction

Another way to reduce the heat dissipation in the shunt circuit is the use of the partial shunt system. The partial-shunt regulator reduces the peak power dissipation to 30-50% of the amount dissipated in a functionally equivalent full shunt [25].

As in a full shunt, there is a control circuit which performs the same basic function, and there are sections intended to dissipate the excess power and regulate the bus voltage. In a partial-shunt system, the power sections are placed across only part of the total number of series-connected solar cells. Thus, the shunt circuit is used to absorb part of the output of the solar array. The design of a partial shunt is greatly dependent on the type of solar cells used, the degradation encountered and the temperature extremes to which the cells are subjected in orbital flight.

As shown in Fig. 5.15, the total number of series solar cells is expressed as

$$N_S = N_U + N_L \qquad (5.16)$$

where N_U = the number of upper series cells

N_L = the number of lower series cells

The number of series cells, N_s, is selected to be able to deliver a given fixed array's output voltage, V_{bus}, to be the shunt reference voltage, V_{ref}, throughout the life of the system. Thus,

$$N_S d_v V_{pp} = V_{ref} \qquad (5.17)$$

where V_{pp} is a peak power voltage of one cell, and d_v is a voltage degradation factor equal to the ratio of the end-of-life to beginning-of-life

CHAPTER 5
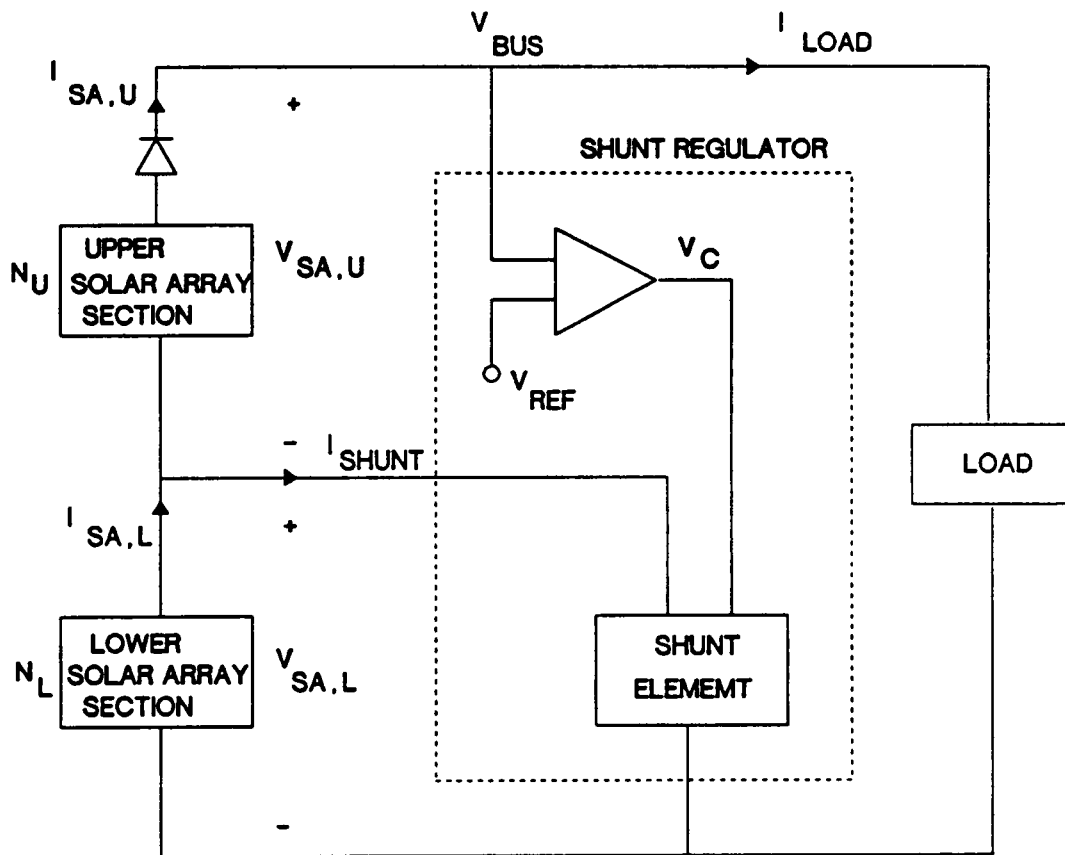
Fig. 5.15 Partial-shunt configuration

voltage at the array's peak-power point, and at a steady-state array temperature. That is, the serial cells of a solar array should be designed so that the peak-power voltage at the end-of-life can be equal to the desired bus reference voltage. The output power of the solar array can then be used most efficiently throughout the life of the system.

In a partial-shunt configuration, the array is electrically split into two sections: upper and lower. The partial-shunt element is placed across a part of the total number of series cells defined by the fraction m:

$$m = \frac{N_L}{N_L + N_U}$$ (5.18)

When the shunt transistor is saturated, that is, when the voltage across the lower cells, $V_{SA,L}$, becomes zero, the highest possible voltage which the upper bank of N_U cells can deliver must not exceed V_{ref} in order to regulate the bus voltage under all conditions. The saturation of the shunt transistor will occur when the array is completely unloaded and the solar cells are at their lowest temperature, at the beginning-of-life. Therefore,

$$N_U V_{oc}(\max) < V_{ref}$$ (5.19)

where $V_{oc}(\max)$ is the maximum open circuit voltage of one cell. By substituting Eqs. (5.16), (5.17) and (5.18) into equation (5.19),

$$m > 1 - \frac{d_v V_{pp}}{V_{oc}(\max)}$$ (5.20)

Thus, the location of the array tap-off point is dependent on the values of d_v, V_{pp} and $V_{oc}(\max)$.

5.3.2 Model generation and simulation

For the partial-shunt configuration, as shown in Fig. 5.16, another solar array model has been developed to provide the tap-off point of the solar array for the shunt regulator. The control voltage, V_c, as shown in Fig. 5.15, is generated by sensing the main bus voltage to control the shunt current. In this model, two solar array models are connected in series. The shunt current controls the low solar array output voltage, thus regulating the bus voltage. The output current of the upper solar array is equal to the inductor current, I_1, where L represents the line inductance. The output current of the lower solar array is the sum of the shunt current and the inductor current. From the given I_1, V_{o1} is obtained from the solar array I-V equation. Then,

$$I_2 = I_1 + I_{sh} \qquad (5.21)$$

$$L \frac{dI_1}{dt} = V_{o1} + V_{o2} - I_1 R - V_C$$

$$C \frac{dV_B}{dt} = I_1 - I_{LOAD}$$

The partial-shunt system with a constant-power load, as shown in Fig. 5.16, is modeled and simulated.

As shown in Fig. 5.17, the load power decreases at a certain rate from the beginning of simulation. The bus voltage increases accordingly and becomes greater than V_{ref} (28.14V in this simulation), which causes the shunt current to flow. As shown in Fig. 5.15, the upper solar array carries only the load current and the lower solar array carries both the load current and shunt current. Since the load current continues to decrease, the upper solar array output voltage increases. The lower array current (the sum of the load and shunt currents) increases so that the lower solar
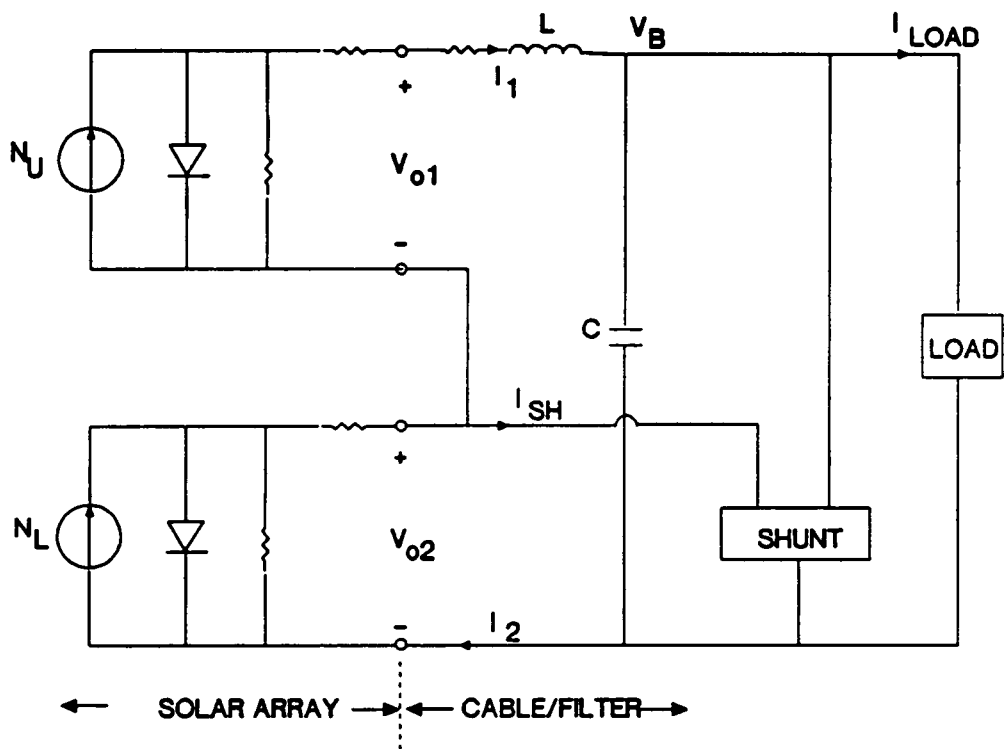
Fig. 5.16 Circuit model of partially-shunted solar array
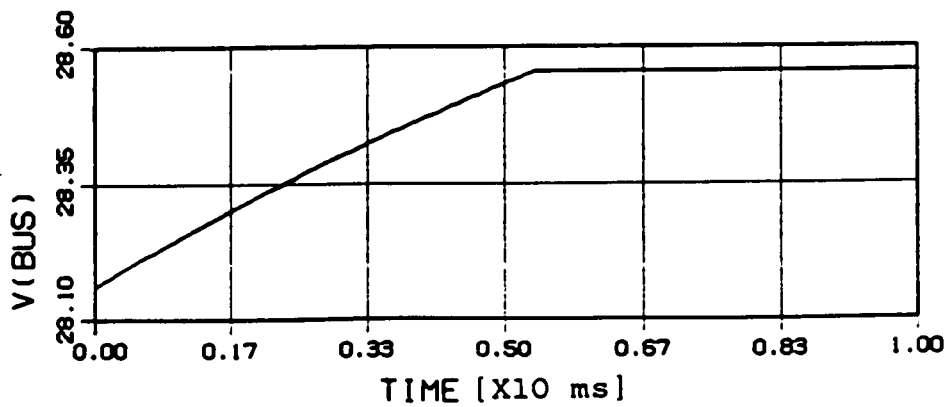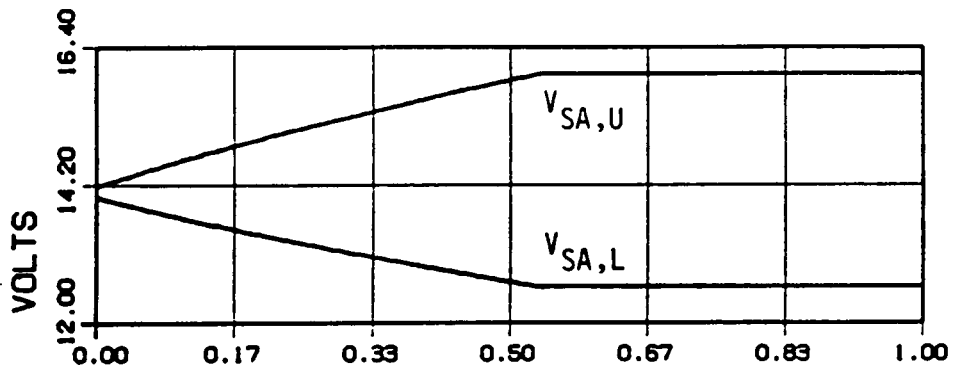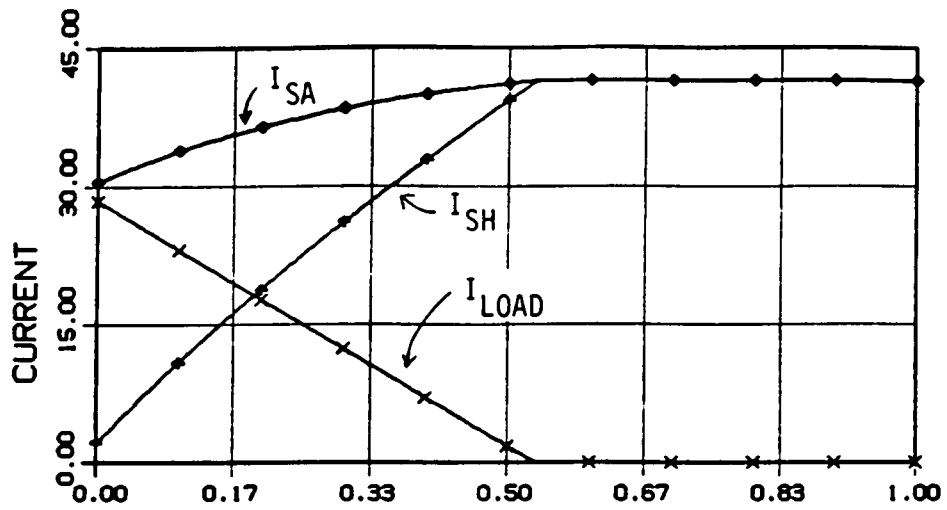
Fig. 5.17 Simulation of partial-shunt system

array output voltage decreases. The sum of lower and upper solar array voltages becomes the bus voltage. The steady-state error of the bus voltage depends on the dc gain of the shunt regulator.

5.3.3 Analysis of power dissipation

As mentioned in the previous section, the main purpose of using the partial shunt system is to reduce the power dissipation in the shunt circuit. Comparison of the power dissipation between the full shunt and the partial shunt are illustrated in Fig. 5.18.

As shown in Fig. 5.18, the power dissipation in the full shunt regulator with a no load condition becomes

$$P_{diss} = I_{SH} V_{RS} \text{ [W]} \tag{5.22}$$

where I_{SH} is the shunt current and V_{RS} is the regulated bus voltage. Let us assume that the same size of solar array used for the full-shunt is tapped at the center of the serial cells to make the partial-shunt system. Then, since there is no load, the operating point of the upper array becomes Point A, which is in open-circuit condition. The operating point of the lower array is determined by the voltage difference between V_{RS} and $V_{SA,U}$. Since the I_{SH} in the full-shunt case (Fig. 5.18a) is almost the same as $I_{SH,L}$ in the partial shunt (Fig. 5.18c), total dissipation in the partial-shunt system becomes

$$P_{diss} = I_{SH} V_{SA,L} \tag{5.23}$$

From the previous simulation result, the power dissipation of the full-shunt case is about 42 x 28.5 = 1197 watts, while the dissipation in the partial shunt is about 42 x 12.6 = 529.2 watts.
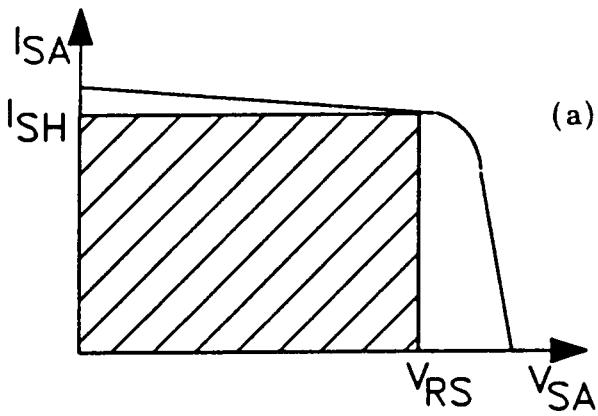
FULL SHUNT CASE
58 CELLS IN SERIES
PEAK POWER DISSIPATION
$= I_{SH} \times V_{RS}$ [W]

(a)
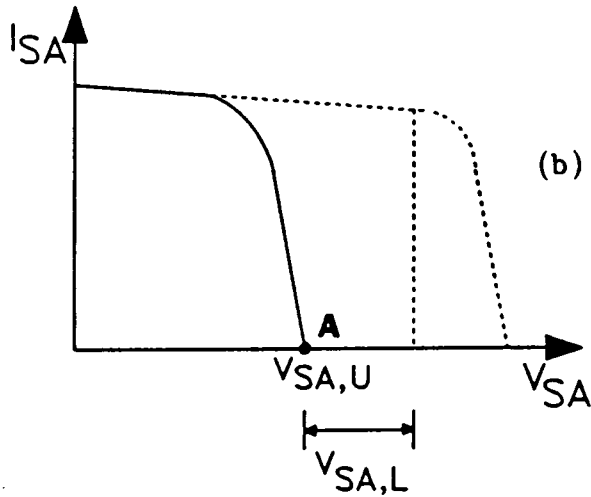
UPPER SOLAR ARRAY
28 CELLS IN SERIES
NO POWER DISSIPATION

(b)
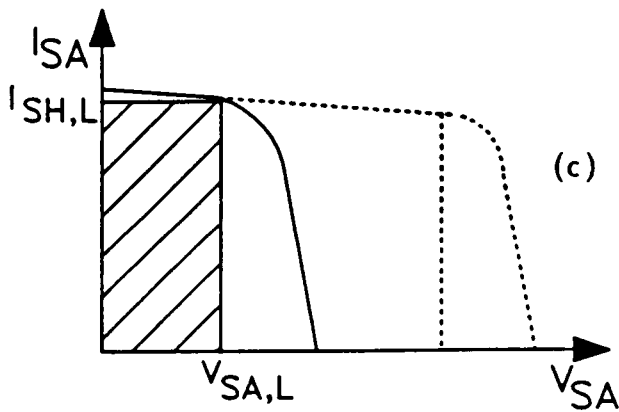
LOWER SOLAR ARRAY
28 CELLS IN SERIES
PEAK POWER DISSIPATION
$= I_{SH,L} \times V_{SA,L}$ [W]

(c)

Fig. 5.18 Peak power dissipation of partial shunt system

5.3.4 Output impedance of partial shunt system

A small-signal equivalent block diagram of the partial-shunt system is shown in Fig. 5.19. To derive the output impedance equation, the circuit equations are written as

$$v_B = v_{SA,U} + v_{SA,L} \tag{5.24}$$

$$i_B = i_{SA,U} - \frac{v_B}{Z_C}$$

$$i_{SA,U} = i_{SA,L} - i_{sh}$$

$$i_{sh} = v_B Y_{sh}$$

$$v_{SA,L} = -i_{SA,L} Z_{SA,L}$$

$$v_{SA,U} = -i_{SA,U} Z_{SA,U}$$

where Z_{SA} and Z_C are the output impedance of the solar array and the impedance of the filter capacitor, respectively, as described in Chapter 4. The output impedance for the partially-shunted solar array system shown in Fig. 5.19 is derived as

$$Z_o = \frac{Z_{SA1} + Z_{SA2}}{1 + \dfrac{Z_{SA1} + Z_{SA2}}{Z_C} + Y_{sh} Z_{SA1}} \tag{5.25}$$

Thus, design of the system loop gain is not as straightforward as in Eq. (4.6). However, if the upper and lower arrays are designed such that $|Z_{SA1}| >> |Z_{SA2}|$ (which is a typical design so that the voltage across the upper array, V_2, is less sensitive and the voltage across the lower array, V_1, is more sensitive to changes in the bus voltage, thus shunt current, to provide better control), then
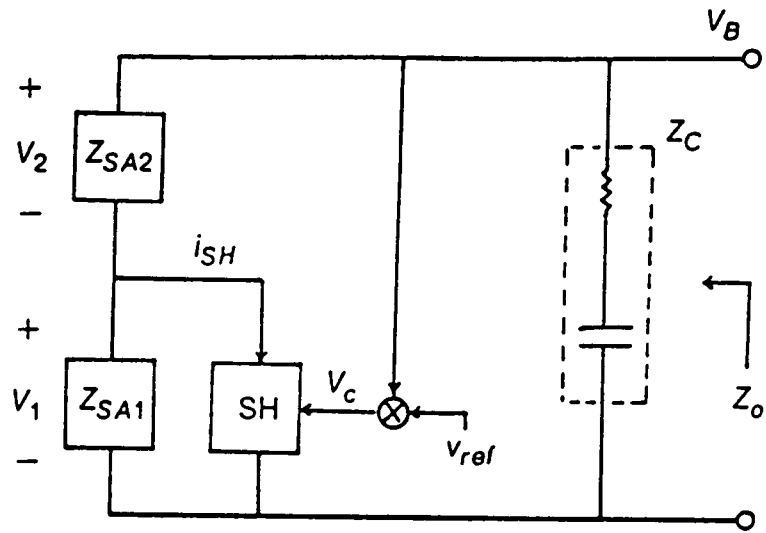
Fig. 5.19 Small-signal block diagram of partial shunt system

$$Z_o \cong \frac{Z_{SA1}}{1 + Z_{SA1} \left(\dfrac{1}{Z_C} + Y_{sh} \right)} \tag{5.26}$$

$$T_o \cong Z_{SA1} \left(\frac{1}{Z_C} + Y_{sh} \right) \tag{5.27}$$

From this simplified expression in Eq. (5.27), the system loop gain can be properly designed and the output impedance of the system can be optimized.

5.4 Peak-Power-Tracking Solar Array System

5.4.1 Introduction

The solar array peak power tracker (PPT) has been developed for spacecraft power systems and terrestrial power systems to utilize maximum power from a given solar array.

For spacecraft applications, the solar array is usually oversized, to compensate for its degradation at the end of its lifetime. Also, when the spacecraft exits eclipses, the peak output power of a solar array becomes almost two times higher than its peak output power in normal sunlight periods. As a result, the spacecraft power system should dissipate high excess power through shunt regulators at the beginning of mission and after eclipse periods. To avoid the high dissipation at the beginning of mission and to utilize maximum power after eclipse periods, the peak power tracker was widely used in many recent spacecraft. This is particularly useful for the spacecraft in a low-earth orbit because it goes through a large number of eclipses, e.g. about 15 eclipses/24 hours. A typical peak power profile generated by the solar array in the LEO spacecraft is shown in Fig. 5.20 [26, 27], together with a temperature profile.

5.4.2 System Operation

The basic concept of the PPT is to obtain maximum power from the solar array by intentionally locating the operating point at the solar array's peak power point, whenever necessary. In case of a resistive load and constant-power load, the maximum power can be achieved by impedance matching between the source and load. The slope of the solar array I-V curve is identical to the slope of the constant-power load line at the peak power point. For the constant-power load, since the partial derivative
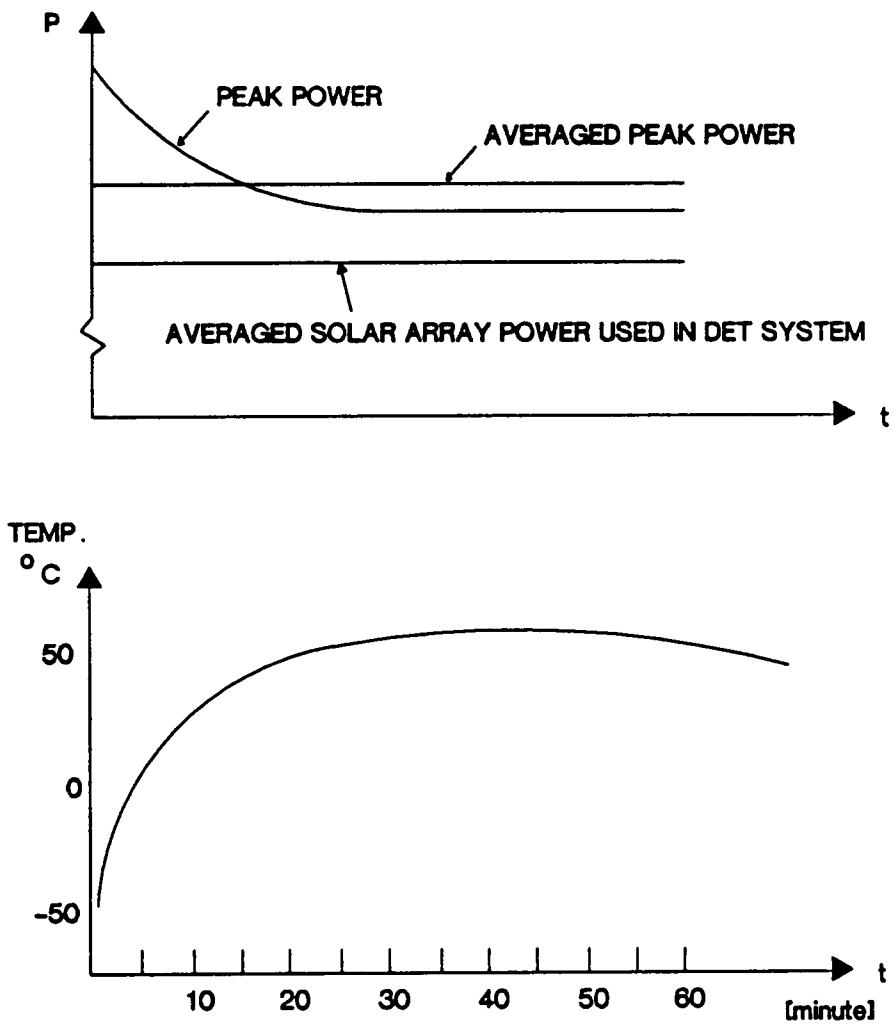
Fig. 5.20 Solar array's power and temperature profile after eclipse

with respect to the voltage or current is zero, the following equations are derived [11]:

$$P = IV \qquad \frac{\partial P}{\partial V} = I\frac{\partial V}{\partial V} + V\frac{\partial I}{\partial V} = 0 \qquad (5.28)$$

$$I = -V\frac{\partial I}{\partial V} \qquad \frac{V}{I} = -\frac{\partial V}{\partial I}$$

Therefore, the slope of the static load line is equal to the magnitude of the solar array's incremental resistance (dynamic resistance) at the peak power point.

In Figs. 5.21 and 5.22, the concept of the PPT is clearly illustrated, assuming that the PPT system is connected with a resistive load, R_L. The PPT usually utilizes a PWM-type converter. The major objective of the converter is to locate the solar array's operating point at the peak power point by controlling its duty ratio. Actually, moving the solar array's operating point to the peak power point has the same effect as matching the converter's dc input impedance (R_{in}) with the source impedance (R_{SA}) at the solar array's peak power point. The desired input impedance of the converter (PPT) can be obtained by changing the duty ratio of the converter. The average power delivered to R_L from the source is the same as the output power consumed at the load resistance, if the converter is assumed lossless [26]. Then,

$$P_S = I_S V_S = \frac{V_S^2}{R_{in}} \qquad (5.29)$$

$$P_O = \frac{V_O^2}{R_L} \qquad (5.30)$$

Defining the voltage gain of the converter,

$$\frac{V_O}{V_S} \cong M$$

BUCK POWER STAGE
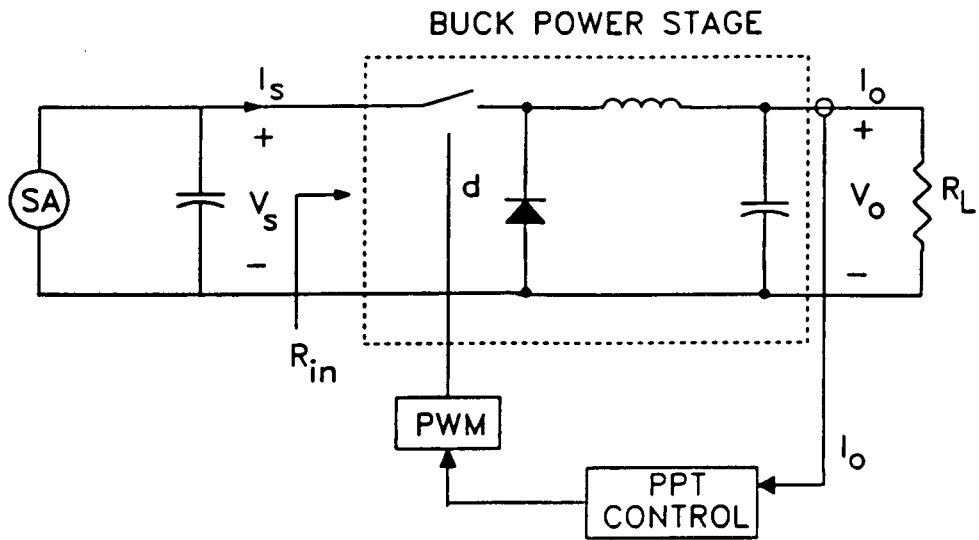
Fig. 5.21 Schematic of buck-type peak-power tracker
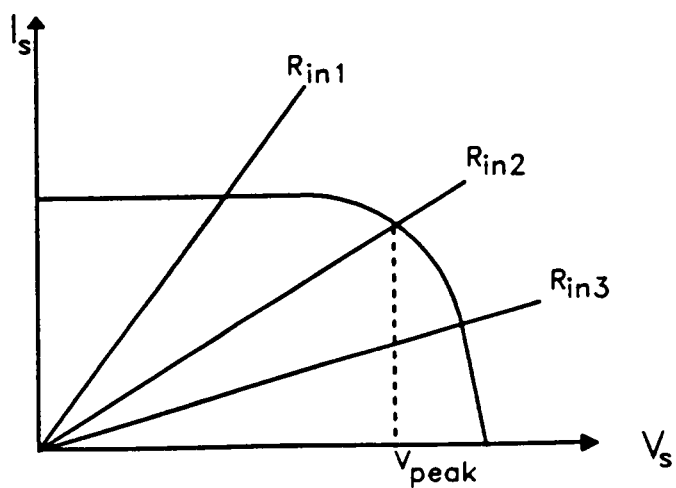
Fig. 5.22 Effect of changing reflected load line

since the $P_S = P_O$, the input resistance, R_{in}, becomes

$$R_{in} = (\frac{1}{M})^2 R_L \qquad (5.31)$$

Since the voltage gain of converter can be controlled by the duty ratio, the input resistance, R_{in}, is also controlled by the duty ratio. For the resistive load case, the duty ratio is adjusted in a direction to produce larger output current, because the output power is proportional to the output current. For a constant-power load, the product of current and voltage should be monitored to control the duty ratio.

In practical systems, the load of PPT during the sunlight period consists of a storage battery and load converters in the battery-charge mode, as shown in Fig. 5.23. The battery load can be represented as a very small resistance with a dc source. In this case, the output power is also proportional to the output current because the output voltage, that is, the battery voltage, can be considered constant due to a much larger time constant compared with the PWM operation. Controlling the duty ratio has the effect of changing the reflected battery voltage, the input voltage of the converter, to match with the peak-power voltage of the solar array. Since the output voltage of PPT is the same as the battery terminal voltage, the reflected input voltage of PPT, V_S , becomes $\frac{V_{BA}}{d}$ in the buck-type PPT. When the duty ratio of PPT is equal to 1, the input voltage, V_S, is the same as the battery voltage, V_{BA}. To track the peak power point, the duty ratio should be decreased until the reflected input voltage of PPT, V_S, is equal to the peak-power voltage of the solar array. Therefore, the reflected load line of the battery moves from L1 to L2 for the buck-type PPT, while it moves from L3 to L2 for the boost-type PPT.

After the battery is fully charged, the PPT is deactivated and the solar array sees only the constant-power load without the battery. Then, the

BOOST : $V_s = d'V_{BA}$ $V_s = V_{BA}$

BUCK : $V_s = V_{BA}$ $V_s = \dfrac{V_{BA}}{d}$

L1

L2   L3

REFLECTED
LOAD LINE
OF BATTERY

A

V_{peak}

V

I
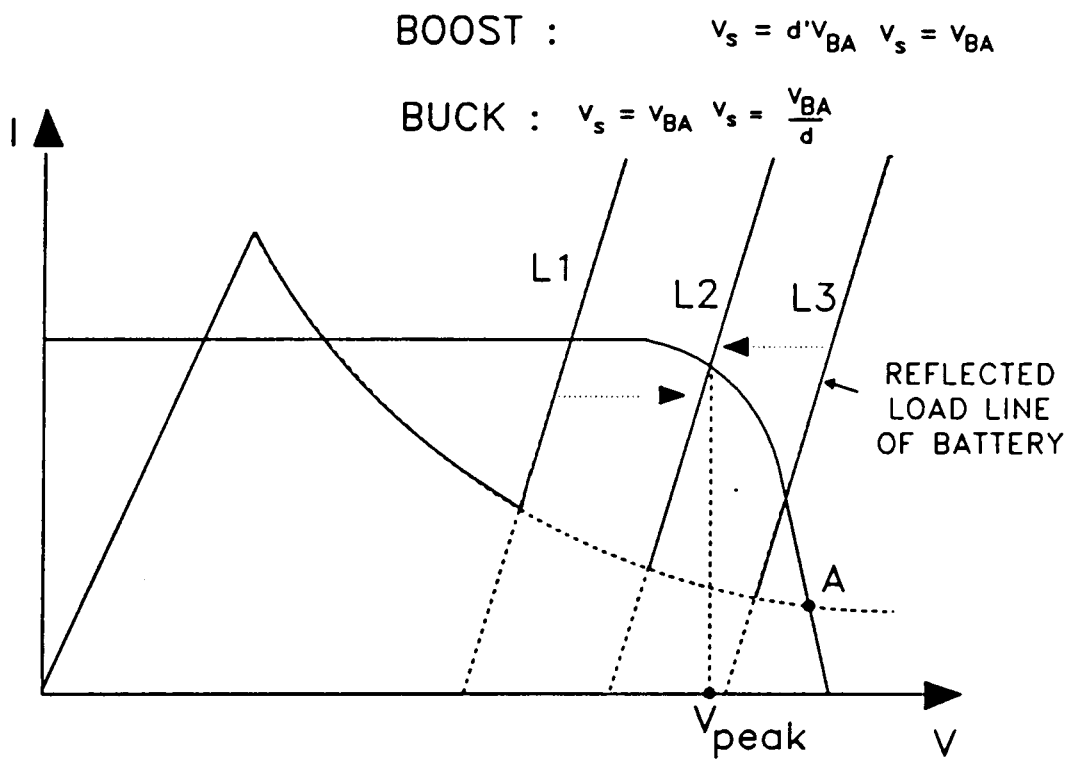
Fig. 5.23 I-V characteristics of battery load and
constant-power load in PPT system

185

operating point moves to point A; that is, it moves towards the open circuit voltage of the solar array.

5.5 Simulation of COBE Power System

5.5.1 Introduction

An existing spacecraft power system, the COBE power system being built by NASA-Goddard, shown in Fig. 5.24, has been modeled and simulated using an already-developed macro component model library. Various systems' modes of operation, including transition modes, are simulated. A simulation is also performed for a complete mission orbit cycle using dc models for the power conditioning equipment and battery.

The COBE power system is basically a DET system. The various power-conditioning components are activated only as needed, thus requiring the system to process only the amount of power needed to maintain the bus at the specified voltage level. A system's mode of operation is determined by the power system central control unit (CCU). The control unit continuously monitors appropriate signals to activate the power conditioning equipment. The control unit provides signals that control the disposition of solar array, battery and shunt currents to maintain the bus voltage regulation. When the bus voltage exceeds the specified level, the control signal activates the shunt regulator, and the excessive solar array power is absorbed by the shunt elements. In this mode, the solar array also supplies the charging current to the battery if it is necessary. When the bus voltage becomes less than the specified level, the battery discharger is activated and the load power is supplied by the solar array and the battery in shared mode. The battery-discharging current is controlled by the bus voltage.

In this simulation, the switching regulators and resistive load were modeled as a constant-power load.
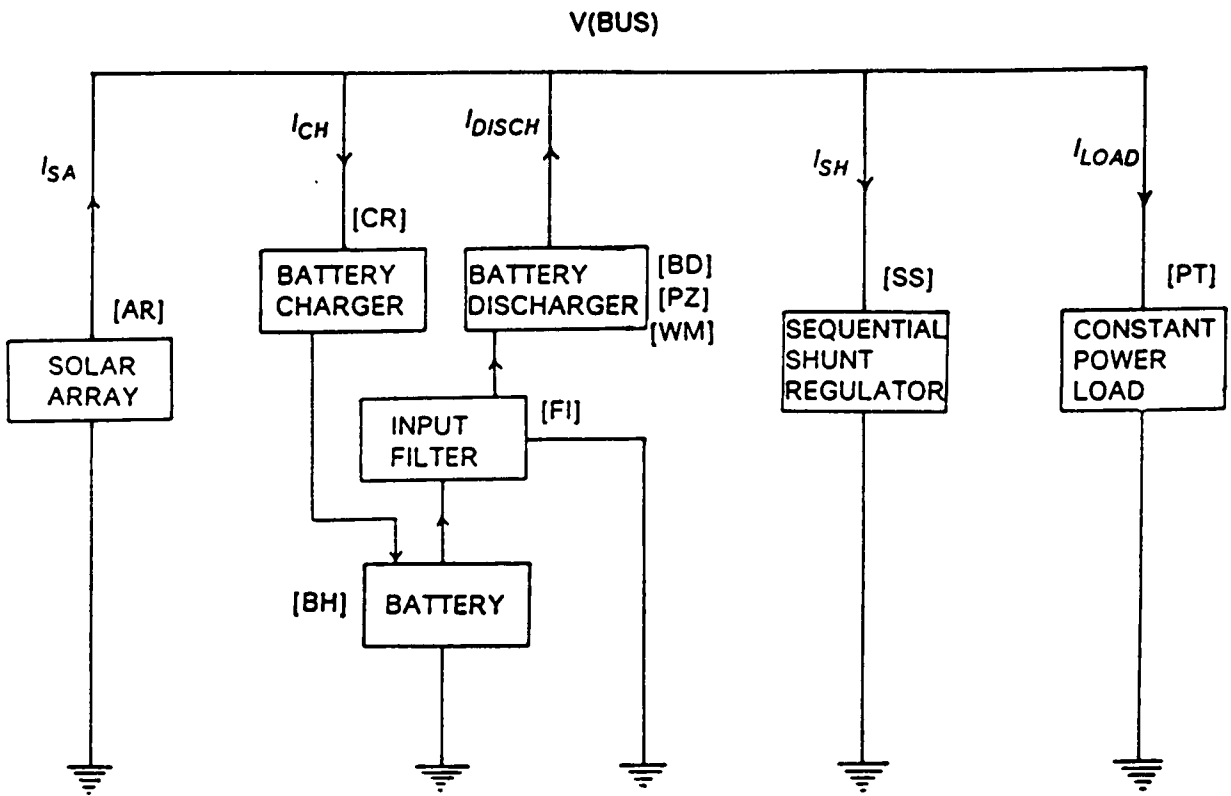
Fig. 5.24 COBE power system block diagram

5.5.2 Transient Simulations

The solar array model [AR] is connected with a battery-charger model [BH], battery-discharger model (power stage of battery discharger [BD], two-pole two-zero compensator [PZ] and PWM [WM]), a sequential shunt regulator model [SS] and a constant-power load model [PT]. The battery charger model is a series pass charger modeled in Chapter 2. The battery-discharger model developed in [2], is a buck-type converter which uses an auto-transformer to boost up the voltage and an output voltage feedback compensator. The sequential shunt regulator model is also developed in Chapter 2. A battery model [BH] is connected to the battery-charger and input filter [FI] of the battery-discharger.

The mode of operation changes from one mode to another as either the illumination level changes or the payload varies. The CCU continuously monitors the bus voltage and commands the system to operate in the battery-discharge mode when V_{bus} becomes less than the battery-discharger regulation voltage (V_{RBD}), or in the shunt-active mode when V_{bus} exceeds the shunt regulation voltage (V_{RS}). When V_{bus} is between V_{RBD} and V_{RS}, a dead band exists in which the load power is equal to the solar array's output power.

Figure 5.25 shows a change from the battery-discharge mode to the battery-charge mode due to a change in illumination. The simulation begins with the battery-discharge mode in steady state. Since the solar array's illumination level increases, its output current increases and the bus voltage rises. When the bus voltage reaches the battery-charger's reference voltage (28.14V), the battery-charger turns on and charges the excess current from the solar array to the battery. The fluctuation of charge-current, I_{CH}, comes from the numerical calculation process. The actual charge current should be smooth. The small integration-time step can
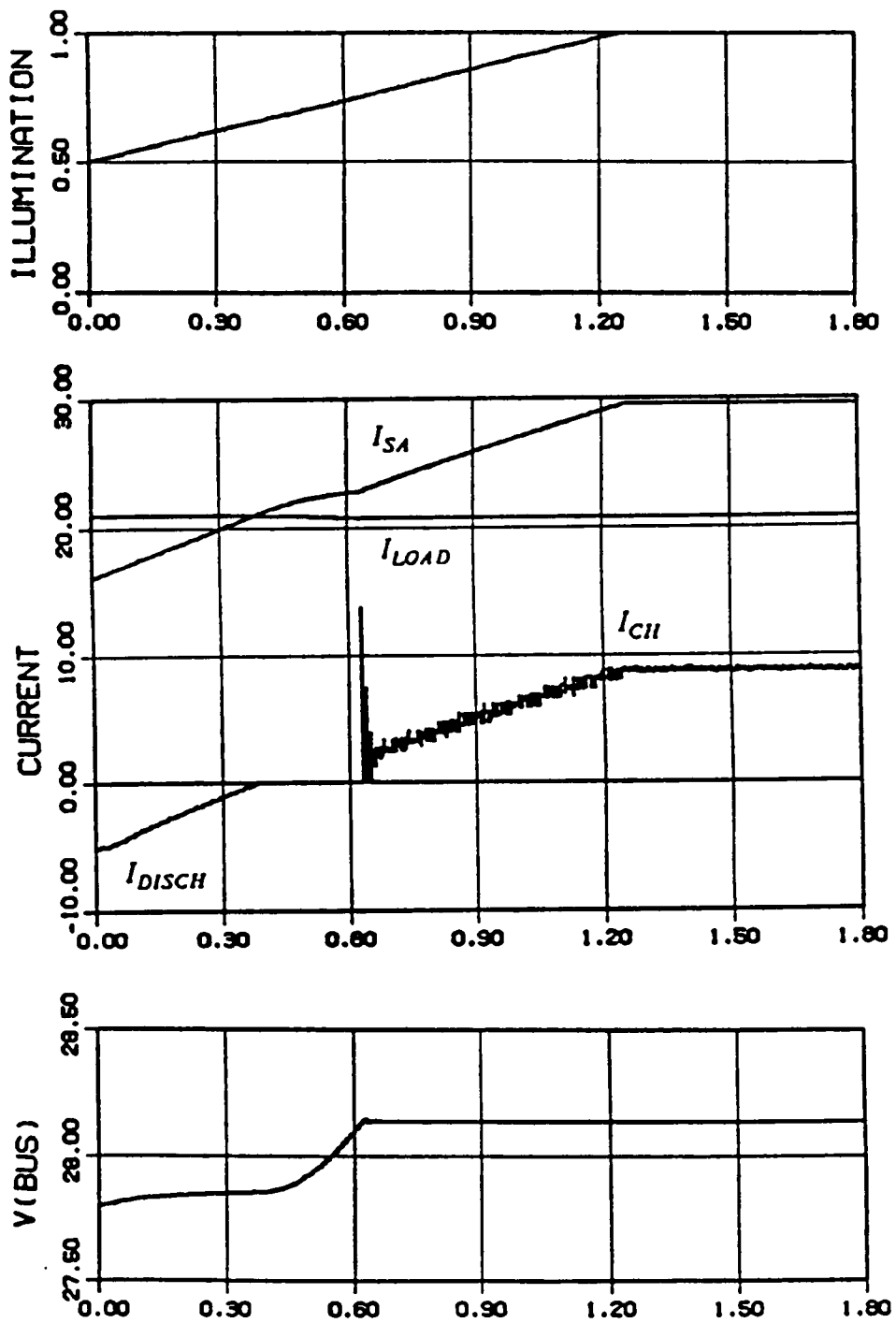
Fig. 5.25 Mode change simulation of COBE system
    (From B/D mode to B/C mode due to illumination change)

avoid fluctuation, but more computer time is needed. The system model description program and EASY5-generated schematic diagram are given in Figs. 5.26 and 5.27.

Other simulation results in Fig. 5.28 show a change from the shunt mode to the battery-discharge mode due to a step-load change. The simulation starts with the shunt mode in steady state. At 0.5 msec, the load power is increased from 584W to 1000W. As a result, the load current surpasses the output current of the solar array. The difference is supplied from the battery-discharger. The last plot shows the response of the switching current of the battery-discharger. As shown in these results, the local circuit behavior, as well as the system behavior, can be observed.

```
***************************************************
** COBE SYSTEM LARGE SIGNAL MODEL FOR TRANSIENT ****
** RESPONSE SIMULATION          REVISED ON 3/1/87 ****
***************************************************
MACRO FILE NAME = MACROS
LIST MACRO COMPONENTS = AR, SS, PT, BD, PZ, WM, FI, BH, CR
MODEL DESCRIPTION
LOCATION= 1, AR, INPUTS=MF(S, 2=IX)
LOCATION=22, SS, INPUTS=AR(VB=VB)
LOCATION=10, PT, INPUTS=AR(VB=VL)
LOCATION=19, PZ, INPUTS=AR(VB=VO)
LOCATION=39, WM, INPUTS=PZ(VE=VE)
LOCATION=65, BH, INPUTS=FI(I1=ILL), CR(IB=IBC)
LOCATION=33, CR, INPUTS=AR(VB=VB), BH(VC3=VBA)
LOCATION=71, MF, INPUTS=SS(IH=S, 1), PT(IL=S, 4), CR(IB=S, 3), BD(ILO=S, 5)
LOCATION=58, BD, INPUTS=AR(VB=V2), WM(IQ=IQ), FI(V2=V1)
LOCATION=66, FI, INPUTS=BH(VC3=V1), BD(IS=I2)
END OF MODEL
PRINT
```

Fig. 5.26 Model description of COBE system [SIM23.MOD]

Fig. 5.27 Schematic Diagram of [SIM23.MOD]

Fig. 5.28 Mode change simulation of COBE system
(From shunt mode to B/D mode due to step-load change)

Continued

SWITCH(Q1) CURRENT OF BATTERY DISCHARGER
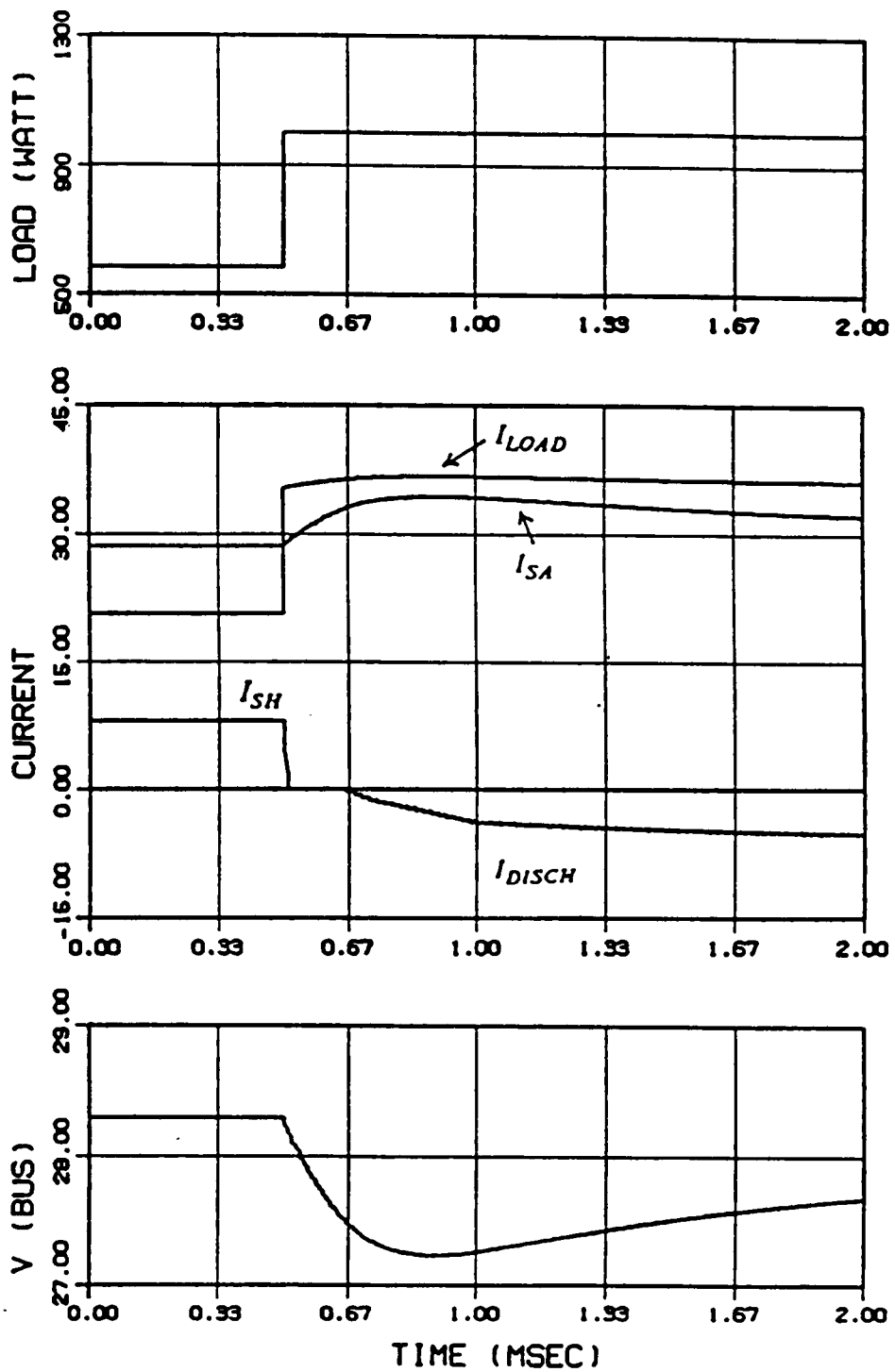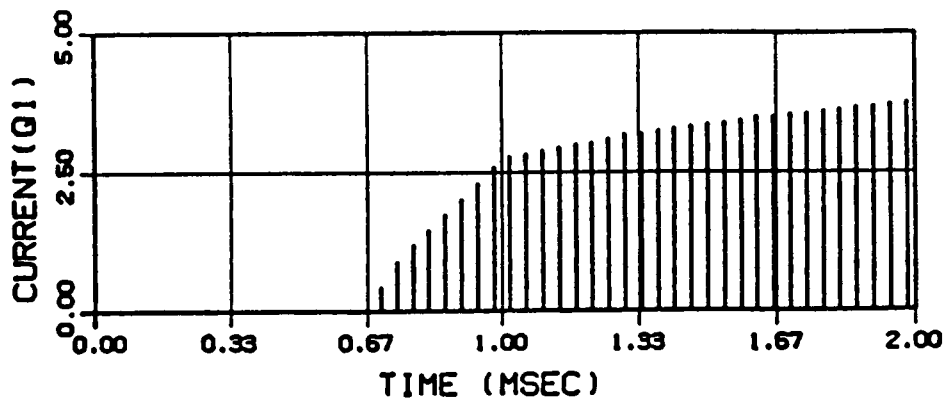
Fig. 5.28 Mode change simulation of COBE system
(From shunt mode to B/D mode due to step-load change)

5.5.3 One-Orbit-Cycle Simulation

For a simulation of a complete orbit cycle, the Mission Orbit Eclipse Phase, which has an orbit period of 103 minutes and a maximum eclipse period of 16 minutes, is chosen to show all modes of operation.

Since one cycle requires a long simulation, a longer time step is used to reduce computer execution time. However, the large time step causes numerical instability when the models include fast dynamics. To observe the system's behavior including the battery output voltage under the illumination change during one orbit cycle, fast dynamics of the power conditioning equipment are neglected, because the time constant of the battery is much larger than the others. Therefore, the battery charger and battery-discharger models are replaced with dc models not having L and C. The system's block diagram for this simulation is shown in Fig. 5.29. Since the time constant of the battery model is very long (i.e., the capacitance value of the battery is on the order of 10,000 Farads), if the time constant of the increased L and C are still much shorter than that of the battery, the simulation results are valid for observing the current and voltage profile during an orbit cycle.

The dc models of battery charger and battery-discharger as described as follows.

DC Model of the Battery Charger [CH]

This dc model is necessary when the one-orbit cycle is simulated. Since simulation of one orbit requires a large integration time step, the model should not include any fast dynamic components such as a small inductor or capacitor.

When the bus voltage is greater than the reference voltage, V_{ref}, of the battery charger, and the MOSFET is not saturated, the charging current

V(BUS)

I_{SA}

I_{CH}

I_{DISCH}

I_{SH}

I_{LOAD}

[AR]

[CH]

[DC]

[SS]

[PT]

SOLAR
ARRAY

BATTERY
CHARGER

BATTERY
DISCHARGER

SEQUENTIAL
SHUNT
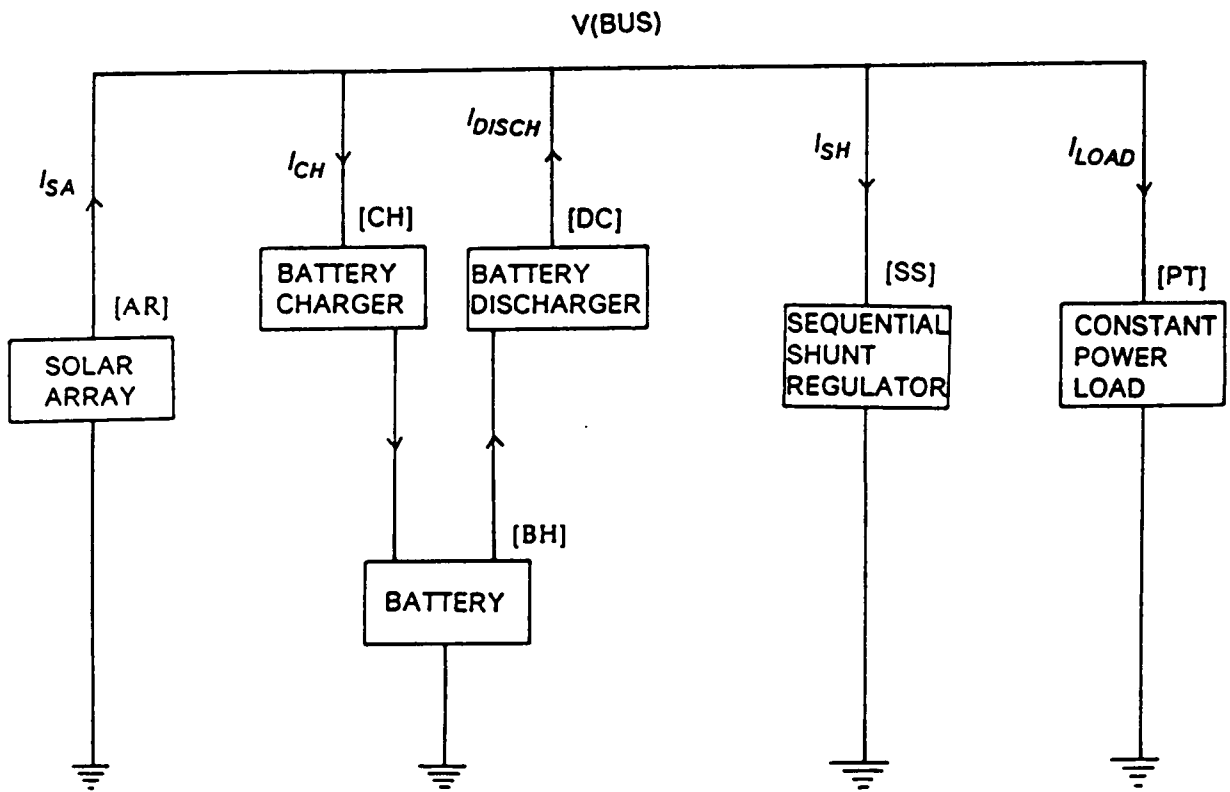REGULATOR

CONSTANT
POWER
LOAD

[BH]

BATTERY

Fig. 5.29 COBE power system block diagram
(for one orbit cycle simulation)

196

is proportional to the voltage difference between the V_{bus} and V_{ref}. As a result, the bus voltage is regulated at V_{ref} while the charging current flows in the linear region of the MOSFET. This voltage regulation mechanism can be expressed as

$$I_{ch} = gm_1 (V_{bus} - V_{ref}) \qquad (5.32)$$

where gm_1 is the transconductance of the battery charger. When the battery voltage reaches a certain value, the MOSFET becomes saturated and the charging current is proportional to the MOSFET's drain-source voltage, V_{ds}. Assuming that saturation occurs when the battery voltage reaches $V_{bat}(\max) - 0.1V$, the charging current during MOSFET saturation can be expressed as

$$I_{ch} = gm_2 V_{ds} = gm_2 [V_{bat}(\max) - V_{bat}] \qquad (5.33)$$

when

$$V_{bat}(\max) - 0.1V \leq V_{bat} \leq V_{bat}(\max) \qquad (5.34)$$

where gm_2 is the inverse of the on-resistance during MOSFET saturation.

DC Model of the Battery-Discharger [DC]

The battery discharger functions as a stiff voltage source when the bus voltage is below the reference voltage of the battery discharger, V_{ref}. This can be modeled as

$$I_{disch} = gain(V_{ref} - V_{bus}) \qquad (5.35)$$

where the gain is the inverse of the internal resistance of the stiff voltage source and V_{ref} is 28.0V in this model.

The first simulation is at constant load and only the illumination level varies. The simulation results shown in Fig. 5.30, were obtained using a one-second time step. Simulation starts when the spacecraft comes into eclipse. During the 18-minute eclipse, the power system is operated in the battery-discharge mode and, after that, it is in the battery-charge and shunt mode. Battery charging starts earlier than the shunt mode. After the battery is fully charged, most excess current from the solar array is shunted through the shunt regulator. Since the MOSFET of battery charger becomes saturated when the battery voltage reaches a certain value, the response of battery voltage is almost constant after eclipse period.

Since the simulation results of the battery voltage and current waveforms are similar to those waveforms shown in [28], which come from the experimental data, these models can be verified.

The second simulation uses the case of the load power changing from 584W to 900W at 50 minutes and returning to 584W at 63 minutes. As shown in Fig. 5.31, at 50 minutes the load current demand becomes higher than the supply current of the solar array. Then, the battery-discharger current starts to flow. When the load power step-changes down to the original value, the battery-charger current flows again.
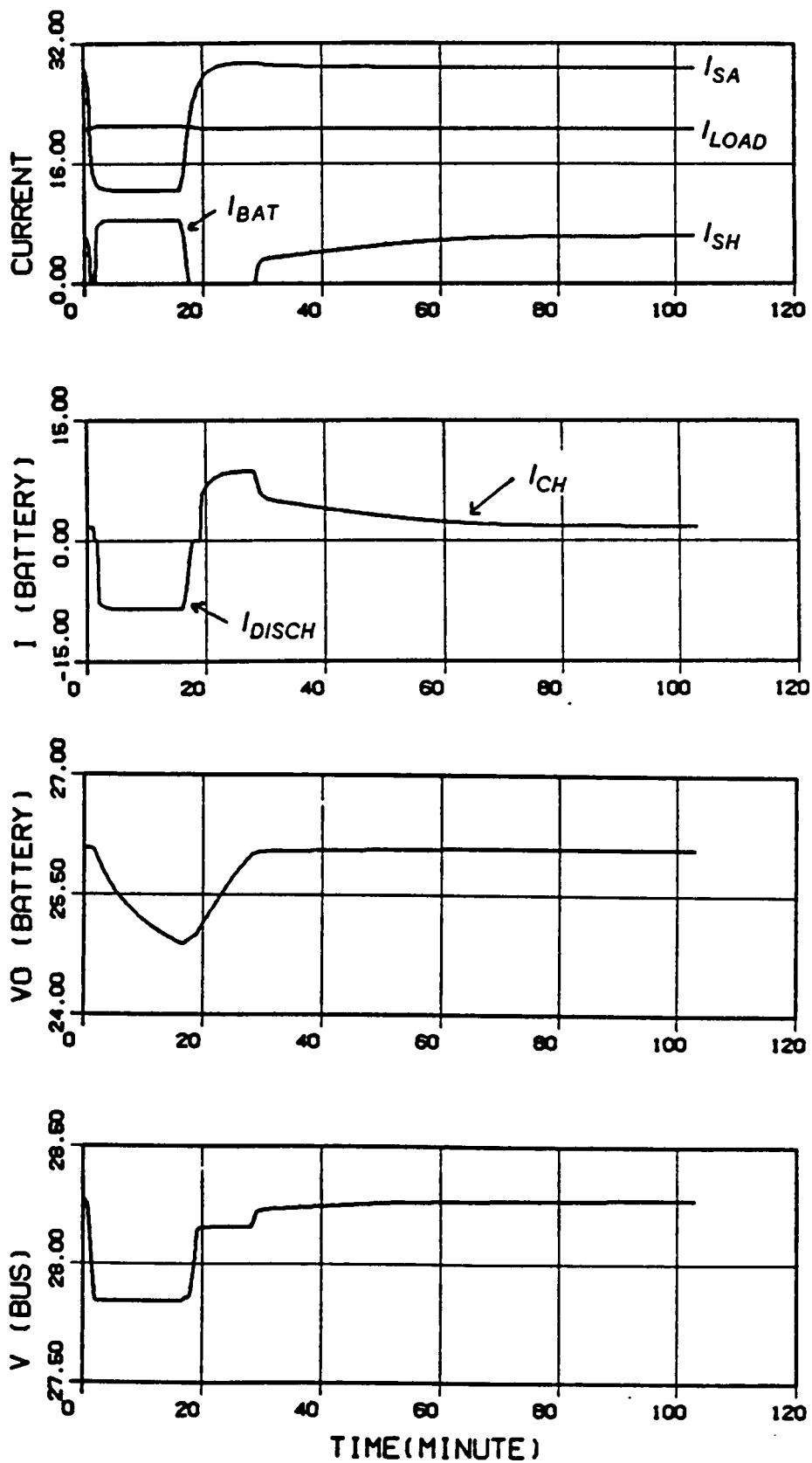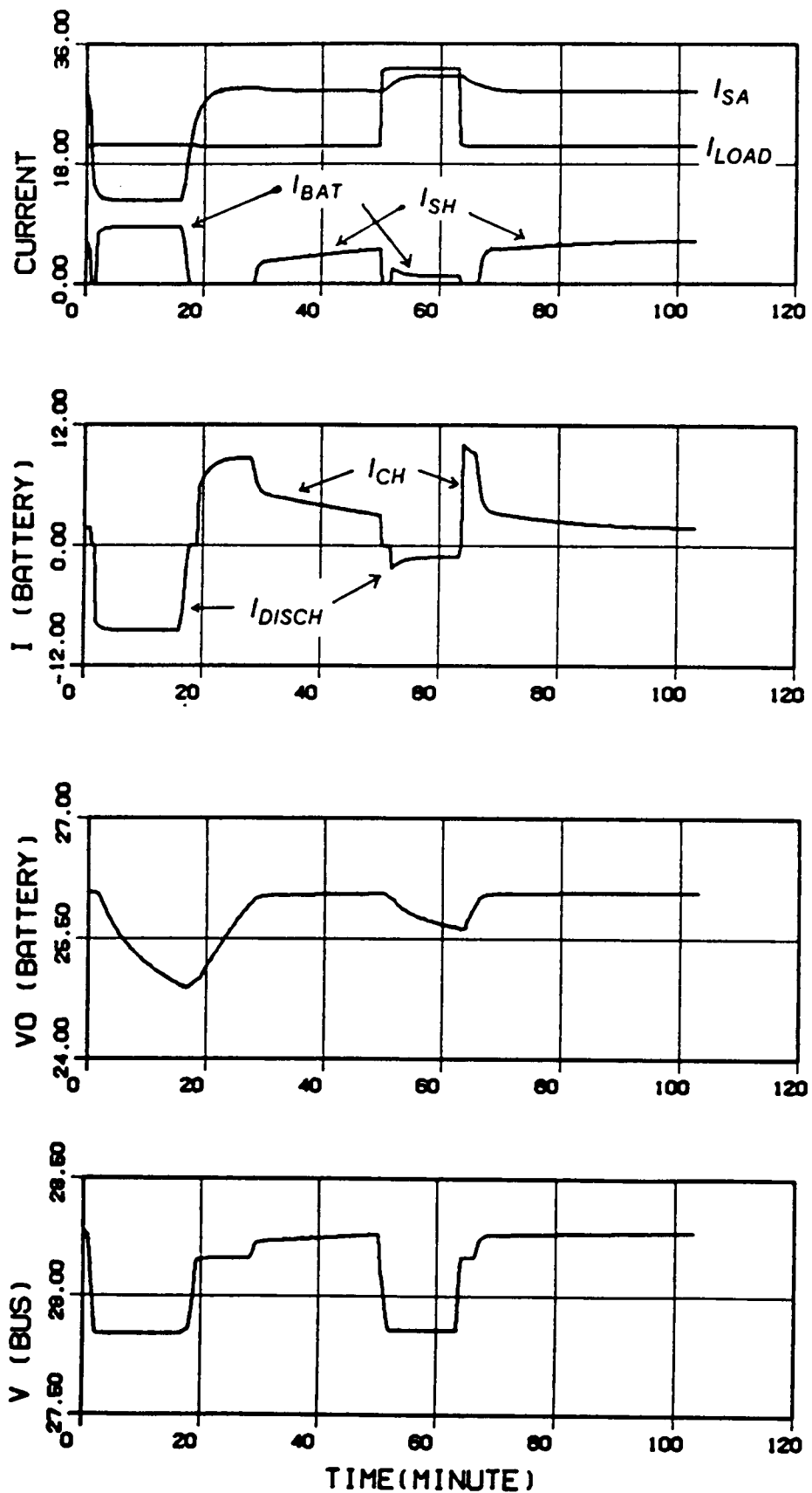
Fig. 5.30 One-orbit cycle simulation of COBE system

Fig. 5.31 One-orbit cycle simulation of COBE system
with step-load change

5.6 Conclusions

Various spacecraft power systems, such as the solar array switching system, partially-shunted solar array system, peak power tracking solar array system and COBE power system, were analyzed and simulated to study each system's performance.

Two solar array switching power systems, SASU with a shunt regulator system and a sequential switching shunt regulator system, were simulated and their performances were observed to compare their characteristics. The SASU with a shunt system gives fine regulation of bus voltage, but has thermal dissipation in the shunt circuit. The PWM-type SSSR system has minimum thermal dissipation, but the bus voltage ripple exists due to PWM control.

The dynamic behavior of the SASU system with a shunt regulator is almost the same as the solar array system with a shunt regulator, because the shunt regulator of the SASU is always active.

A simplified SSSR system was modeled to understand the feedback control of SASU systems. In Region #2, the SASU system without a feedback loop is unstable; the feedback circuit provides the stability of the system. The gain of the bus voltage feedback should be greater than $|\frac{1}{r_S} - \frac{1}{r_L}|$ to make the system stable. Since the feedback circuit of the SASU system functions as a shunt regulator, design criteria of the control circuit of the SASU system is the same as that of the shunt regulator.

The partially-shunted solar array system reduces the peak power dissipation to a range of 30-50% of the amount dissipated in a functionally-equivalent full shunt. The partial shunt system was simulated and the

voltage and current waveforms of the upper and lower array sections were observed during load change from full load to no load.

For the low earth orbit spacecraft, the peak power tracking system is effective to avoid the high dissipation in shunt regulators. The idea of the PPT is to make the PPT's input resistance match with the incremental resistance of the solar array at its peak power point.

To show the capabilities of the modeling technique using EASY5, the power system of an existing spacecraft, COBE, was modeled and simulated to show transient response during mode change from a battery-discharging mode to a battery-charging mode. A one-orbit cycle simulation was performed using the solar array model, dc models of the charger and the discharger, battery model and constant power load model. From this simulation, the voltage and current profiles of the solar array and battery were observed for a complete orbit cycle.

CHAPTER 6

CONCLUSIONS

The major objective of this dissertation has been to develop computer models and perform comprehensive analyses of the dynamics of various spacecraft power systems. The analyses characterize large-signal and small-signal dynamics of the systems and provide design information for system-level operating points, as well as local power conditioning equipment, to provide stability and optimum performance. The analyses are made in various modes of operation, including the shunt, battery-charge and -discharge mode. A comprehensive modeling technique using the EASY5 program is employed to facilitate an essential design iteration loop (namely, analysis, design and performance verification) for the various Direct Energy Transfer (DET) systems.

Component models, such as the battery charger, storage battery, solar array switching unit and partially-shunted solar array, are developed to facilitate the simulation of the various DET systems. The development of an equivalent circuit for the battery model provides the capability for transient analysis of the whole power system. Generic computer models

developed for spacecraft power systems' components and subsystems have been utilized to simulate performance verification for existing hardware in industry.

The large-signal stability analysis of the main bus of the DET system is performed by utilizing the simplified second-order system, which includes nonlinear characteristics of the source, load and power conditioning equipment (bus regulators). The regulators can be viewed either as a load to the solar array source or as a part of the source to the constant-power load. These regulators effectively change the system eigenvalue to stabilize the system even in the high source impedance region (current source region) of the solar array. The stability criteria in each mode are developed in terms of the incremental resistances of the solar array and each piece of power conditioning equipment, and in terms of the bus filter capacitance and cable inductance. The state trajectory is used to analyze the large-signal dynamic behavior of the system in various modes, such as the shunt, battery-charge and -discharge modes and the deadband mode.

The phenomenon of solar array/battery lockup, a condition in which the battery discharges even when the solar array alone can supply the load, is graphically analyzed and simulated for verification. The I-V characteristics of the source in the DET system is composed, basically, of three parts: output I-V characteristics of the solar array with a battery discharger at the bus voltage below the discharger's reference voltage, output I-V characteristics of the solar array with a shunt regulator at the bus voltage above the shunt regulator's reference voltage and the I-V

characteristics of the solar array itself at the bus voltage between the two reference voltages. The system can escape from the lockup by either temporarily reducing the load power or temporarily increasing the solar array power. That is, the system should be forced to have only one equilibrium point on the shunt line to escape from the lockup.

Two failure modes, shunt regulator failure and battery discharger failure, are analyzed in the state-plane. In examining these failures, it is assumed that each piece of equipment is abruptly disconnected from the bus. The main bus behavior, such as the bus voltage, solar array current and load current after the failure, are observed from simulations.

In order to characterize the small-signal dynamics of the system bus, such as the bus impedance and stability, the system loop gain is identified. The loop gain, T, is the product of the transadmittance of each bus regulator, Y, and the source impedance of the solar array with a bus filter capacitor. Therefore, for a given source impedance characteristic, the loop gain, T, can be shaped for the optimum bus dynamics and stability by properly designing Y.

In a buck-type battery charger, proper input filter design and the bus voltage feedforward loop ensure the system's stability in the charger's bus voltage regulating mode. During the charging current regulating period of the charger, since the charger no longer functions as a bus regulator, it should be treated as a constant-power (constant-current) load.

For the design and analysis of the battery discharger, a two-loop controlled boost regulator with a secondary filter is considered. A simplified

design approach using the unterminated regulator is introduced. In addition to the frequency-domain analysis and simulation, time-domain simulations are performed using large-signal models to verify design and analysis in the three modes.

Two SASU systems, a SASU with a shunt regulator and a PWM-type sequential switching shunt regulator (SSSR), are compared and their advantages and disadvantages are identified through analyses and simulations. The SASU system with a shunt system provides good stability and fine regulation of the bus voltage, because the shunt regulator is always active whenever the SASU control is activated. The small-signal dynamics are the same as those in the linear shunt. In the PWM-type SSSR system, a PWM-controlled shunt switch controls the effective output current from one section of the solar array. The analysis shows that the SSSR feedback loop functions as a shunt regulator. The analysis is simulated and verified by modeling the PWM action as a control for the effective number of parallel array strings connected to the bus.

The partial shunt system is analyzed and simulated to show its advantage of having less power dissipation than the full shunt regulator. Since only the lower portion of the solar array is shunted, much less power is dissipated in the partial shunt regulator. The output impedance and system loop gain are derived in terms of the shunt admittance, impedance of the upper and lower solar array section and impedance of the bus capacitor.

The concept of the peak power tracker system is illustrated using buck-type and boost-type PPT examples. The basic idea of the PPT is to intentionally locate the operating point at the solar array's peak power point by controlling its duty ratio.

Finally, one existing spacecraft power system, COBE, is modeled and simulated to observe transient response and one-orbit cycle response and to demonstrate the effectiveness of the computer modeling and simulation. Some of the simulation results are compared with the hardware test data and show good agreement.

REFERENCES

1. Boeing Computer Services, "EASY5 Dynamics Analysis System User's Guide," 1983.

2. B. H. Cho, "Spacecraft Power System Analysis," Ph.D. Dissertation, 1985, VPI & SU, Blacksburg, Virginia.

3. B. H. Cho, F. C. Lee, "Modeling and Analysis of Spacecraft Power Systems," IEEE Transactions on Power Electronics, Jan., 1988.

4. R. D. Middlebrook, S. G. Kimble, "Design of the HEAO Main Bus Shunt Regulator," IEEE Transactions on Aerospace and Electronic Systems, March 1976.

5. J. M. Voss, J. G. Gray, "A Regulated Solar Array Model - A Tool For Power System Analysis," IEEE PCSC 1970 pp.12-17.

6. A. Capel, et al., "Power System Simulation of Low Orbit Spacecraft: The EBLOS Computer Program," IEEE PESC 1982, pp.272-285.

7. Robert L. Bailey, "Solar-Electrics Research and Development," Ann Arbor Science, 1980, pp.112.

8. J. R. Lee, S. J. Kim, B. H. Cho, F. C. Lee, "Computer-Aided Modeling and Analysis of Power Processing Systems-Phase II," Final Report to NASA-GSFC, VPI & SU, Blacksburg, VA, July, 1987.

9. J. R. Lee, B. H. Cho, S. J. Kim, F. C. Lee "Modeling and Simulation of Spacecraft Power Systems," IEEE Transactions on Aerospace and Electronic Systems, May, 1988.

10. H. G. Zimmerman, R. G. Peterson, "An electrochemical Cell Equivalent Circuit for Storage Battery / Power System Calculations by Digital Computer," IECEC 1970.

11. E. N. Costogue, S. Lindena, "Comparison of Candidate Solar Array Maximum Power Utilization Approaches," IECEC 1976, pp.1449-1456.

12. R. D. Middlebrook, "Input Filter Considerations in Design and Application of Switching Regulators," IEEE IAS, 1976 Record, pp. 366-382.

13. B. H. Cho, J. R. Lee and F. C. Lee, "Large-signal Stability Analysis of Spacecraft Power Processing Systems," IEEE PESC, 1987.

14. D. W. Jordan, P. Smith, "Nonlinear Ordinary Differential Equations," Oxford University Press, 1985.

15. A. Capel and D. O'Sullivan, "Influence of the bus regulation on Communication Spacecraft Power System and Distribution," ESA SP-230, Jun., 1985.

16. D. W. Zerbel, D. K. Decker, "AC Impedance of Silicon Solar Cells," IECEC, 1970.

17. R. B. Ridley, B. H. Cho, F. C. Lee, "Analysis and Interpretation of Loop Gains of Multi-Loop-Controlled Switching Regulators," The Power Electronics Show & Conference, San Jose, California, Oct., 1986.

18. R. A. Carter, F. C. Lee, "Investigation of Stability and Dynamic Performance of Switching Regulators Employing Current-Injected Control," IEEE PESC 1981.

19. R. B. Ridley, "Secondary Filter Analysis and Design Techniques for Current-Mode-Controlled Converters," Power Electronics Conference, Boston, Mass., 1987.

20. M. A. Green, "Solar Cells," Prentice-Hall, Inc., 1982.

21. D. K. Decker, J. Cassinelli, "High Power Solar Array Switching Regulation," Sixteenth IECEC Record, Atlanta, 1981.

22. S. G. Kimble, J. F. Wise, "Integrated Electronics Solar Array Control Units," IEEE PCSC 1971, pp.77-85.

23. D. O'Sullivan, A. Weinberg, "The Sequential Switching Shunt Regulator S^3," ESA SP-126.

24. G. W. Fleck, "Solar Array Switching Unit Stability Analysis," IECEC 1984, pp.576-581.

25. Paul S. Nekrasov, "Partial Shunt Regulation," AAS 68-067, 14th Annual Meeting AAS, May 1968, Dedham, Mass.

26. C. A. Bernard, JR., "A Second Generation (High-Speed) Maximum Power Tracker For Space Applications," Proceedings of the Fifth Space Congress, Cocoa Beach, Florida, Mar., 1968.

27. P.R.K. Chetty, "Electrical Power System for Low Earth Orbit Spacecraft Applications," IECEC 1987, pp.281-287.

28. V. C. Muller, D. A. Webb, "Nickel-Cadmium Batteries for the Modular Power Subsystem," IECEC 1980, pp.1638-1642.

29. W. Burns, III, et al., "A Digital Simulation and Study of Direct Energy Transfer Power Conditioning System," IEEE PESC, 1975 pp.138-149.

30. R. D. Middlebrook, S. Cuk, "A Generalized Unified Approach to Modeling Switching Converter Power Stages," IEEE PESC 1976.

31. P. Chen, et al., "Experimental Determination of Series Resistance of p-n Junction Diodes in Solar Cells," IEEE Tran. on Elec. Devices, vol.ED-25, march 1978, pp.386-388.

32. R. Otterbein, D. Evans, "Two Modified Single Diode Models for Simulating Solar Cells with Distributed Series Resistance," IEEE PSC, Aug. 1970.

33. M. Imamura, J. Portacheller, "An Evaluation of the Methods of Determining Solar Cell Series Resistance," IEEE PSC, Aug. 1970.

34. H. T. Weaver, R. D. Nasby, "Analysis of High Efficiency Silicon Solar Cells," IEEE Tran. on Electron Devices, vol.ED-28, May 1981, pp.465-472.

35. E. R. Hoover, "Solcel II: An Improved Photovoltaic System Analysis Computer Program," IECEC, 1980.

36. P. Chetty, et al., "Microprocessor Controlled Digital Shunt Regulator," IEEE Tran. on AES, March 1980, pp.191-200.

37. M. Imamura, et al., "Computer Simulation Concept for a Large Solar Array/Battery Power System," IECEC, 1972.

38. H. Weiner, "Power Subsystem Performance Prediction Computer Program," IECEC, 1972.

39. M. Schwartzburg, "Analysis of Solar Array/Battery Lock-up by Computer Simulation of Electric Power System Performance," TRW Systems Group, IECEC 1971.

40. L. R. Ostwald, "Maximizing the Useable Energy from a Spacecraft Power System," IECEC 1971, pp.985-994.

41. S. R. Peck, R. N. Devaux, "STC/DBS Power Subsystem Control Loop Stability Analysis," IECEC, 1984.

42. J. Cassineli, et al., "Analytical Modeling of Spacecraft Power System," Final Report to NASA GSFC, 1982, TRW, Redondo Beach, CA